University of Alberta

Role of Ultra-Fine Solid Fractions on Rheology of Oil Sands Suspensions

by

Sepideh Samiei

©

A thesis submitted to the Faculty of Graduate Studies and Research
in partial fulfillment of the requirements for the degree of

Master of Science

in

Chemical Engineering

Department of Chemical and Materials Engineering

Edmonton, Alberta
Fall, 2007

Canada

Abstract

Success of the conventional separation process used for oil sands extraction as well as effective disposal of oil sands processing reject tailings are highly influenced by the nature of ultra-fine clay particles in oil sands. In this study, the effect of three ultra-fine solid fractions on the rheology of solids suspensions derived from oil sands processing was investigated.

Three solids fractions having different particle size distributions were separated from mature fine tails (MFT) and their rheological properties were studied. Rheological measurements along with other complementary characterization methods were utilized to characterize the solids and understand their behaviours. It was found that the fraction of solids containing the highest amount of organic matters corresponded to the highest viscosities, yield stress and gel strength in the suspensions. While electrostatic interactions played a role in the observed behaviour, the presence of organic matter was the largest contributor to high elastic characteristic in this particular fraction.

Acknowledgements

I wish to thank Drs. Jacob Masliyah and Zhenghe Xu for their bright guidance throughout the course of this work. They taught me to welcome challenges and to question preconceptions.

Thanks to Dr. Sola Adeyinka and Mr. Brad Komishke for their creative ideas which highly contributed to the progress of this work. My gratitude also goes to Dr. Tony Yeung for his valuable criticism and advice.

I acknowledge Mr. Jim Skwarok and Ms. Leanne Swekla for being accommodating and resourceful on every occasion. I am also grateful to Dr. Sili Ren for his collaboration in obtaining the AFM results. I thank Dr. Trong Dangvu for sharing his experience in contact angle measurements.

I also would like to thank Mr. Shiraz Merali for collecting XRD patterns and Dr. Dipo Omotoso for his help with XRD data analysis. Thanks to Ms. Tina Barker and Mr. Shihong Xu for their assistance with SEM imaging. I would like to extend my gratitude to all administrative and support staff at the Chemical and Materials Engineering Department for being friendly and reliable.

Finally, my deepest gratitude goes to my family and friends. I am forever grateful to my family for their love and support; for being part of my life; for being my wings and letting me fly; and for teaching me how to see good things in life. I thank all my friends for standing by me and for showing me how friendship knows no boundaries.

Table of Contents

List of Tables

List of Figures

List of Nomenclature

(i)   Latin Symbols

a Particle diameter (μm)

D_p Particle Diameter (μm)

d_{50} Mean particle diameter (μm)

F Long-range interaction force (mN)

F_a Adhesion force (mN)

G Elastic modulus (Pa)

$G*$ Complex viscoelastic modulus (Pa)

G' Storage modulus (Pa)

G'' Loss modulus (Pa)

M Torque (N·m)

R Cone diameter (mm)

R_p Probe diameter (m)

t Time (s)

V_t Settling velocity (m/s)

(ii)   Greek Symbols

β Cone angle (Degrees)

δ Phase lag (Degrees)

γ Deformation

γ_0 Oscillatory deformation amplitude

$\dot{\gamma}$ Deformation rate (s^{-1})

κ Inverse Debye length (μm)

μ Viscosity (Pa·s)

μ_c Casson viscosity (Pa.s)

μ_r Relative viscosity

Ω Angular velocity (rpm)

θ Contact angle (Degrees)

ρ Fluid density (kg/m^3)

ρ_s Particle Density (Kg/m^3)

τ Stress (Pa)

τ_y Yield stress (Pa)

τ_0 Oscillatory stress amplitude (Pa)

τ' In-phase stress response (Pa)

τ'' Out-of-phase stress response (Pa)

ω Angular frequency (rad/s)

ζ Zeta potential (mV)

List of Acronyms

AA	Atomic Absorption
AFM	Atomic Force Microscope
CSS	Cyclic Steam Simulation
FTIR	Fourier Transform Infrared Spectroscopy
MFT	Mature Fine Tails
NMR	Nuclear Magnetic Resonance
PALS	Phase Analysis Light Scattering
PSD	Particle Size Distribution
SAGD	Steam Assisted Gravity Drainage
SEM	Scanning Electron Microscope
TG	Thermogravimetry
XRD	X-Ray Diffraction

1. Introduction

1.1. Oil Sands

In 2005, Canada produced $136.4*10^6$ cubic meters of crude petroleum. Two thirds of this production came from Alberta where oil sands production corresponds to 42% of the province's total production [1]. At the end of year 2004, the remaining oil sands reserves in Alberta were estimated to be 28 billion cubic meters, making it the second largest oil reserve in the world after Saudi Arabia [2]. Oil sands can be produced through either surface mining or in-situ processes. When the reserves are too deep to be economical for surface mining techniques, alternative in-situ operations such as steam assisted gravity drainage (SAGD) or cyclic steam simulation (CSS) are applied [3].

The oil component in oil sands is bitumen. Bitumen is a high molar mass viscous hydrocarbon. Oil sands ore contains 6–14 wt% bitumen and 80–85 wt% mineral solids balanced by water [4]. Processability of oil sands in the past years was determined based on bitumen content of ores. High bitumen content in the ore corresponded to good processing performance, whereas low bitumen content often posed difficulties in the separation process. However, it was found that ore processability is not only related to its bitumen content. The nature of the mineral solids associated with oil sands is found to determine ore processability [4-5].

The solid components of oil sands are mainly quartz sand and clay particles. Mineral type and content in the oil sands ore are used as markers to determine ore processability. The fortunate property of Alberta oil sands is the affinity of its solids towards water. However, at high concentrations of solids smaller than 12 μm (ultra-fines), difficulties in the separation process are anticipated [4-5]. In this case, precautionary measurements would be required to avoid reduced recovery. On the other hand, ores that have low ultra-fines content are considered good processing ore where little difficulties in separation are expected.

1

Between the content of bitumen and solids in an oil sands ore, a direct correlation was known to exist. For ores of low bitumen content, ultra-fine solids content was expected to be high. This correlation, however, is not valid for certain ore types such as weathered ores. Lately, the ultra-fines content of ores had been used as a marker to identify the processability of certain oil sands.

1.2. Separation Process

Separation of bitumen from sand is conventionally carried out through a water based extraction process. The mined ore is slurried with warm water. The slurry is then conveyed to the extraction plant via hydrotransport pipelines. In mining operations, 2 to 4.5 cubic meters of river water is used to produce one cubic meter of oil from oil sands [6]. The main sources of water for the extraction process are fresh water from Athabasca River and recycle water from the plant.

Flowing through the pipeline provides mechanical energy that is required for bitumen liberation from the sand grains. The liberation process is affected by water temperature as well as the surface and interfacial properties of sand, bitumen and water. In some cases, additives, such as sodium hydroxide, are used to control the slurry pH. The control of pH helps optimize the surface properties of different species in the slurry [7].

Bitumen liberated from sand grains forms droplets that are of the same density as water. In order to achieve efficient separation of bitumen from the sand grains, it is imperative to have an appreciable difference between the densities of bitumen and water. Bitumen droplets therefore are to attach to air bubbles which are present during the slurry flow in the hydrotransport pipeline. Aeration of bitumen droplets lowers their overall densities and facilitates the separation of bitumen from the sand grains by gravity separation. A favourable scheme of aeration is when bitumen droplets engulf air bubbles. In order to have a higher rate of engulfment, as opposed to other forms of bitumen aeration, water temperature and pH need to be optimized.

2

Separation of aerated bitumen from sand grains is achieved in a gravity separation vessel. The oil sands slurry containing aerated bitumen and solids enters the plant as the feed stream to the separation vessel. Figure 1.1 schematically shows different zones and streams in a gravity separation vessel. In the vessel, the flow mode is quiescent. This condition is designed to assist flow of aerated bitumen and coarse sands in opposite directions. The aerated bitumen of overall density less than the density of its suspending medium floats to the top and forms a bitumen froth layer. After de-aeration, this separated froth on average contains 60 wt% bitumen, 30 wt% water and 10 wt% solids [7]. To clean up the water and solids in the froth, further processing is performed in froth treatment units.

In the gravity separation vessel, the coarse solids have a higher density as compared to their suspending medium. Under normal extraction conditions, these solids separate fairly effectively to the bottom and form the tailings stream. From the middle of the gravity separation vessel, an intermediate stream is withdrawn. This stream is often referred to as the middlings stream. The tailings and middlings streams are directed to flotation cells where more bitumen is separated from the slurry. Since bitumen cannot be utilized as a commercial petroleum product, additional upgrading units are needed to convert the separated bitumen to synthetic crude oil.

1.3. Problem Definition

Although the basic principles of bitumen extraction from oil sands appear rather simple, the entire process suffers from the production of a large amount of tailings. In addition, the recovery process experiences significant drawbacks due to the presence of fine solids for certain types of ores. The following sections provide more details on these two shortcomings and clarify the need to search for a better understanding of oil sands slurries.

3

1.3.1. Mature Fine Tails (MFT)

After residual bitumen is separated from the tailings and middlings, the streams containing reject solids are combined and directed to tailings ponds. In the ponds, the coarse fraction of solids rapidly segregates from the fine fraction and settles. The fine solids, on the other hand, are of much slower settling rates. After two to three years of settling, these fine solids reach a particle concentration of about 30 to 40 wt% and form a stable suspension called mature fine tails (MFT). Once an MFT is formed, its strong networked structure of solids leads to no further consolidation. The main components of MFT are kaolinite, illite and some mixed forms of smectite clays. It has been estimated that complete settling of MFT solids would take more than a century to occur [8].

The networked structure of solids in MFT traps significant amounts of water with noticeable organic matters, leading to environmental hazards and economical problems associated with the storage of solid rejects in the tailings ponds. Therefore, disposal of unconsolidated tailings is one of the major challenges in the oil sands industry.

1.3.2. Gelation

Structure formation of oil sands solids in aqueous suspensions can also lead to reduced recovery in the extraction plant. Occasionally, a high build up of solids causes gel (sludge) formation in the gravity separation vessel. This gel has strong elastic (solid-like) characteristics. With high viscosity and yield stress, formation of gel poses a high resistance against the rise of aerated bitumen through the separation vessel. As such, gel formation interrupts the separation of the aerated bitumen from sand. Under such circumstances, bitumen content of the froth is reduced and recovery becomes low. With little bitumen reporting to the froth, the middlings stream will have high content of hydrocarbon as well as solids. Flow properties of the middlings in this situation are similar to that of a solid-like gel. Accordingly, this operational condition is referred to as "gelation" or "sludging" of the separation vessel.

Common industrial countermeasures against sludging are to use dispersing agents, decrease throughput and/or dilute the feed slurry with water. These approaches, however,

4

are not successful for some problematic ores; other remedial actions are required in such cases. Research on the cause of gelation and methods to avoid it is on-going. Primarily, the ultra-fine fraction of oil sands solids are known to be the cause of the problem. These particles are mostly clay minerals.

1.4. Clays

Ultra-fine clay particles strongly enhance the stability of oil sands solid dispersions. Two of the most noticable problems associated with oil sands extraction (discussed in Section 1.3) appear to be directly related to the presence of ultra-fine solids. This section, therefore, will provide some information on clay mineralogy and clay-in-water dispersions.

When placed in an aqueous solution, particles in the ultra-fine size range form a colloidal system, the state of which strongly depends on the interactions between the particles. A basic knowledge of clay mineralogy, surface properties and their charging mechanisms is therefore required to understand whether or not clay dispersions will form a dispersed stable sol or will flocculate. Reference [9] gives the details of what is summarized here.

1.4.1. Unit Layer Structure

Clay particles are composed of two dimensional arrays of silicon-oxygen tetrahedra and two dimensional arrays of aluminum- or magnesium-oxygen octahedra. Different clays are composed of different arrangements of these sheets in their unit layers. A single clay particle can have multiple unit layers stacked on top or next to one another. The layers are held together by van der Waals forces, which are a universal force that exists between all materials and causes attraction between their molecules.

Based on the structure of their unit layers, clay minerals can be divided into different families. Three-layered clays such as illite or smectite have unit layers composed of one octahedral sheet located between two tetrahedral sheets of silicon oxygen. The metal oxide sheets of the unit layers in these minerals are held together by attractive van der

5

Waals forces. Two-layered clay particles, such as kaolinite clays have one tetrahedral silicon-oxide sheet attached to a sheet of aluminum oxide or hydroxide octahedral. The position of the metal oxides in the tetrahedral and octahedral sheets gives a hexagonal symmetry to the plate-like structure of clay particles.

In certain types of three-layered clays known as smectites or montmorillonite clays, once the clay is brought in contact with water, penetration of water between the unit layers increases the distance between them and causes the clay to swell. The swelling characteristic of smectite clays is what distinguishes them from other three-layered clays. Swelling of montmorillonites increases solids volume fraction in aqueous solutions and enhances the gelation propensity of their suspensions. These clays are known to form a gel at lower particle concentrations as compared to other types of clays. In illite clays, a non-swelling capacity is observed. This is attributed to the potassium ions linking the unit layers together. The interlayer water of smectite clays can be removed by intense heating which causes the layers to collapse. Repeated heating of smectites stabilizes the potassium in between the layers and renders the particles non-expandable.

1.4.2. Charging Mechanisms

Gel formation in clay suspensions is strongly controlled by the electrostatic interactions between the particles. Unit layers of clay particles can obtain electric charges by substitution of ions in the tetrahedral and octahedral sheets. Sometimes, the tetravalent silicon ions can be replaced by trivalent aluminum leaving the surface with a negative charge. This situation is due to similar morphology of the ions exchanging between the layers. The charging mechanism of this form is thus known as isomorphous substitution of ions.

Aluminum can also be replaced by divalent atoms such as Fe, Cr or Zn. This substitution will also leave the clay surface with a negative charge which can be balanced by positive ions that are too large to penetrate inside the unit layer. Once the clay particles are placed in water, the positive surface ions are exchanged by other cations present in the water. The exchange capacity of such cations is a means for identifying different types of clays.

6

Clay minerals can also have charges along their edges. There is a significant structural difference between the edges of the clays and the flat basal faces. Primary alumina and silicon oxygen bonds are broken at the edges, which leaves a pH dependent charge at the edges. Kaolinite clays, for example, carry a positive edge charge under acidic conditions. The edge charge for this type of clay is reversed by increasing solution pH to alkaline values.

1.4.3. Particle Association in a Clay Suspension

With opposite charges present on the edges and faces of the clay particles, under favourable conditions, these solids can form different types of particle agglomerates. Depending on the surfaces (edge or face) that come together, the structure of the aggregates varies significantly. The famous space-filling "house of cards" flocculated structure of clays is formed as a result of the positive edges attaching to the negative faces (Figure 1.2a). The faces of the particles can also attach to each other and form particle aggregates (Figure 1.2b). These particle aggregates can be either dispersed or form bigger flocs and hence increase the volume of the structured system.

1.5. Surface Phenomena

Different properties of the particle surfaces in colloidal systems can give rise to various types of interactions between the particles. The following sections discuss the phenomena that can affect particle association in clay-liquid systems as well as their effect on flow properties of their suspensions.

1.5.1. Electric Double Layer

Interaction of charged species in an electrolyte solution is greatly affected by a phenomenon known as electric double layer formation. When a charged surface is in an electrolyte solution, ions carrying a charge opposite to that of the surface are electrostatically attracted towards it and form an electric double layer near the surface. Different models such as Gouy-Chapman or Stern models predict the distribution of these

7

electrolyte ions, also known as counter ions, near the surface of a charged particle. The details of these models are given in reference [10]. In general, the ions are distributed in such a way that balances the charge on the surface. Figure 1.3 shows the structure of electric double layer for a negatively charged surface according to the Stern model. The potential distributions in different layers of this electric double layer are labelled in Figure 1.3. As seen in the figure, there is a linear decrease in the electric potential in a layer immediately across the charged surface. This region is known as the Stern layer. Electric potential at the end of the Stern layer (away from the particle surface) reaches the Stern potential and decreases exponentially thereafter. In the Stern layer, the ions are believed to be bound to the particle surface. It is not until a distance away from the Stern plane where the ions and the ion bearing electrolyte solution can flow around the particle. The plane at which fluid flow initiates is known as the shear plane. For surface characterization measurements, it is customary to interpret the potential to be at the shear plane. This is the plane at which the no-slip flow boundary condition applies. The potential at the shear plane is known as the zeta potential (ζ).

The charge distribution in the electric double layer is such that the particle-double layer system, as well as the bulk electrolyte solution, are electroneutral. Within the double layer region, however, electrolyte type and ion concentration can alter the electric potential profile. As a result, particle zeta potential also varies with electrolyte type and ion concentration [10]. The magnitude of electrostatic forces between the particles in a suspension depends on the distribution of ions in the double layer. One can change particle interactions by changing the chemical composition of the suspending medium. In clay dispersions, for example, the presence of positive ions such as divalent calcium ions can reduce the repulsion between the particles significantly. With lower electrostatic repulsion between the solids, particle agglomeration due to the universal attractive van der Waals forces has a higher possibility.

1.5.2. Surface Wettability

When a liquid droplet is placed on a flat solid surface, it may spread over (wet) the surface completely or remain as a droplet. Figure 1.4a shows a liquid droplet on a solid

8

surface in air. Surface wettability of the solid can be measured through the contact angle, θ. In the given system in Figure 4.1a, higher contact angles would represent a lower tendency of the liquid droplet to spread and wet the surface.

Based on the wettability of a surface by either water or oil, it is customary to define hydrophobic and hydrophilic surfaces. Figure 1.4b shows an oil droplet on a solid surface in water. Note that in the presence of two different liquid phases, the contact angle is defined as that through the water phase. In the system of Figure 1.4b, small contact angles would indicate that the solid surface is hydrophilic. Larger contact angles on the other hand would indicate hydrophobic surface properties.

Surface wettability can be affected by a number of factors. Surface active agents can change the surface tension of the phases involved and considerably affect the contact angle of the surface. Depending on whether a liquid droplet is advancing on a dry surface or receding from a wet surface, different angles could be measured. Such a phenomenon is known as contact angle hysteresis. Surface roughness is also responsible for causing contact angle hysteresis. In addition, surface preparation methods can alter the measured contact angles as well. For example, preparing a crystalline solid in the presence or absence of water can change the surface properties and result in different contact angles. In this case, entrapment of water in the solid crystal can be the cause of the problem [11].

In clay systems, surface wettability of the solids can alter the manner in which particles associate with each nother. When the system is in contact with oil, polymeric agents in oil* can act as bridges between hydrophobic surfaces and cause particle flocculation (Figure 1.5). Bridging the particles together can result in stronger flocs as compared to aggregate formation through salt addition. This is because particle agglomeration is caused by the weak van der Waals forces while bridging flocculation is due to much stronger physical links between the particles [12].

---

* Asphaltene aggregates can have bridging effects in oil sands systems.

9

1.6. Consequences of Particle Association on Flow Properties

Flow properties of a dispersed system are directly affected by the interactions between the particles. In dilute systems where the distances between the particles are relatively large, inter-particle forces do not alter the flow properties significantly. However, once the particle concentration increases, the distances between the particles become shorter. In the range where particle interaction forces are active, the solids can form a rigid network. Such particle linkage is observed in the form of elevated effective viscosity or finite yield stresses in the dispersed system. Therefore, any variable affecting particle interactions can also change the bulk flow properties. In a dispersion of smaller solid particles for example, due to smaller net repulsion between the particle surfaces, rigidity of the solids network is higher and higher viscosities are observed.

The following section discusses those flow properties that can provide us with more information about particle associations and network structures in solid liquid dispersions.

1.7. Rheology of Solid-Liquid Dispersions

The term "rheology" is by definition the study of flow and deformation of matter [13]. The primary variables in rheology arise from the studies of Robert Hooke and Isaac Newton on solids and liquids. Robert Hooke related the tension (stress) of a spring to its infinitesimal extension (deformation) by a spring constant. With focus on liquids, Newton defined viscosity as a resistance to the rate of deformation (as opposed to deformation for elastic solids). He found that this resistance was proportional to the velocity gradient. The experiments of Newton and Hooke established the relations for two extremes of material behaviour, namely, ideal solids and ideal liquids.

Hooke's law for an elastic solid relates stress and deformation through the equation $\tau = G\gamma$. In this equation, τ is stress that is equal to force per unit area, γ is deformation and G is the proportionality constant or elastic modulus [14]. Through Newton's law of viscosity, the relation between shear stress (τ) and rate of deformation or shear rate ($\dot{\gamma}$)

10

can be written as $\tau = \mu \dot{\gamma}$. Here, the coefficient relating shear stress and shear rate is known as the liquid viscosity (μ).

For most materials, however, ideal behaviours described by the two researchers are not observed. Viscosity (μ) and elastic modulus (G) are more than simple coefficients and can vary with deformation or shear rate. As such, more complex correlations appear to be required for more realistic material behaviour. There are, however, some cases where materials do behave effectively as ideal substances. A liquid that has a constant viscosity over a range of shear rates is said to have Newtonian behaviour, whereas liquids showing variations in viscosity with shear rate have non-Newtonian behaviour. For materials having non-Newtonian behaviour, an apparent viscosity is defined as the ratio of shear stress to shear rate. The most common non-Newtonian characteristic is the appearance of yield stress (τ_y) where the material shows an initial resistance against flow. Materials with yield stress do not flow until the applied shear stress reaches their yield level.

In solid-liquid dispersions, such as clay-in-water suspensions, a reduction in apparent viscosity with increasing shear rate (shear thinning) is often observed. In such suspensions, the viscosity can be affected by the colloidal interactions between the solids. Where there is an attractive force between the solid particles, floc formation and entrapment of the suspending medium between the particles increase the volume occupied by the solids. The higher volume percent will lead to viscosities higher than what would normally be expected. For particles carrying identical surface charges, repulsion between the particles will position them at distances where an equilibrium state is achieved. In order to cause flow in a system of repelling particles, the equilibrium first needs to be interrupted. Therefore, there will initially be an augmentation to the low shear viscosity of such suspensions. As the shearing becomes sufficiently intense, the structures formed among the solids, either due to preferred orientation of the particles or breakage of flocs. This leads to decreased viscosities. The reduction in viscosity, however, is limited to the point where solid particles in the system begin to rearrange and obtain a newly adapted arrangement which leads to increased viscosity (shear thickening). Figure 1.6 schematically represents the described behaviour [13].

11

In addition to changes in viscosity due to variations in material properties, time can also have an impact on sample viscosity. In a solid-liquid dispersion where reconstruction of structures is time-dependent, viscosity will be time-dependent and can result in hysteresis loops in flow behaviour. At constant shear, increase in viscosity with time is known as thixotropy. If viscosity decreases with time at a given shear rate, the behaviour will be referred to as anti-thixotropy or rheopexy [13].

Another very common material behaviour is viscoelasticity. Depending on the timescale of experimental measurements, an intermediate behaviour displaying both solid-like and liquid-like characteristics is observed for some real materials. Such material behaviour is known as viscoelasticity. In a given sample, viscoelasticity can be measured by applying a step deformation and measuring the stress response. In such a test, known as stress relaxation, the response of a viscoelastic material is a gradual decrease in stress, whereas in liquids stress will relax immediately after strain is constant[†] and in solids there will be no relaxation at all [14]. In solid-liquid dispersions where a preferred particle arrangement exists, a tendency to maintain the original arrangement will always be present in response to small disturbances. Rearrangement of the particles back to their favourable locations will be observed as a gradual relaxation of applied stress. Viscoelastic behaviour is a typical behaviour of clay-in-water dispersions.

For viscoelastic materials, a relaxation modulus can be defined as $G(t) = \tau(t) / \gamma$. Note that the relaxation modulus is time dependent while Hooke's elastic modulus is a constant. In short time intervals, the relaxation modulus can have a linear dependence on deformation. This region of material behaviour is known as linear viscoelasticity. One of the simplest models for linear viscoelasticity is the Kelvin model. This model assumes that the viscoelastic behaviour is a result of parallel combination of an elastic solid and a viscous liquid. Therefore, the model gives stress as $\tau = G\gamma + \mu\dot{\gamma}$ [13].

[†] Note that according to Newton's viscosity law, ideal liquids will resist step deformation by infinite stress. However, as instant deformation is not achieved in reality, only a steep rise in the liquid stress response will be observed before it relaxes and reaches zero stress.

12

A common practice to characterize viscoelastic material behaviour in terms of its solid-like or liquid-like contributions is by conducting small strain oscillatory tests in their linear viscoelastic region. Typically, in such a test, a sinusoidal deformation in the form of equation 1.1 is applied to the material:

$$\gamma = \gamma_0 \sin(\omega \cdot t) \tag{1.1}$$

After several oscillations, the stress response will also oscillate at the same frequency. Relative to the applied strain, however, the stress will show a phase lag according to the relation

$$\tau = \tau_0 \sin(\omega \cdot t + \delta) \tag{1.2}$$

In equations 1.1 and 1.2, τ_0 and γ_0 are the stress and deformation amplitudes, respectively. The stress response in equation 1.2 can be decomposed to two components: one in phase and one 90° out of phase with the applied deformation, i.e.

$$\tau = \tau' + \tau'' = \tau_0' \sin(\omega \cdot t) + \tau_0'' \cos(\omega \cdot t) \tag{1.3}$$

Equations 1.2 and 1.3 will result in $\tau'' = \tau_0 \sin \delta$ at $\omega.t = 0$ and $\tau' = \tau_0 \cos \delta$ at $\omega.t = \dfrac{\pi}{2}$.
We can then write

$$tan\ \delta = \tau''_0 / \tau'_0 \tag{1.4}$$

Writing stress in the form of equation 1.3 suggests the definition of two dynamic moduli as [14]

$$G' = \tau'_0 / \gamma_0 \quad \text{and} \quad G'' = \tau''_0 / \gamma_0 \tag{1.5}$$

Defining a complex viscoelastic modulus $G^* = G' + iG''$ so that [14]

13

$$\tau_0 = |G^*| \, \gamma_0 \qquad\qquad (1.6)$$

Therefore, we can write

$$\tau_0 = |\tau_0' + i\tau_0''| \qquad\qquad (1.7)$$

Substituting equations 1.7 and 1.4 into equation 1.2 leads to

$$\tau = G'\gamma_0 \sin(\omega \cdot t) + G''\gamma_0 \cos(\omega \cdot t) \qquad\qquad (1.8)$$

The in-phase modulus in equation 1.8, G', is known as the storage modulus or elastic modulus. It represents the solid-like characteristic of a material. The viscous or liquid-like characteristics of such matter can be measured through the out-of-phase coefficient, G'', which is known as the viscous or loss modulus. G'' is a measure of the energy dissipated per cycle of deformation per unit volume [14].

The relative values of G' and G'' can indicate which part of material behaviour is more prominent. When G' is higher than G'', the solid like properties are more significant. Liquid-like properties are more important when G'' is higher that G'. The dynamic moduli, G' and G'', are measured through an oscillatory frequency sweep test. Figure 1.7 shows the typical responses that can be expected in a frequency sweep. These measurements are particularly of interest in characterizing solid-liquid dispersions where inter-particle interactions can change the suspension from a very fluid system to a strong solid-like gel.

Figure 1.8 gives a summary of the rheological variables discussed thus far. As stated earlier, these parameters are a matter of interest to the oil sands researcher since many of the aspects of the extraction process are directly affected by the rheological properties of the solids suspensions.

14

1.8. Previous Studies on Oil Sands Suspensions

1.8.1. Gelation

Schramm used an in-situ approach to measure the viscosity of the middling zone in a commercial separation vessel [15]. A vibrational viscometer was placed in the middlings zone and the viscosities were measured at different pH and positions in the separation vessel. Using the Stokes equation, Schramm found that high bitumen rise velocities and recoveries were realized for low fines content, a certain pH range and locations in the gravity separation vessel. Chong et al. [16] showed that high fines content in oil sands ores reduced bitumen recovery. Sparks et al. [17] suggested that under certain conditions, organic-rich bi-wettable ultra-fines and hydrophilic ultra-fines can interact strongly to form a gel and cause gravity separation vessel sludging. More recently, Tu et al. [18] provided more useful insight into the gelation problem with ^{2}H NMR and jar tests on ultra-fines separated from oil sands and waste unit samples. Their study further established that, given the right water chemistry, sludging conditions will be reached when ultra-fines in the slurry exceed a certain concentration. They also found that at 460 ppm of sodium ions in water, only 1.5 wt% of particles smaller than 0.3 micron is sufficient to cause gelation as compared to 16 wt% for 10 micron particles. Chow [19] used inter-bedded clays and rheology to map gelation propensity at different sodium and calcium ion concentrations, ultra-fine solids concentrations and shear history.

The aforementioned studies suggest that gelation can be due to a combination of the following factors: high solids content, high ultra-fines content, high electrolyte concentration and the presence of swelling clays. Ultra-fine clays modify the rheological properties of oil sands slurry and middlings due to colloidal inter-particle forces.

1.8.2. Tailings Settling

Angle et al. [20] used ultra-centrifugation to separated different layers of solids from oil sands tailings. Their results showed that solids containing different amounts of bound organic matter had different slurry elasticities. The largest elastic properties were observed for the fraction of solids containing the maximum amount of organic matter. In general, it is believed that the organic material associated with oil sand solids has an

15

important impact on oil sands tailings [21-24]. Majid and Sparks [25] separated two different solid fractions from fine tailings. Solids in one fraction contained a higher amount of organic matter and were predominantly hydrophobic. The other fraction contained less organic matter and showed biwettabilty as opposed the hydrophobic nature of the former fraction. Majid and Sparks showed that in the presence of bitumen in their systems, the separated solids had the capacity of forming flocculated structures with strong non-settling characteristics. Majid et al. [26] separated toluene insoluble organic material from a non-settling fraction of oil sands tailing. The average elemental composition of the separated material was similar to that of solvent extractable humic acids. Based on the aromaticity of the separated organics, they also suggested that these materials may have been originated from the oil sands feed and were not formed by the process.

1.9.   Objectives of Present Work

In order to overcome the issues associated with gel formation and hold-up of water and hydrocarbon in the tailings stream, a better understanding of surface properties and interactions of ultra-fine particles is required. For the purpose of this study, rheological measurements are utilized to determine the effect of particle size on the flow properties of oil sands slurries. Our main focus is to identify the ultra-fine fraction which has the highest impact on the rheology of oil sands slurries. The flow behaviour of ultra-fine clay suspensions is a direct measure of particle interactions. Critical gelation conditions in terms of solids content and solution chemistry of the solids are determined. Characterization measurements on the solid particles of interest are performed to identify the nature of different interactions between the solids.

16

To Froth Treatment

Feed Slurry

● Bitumen

◖ Air Bubbles

✦ Coarse Sands

Froth

Middlings

Tailings

To Tailings Recovery
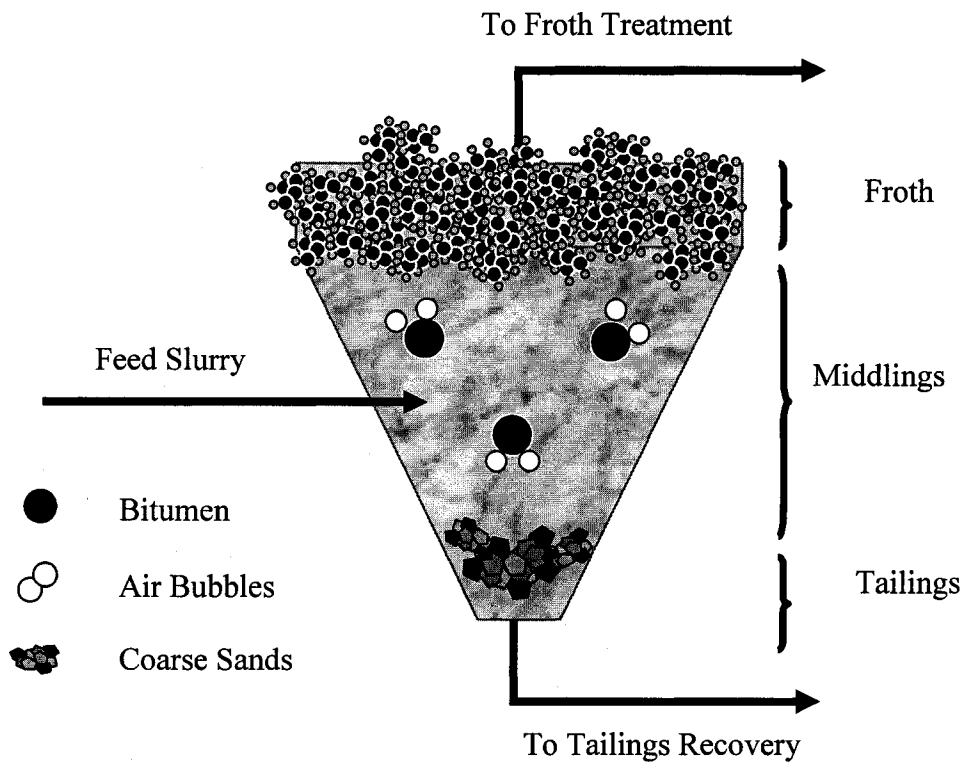
Figure 1.1 – Gravity separation vessel

17
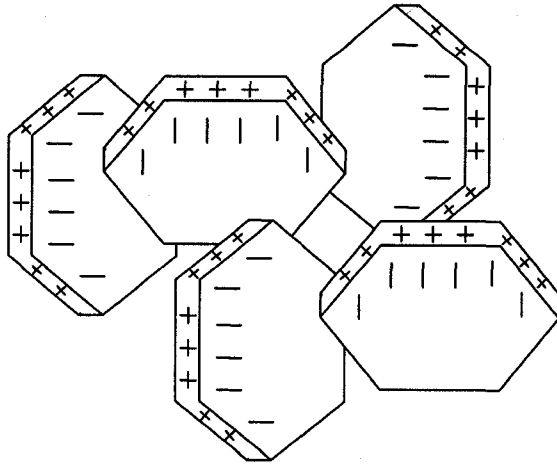
a) Flocculated Particles   b) Aggregated Particles
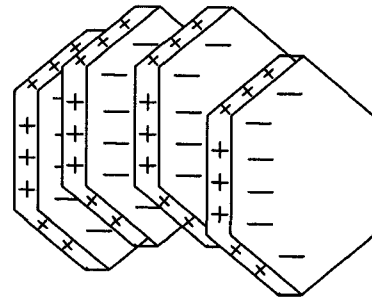
Figure 1.2 – Two different modes of particle association for clays.

18
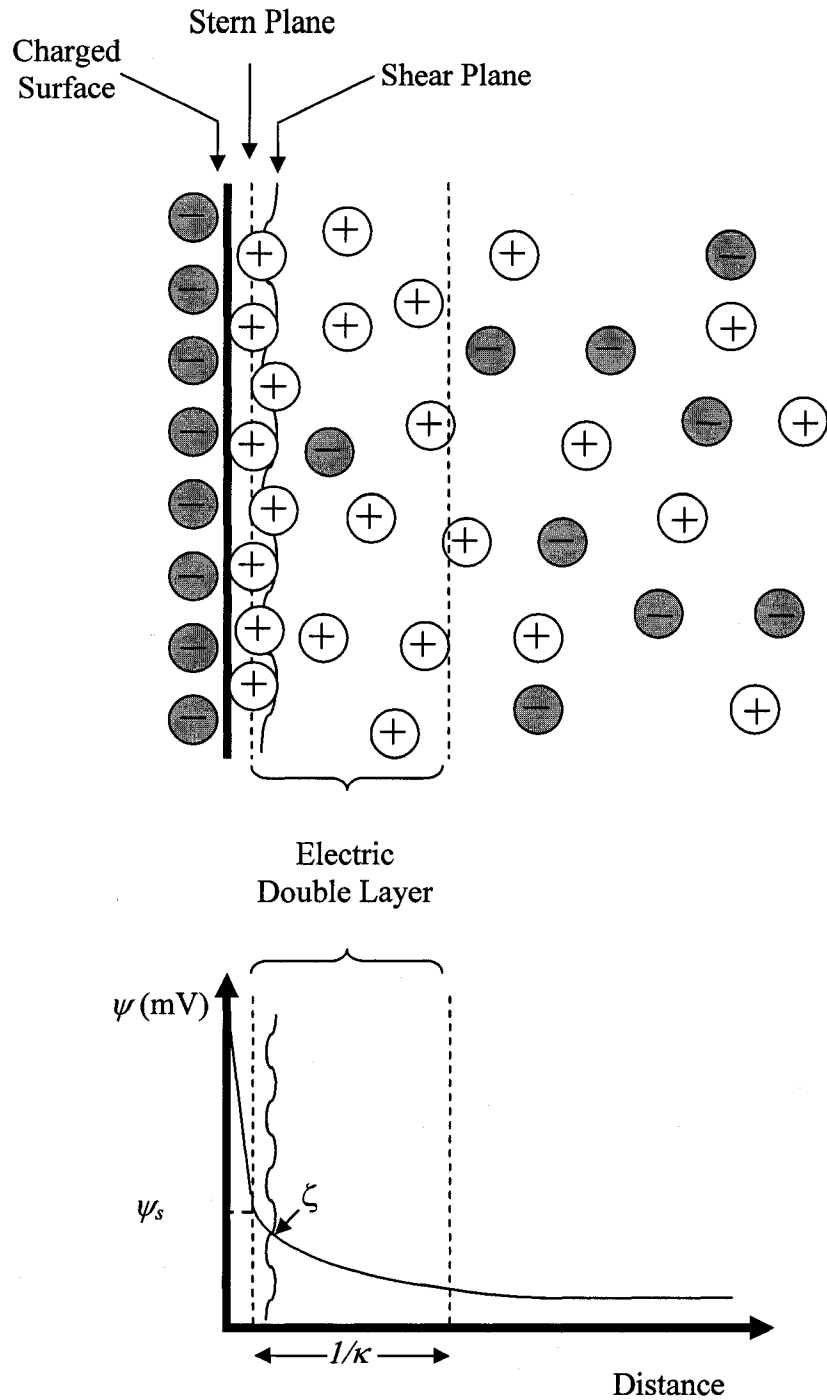
Figure 1.3 – Schematic illustration of an electric double layer across a negatively charged surface and profile of electric potential distribution away from the surface according to the Stern model.
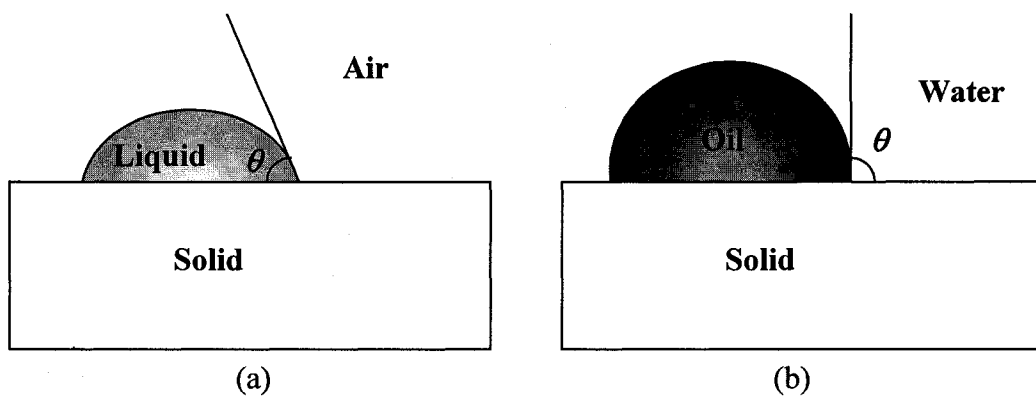
Figure 1.4 – Contact angle for a) liquid droplet on solid in air b) oil droplet on solid in water
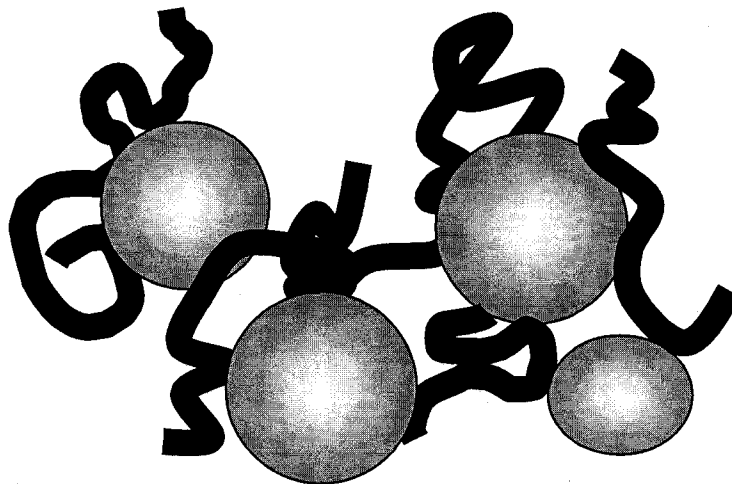
Figure 1.5 – Bridging of hydrophobic particles by polymeric oil strands.

20
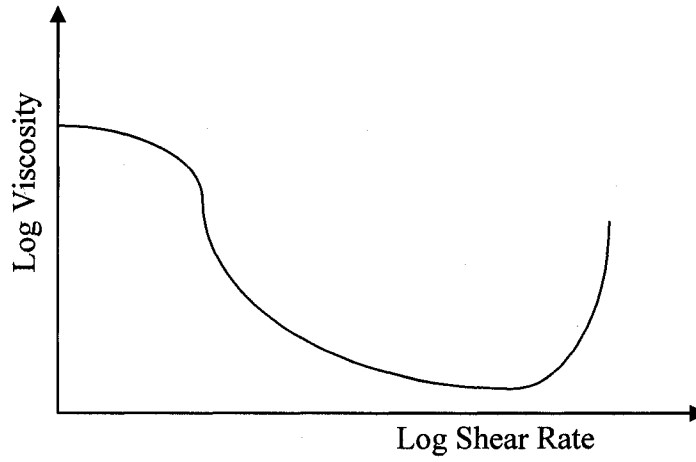
Figure 1.6 – Schematic flow curve of a concentrated solid-liquid dispersion.
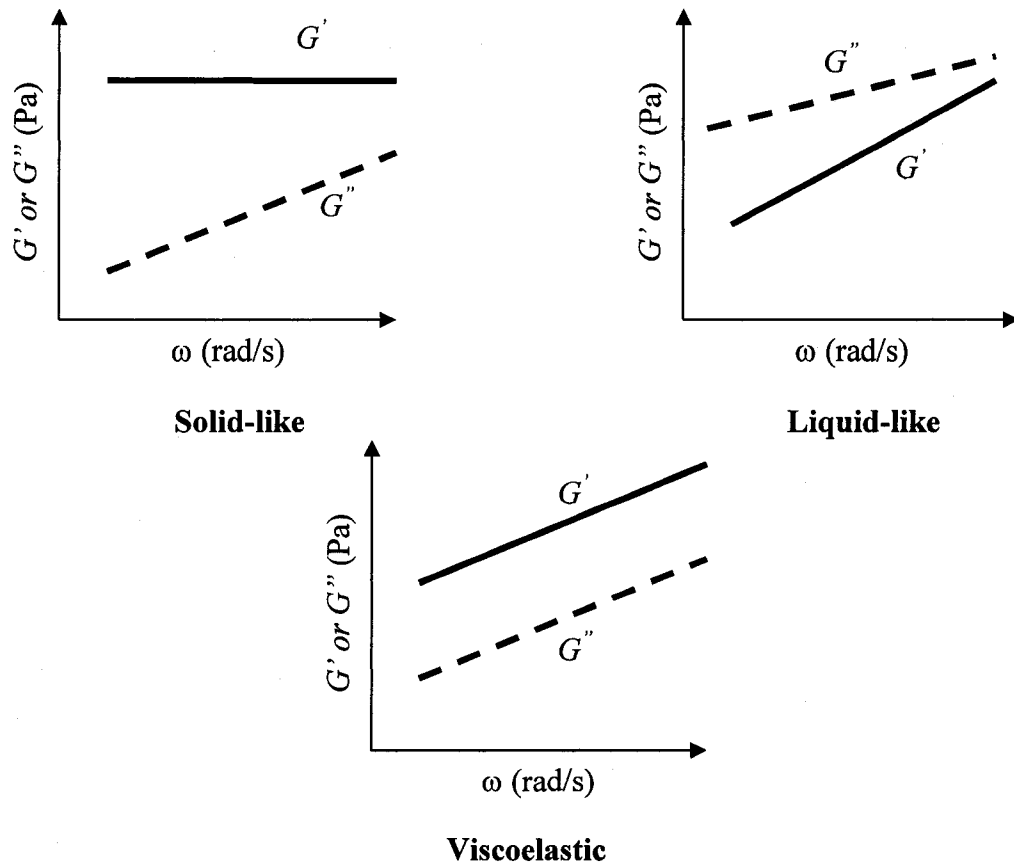
Figure 1.7 – Typical responses observed in a frequency sweep test.
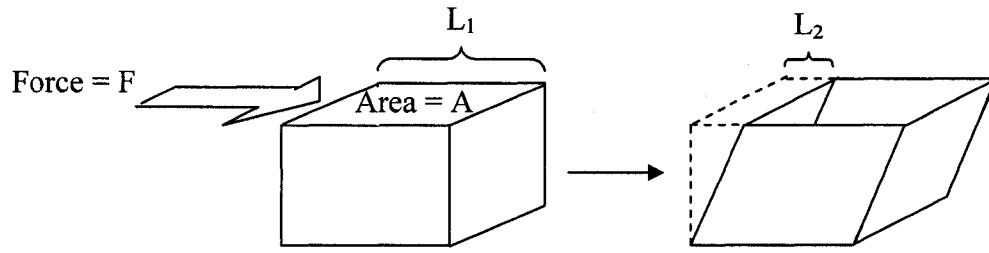
Stress $\tau = \dfrac{F}{A}$ Deformation $\gamma = \dfrac{L_2}{L_1}$ Shear Rate $\dot{\gamma} = \dfrac{\Delta\gamma}{\Delta t}$

Viscosity $\mu = \dfrac{\tau}{\dot{\gamma}}$ Elastic Modulus $G = \dfrac{\tau}{\gamma}$

$\tau = \tau_0 \sin(\omega t + \delta)$

$\gamma = \gamma_0 \sin(\omega t)$
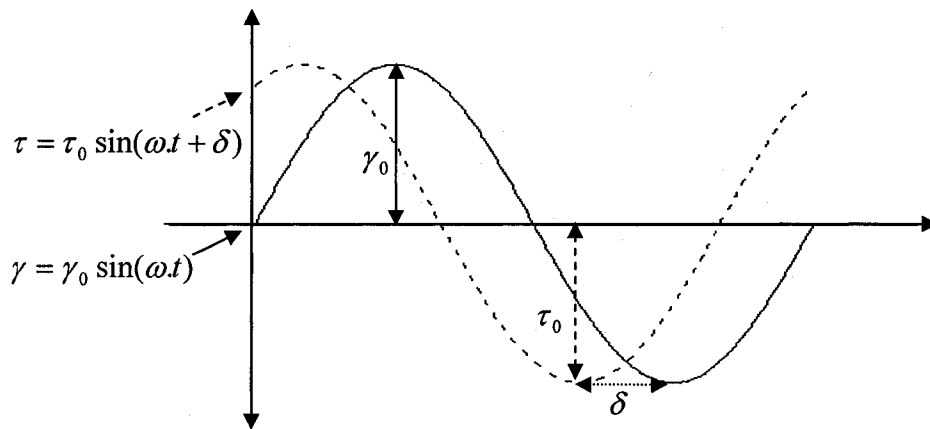
Complex Elastic Modulus $G^* = G' + i\, G''$; $|G^*| = \dfrac{\tau_0}{\gamma_0}$
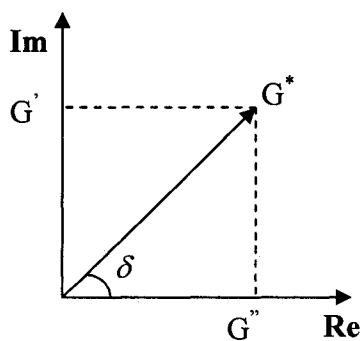
Storage (Elastic Modulus) G'

Loss (Viscous) Modulus G''

Figure 1.8 – Summary of the rheological properties
of interest to the experiments in this work.

22

2. Experimental

2.1. Materials Used

Tailings and middlings from Syncrude Canada and Shell Canada were used as the source of the solids. Ultra-fine particles were separated from these suspensions following a procedure described in Section 2.3.

For dilution purposes and electrolyte preparation, Millipore deionized water with less than 0.2 $\mu S/cm$ conductivity was used.

Anhydrous calcium chloride pellets from Fischer were used as the source of calcium ions. All electrolyte solutions were prepared daily as needed for the experiments. Potassium bromide salt from Aldrich was used for FTIR experiments. Hydrogen peroxide from Aldrich was used to wash some of the solid particles used in the experiments. All the chemicals used were of analytical grade.

2.2. Equipments

2.2.1. Rheometer

For rheological measurements, the ARG2 rheometer from TA Instruments was used. In all rheological measurements, a cone-and-plate (2°, 60 mm) geometry was used. Cone-and-plate geometry is suitable for measurements of low and high viscosity materials. This choice of geometry would also allow for measurements with small quantities of sample. To avoid drying during the experiments, an integrated solvent trap was used to maintain the sample at the vapour pressure of its suspending medium. Figure 2.1 schematically represents the cone-and-plate geometry, together with the solvent trap.

Figure 2.2 shows a cone-and-plate geometry and its corresponding spherical coordinates. With the assumptions given in reference [14], the working equations of the cone-and-plate geometry can be written as follows:

23

$$\tau_{\phi\theta} = \frac{3M}{2\pi R^3}$$ (2.1)

In this equation, $\tau_{\phi\theta}$ is the stress component on a surface normal to the ϕ axis and in the θ direction, M is the applied torque on the rotating shaft and R is the cone diameter. For this geometry, the applied strain is uniform throughout the sample and is given by

$$\gamma = \frac{\phi}{\beta}$$ (2.2)

In equation 2.2, ϕ is the rotation angle and β is the cone angle which is constant. From equation 2.2, the shear rate can be defined as

$$\dot{\gamma} = \frac{\Omega}{\beta}$$ (2.3)

In equation 2.3, Ω is the angular velocity of the rotating cone ($\frac{\phi}{t}$).

Figure 2.3 shows the drive unit of the rheometer. In this system, the motor applies a torque and controls the speed and oscillation frequency. The magnetic thrust bearing provides effectively frictionless axial support of the drive shaft and geometry. This system allows for measurements at torques as low as 3 $nN.m$ to probe delicate material structures.

2.2.2. ZetaPALS

Brookhaven ZetaPALS was used for zeta potential measurements. This instrument has the capability of performing measurements on samples of high salt concentrations and conductivities. Sample quantities, as small as 2 mL, are sufficient for accurate zeta potential measurements of any transparent colloidal systems.

24

ZetaPALS determines zeta potential using phase analysis light scattering (PALS) technique. PALS utilizes two laser beams with a small frequency difference (ω_s) that cross in an interference region where particle mobility is measured. A particle at fixed position in the interference region will scatter light with an intensity varying with frequency ω_s and with an arbitrary but fixed phase shift relative to the reference signal. Any particle translation will cause a time-dependent phase shift of the scattered light which can be directly related to the particle movement [27].

2.2.3. Thermal Analyzer

Thermal analysis was performed using the STA 409 PC Luxx thermal analyzer by Netzsch Instruments. With a top loading balance that detects mass changes of the sample, this TG analyzer has high sample capacity of 18 g and is capable of reaching 1550 $°C$.

2.2.4. FTIR[‡] Spectrometer

BioRad FTS6000 was used for infrared spectrometry. This instrument enables recording of infrared spectra of solids and gases. It can cover the spectral range of 11,000 to 400 cm^{-1}.

Figure 2.4 shows a block diagram of a Fourier transform system. The source sends a beam containing a complete range of infrared frequencies into the interferometer I. The beam is first divided at the semitransparent beam splitter BS, which transmits half to the variable plane mirror M_V and reflects half to the fixed plane mirror M_F. The separate beams are returned by M_V and M_F to the beam splitter where they are recombined after having travelled distances differing by some amount L which is continuously variable. The recombined beams interfere at BS, where they are partially reflected and sent out of the interferometer to the sample S. After passing through S, the radiation is converted to an electric signal at the detector det. This output is processed electronically at A, stored in the computer memory and then transformed to the spectrum by Fourier transform processing. The spectrum is read out in a suitable form, for example, as a plot on the chart recorder CR of percent transmission versus frequency [28].

[‡] Fourier transform infrared

25

In the FTS 6000 FTIR spectrometer, a single beam He-Ne laser is first passed through a beam splitter to collect the spectrum of the source. The sample is inserted in the instrument. To obtain the desired sample spectrum, absorption due to the sample is collected and ratioed against the source. During a scan, all the experimental conditions (source, sample, detector, etc.) should remain constant; otherwise, artifacts will be present in the resulting spectrum.

2.2.5. Particle Size Analyzer

Malvern Mastersizer 2000 was used to measure the particle sizes of the solids. The instrument uses laser diffraction technique to measure the particle size distribution (PSD). Laser diffraction is based on the principle that particles passing through a laser beam will scatter light based on particle sizes. The intensity of the scattered light is also proportional to the particle size. Large particles scatter light at narrow angles with high intensities whereas small particles scatter light at wider angles but with low intensities.

Other than scattering of light in laser diffraction, phenomena such as transmission through the particle are possible and will affect the measurements. To account for such phenomena in the measurements, knowledge of the refractive index of the sample is required [29].

To keep the samples well dispersed during measurements, a dispersion unit with a controllable stirrer is attached to the instrument. Particle sizes can be measured in a suitable liquid. The amount of sample required for each measurement is specified online by the instrument software. The results have a continuous format of volume percent of particles in the size range between 0.2 μm and 2000 μm.

2.2.6. Drop Shape Analyser

Krüss drop shape analyser was used for contact angle measurements. This instrument allows for automatic and manual adjustments of the system and measurements. Contact angles from 0 to 180 degrees can be measured with 0.1 degree of accuracy. An integrated video system incorporated in the software can record the details of the

measurements. Evaluation of the drop image takes place in the video window of the software, where the baseline is determined automatically. For measuring the contact angle, several automatic methods are available.

2.3. Solids Fractionation

Experiments were performed on ultra-fine solids separated from mature fine tails and middlings suspensions provided by Shell Canada and Syncrude Canada. In what follows, the procedure applied in this study for separation of ultra-fines from an MFT suspension is described. Figure 2.5 shows the fractionation scheme for MFT. A similar procedure was applied to separate the solids from the middlings.

As networked structures of solids are formed in MFT over time, separation of the ultra-fines requires breaking the linkages between the particles. Decreasing ionic concentration of the suspending medium would reduce the attraction between the solid particles and facilitate separation of the solids due to their density difference. For this, deionized water was added to the MFT at a 4:1 volume ratio of water to MFT. As such, structures in the suspension were broken. With about one hour of settling time, the diluted suspension segregated with the coarse solids settled to the bottom. At this stage of settling, some of the trapped bitumen among the solid particles was released and floated to the top of the container. This bitumen was skimmed off and separated from the solids. The solids remained in the suspension up to this point were mostly fine particles.

The dilute suspension of fine particles was separated from the coarse sediments by decantation and transferred to a different container (suspension A in Figure 2.5). To isolate the ultra-fine solids, suspension A was passed through 75, 45 and 20 μm sieves. Sieving the suspension removed a considerable amount of minute bitumen droplets trapped in the solids networks. Figure 2.6 shows the particle size distribution of the sieved suspension (<20 μm). As the figure shows, two separate peaks (0.2 μm and 5 μm)

27

appeared on the PSD[§] of suspension A after sieving. This meant that the particles at this stage were predominantly of the above mentioned sizes.

The sieved suspension was left to settle for 48 hours in order to fractionate the solids of the two peak sizes shown in Figure 2.6. After two days, a layer of sediments appeared in the bottom of container B in Figure 2.5. In this study, the B sediments were referred to as fraction 1. These sediments were separated from the suspension above of it. The upper suspension was further diluted and allowed to settle in graduated cylinders for another 24 hours. This final stage of settling would release more of the solids that formed the B sediments. Figure 2.7 shows the PSD of B sediments and the suspension separated from it. The results in this figure show that the solids forming the peaks of Figure 2.6 were successfully separated. To this point, two fractions of ultra-fine solids, with PSDs as shown in Figure 2.7, were separated.

The focus of this study was to investigate the role of ultra-fine solids in altering the rheological properties of oil sands suspensions. Changes in alterations in water chemistry of the suspension may lead to rheological behaviours that are not representative of actual industrial conditions. Therefore, the water chemistry of the suspensions was to be preserved. To that end, the deionized water introduced during the fractionation had to be replaced by the suspending medium of the original MFT suspension. This was achieved by washing the separated solids with MFT supernatant water. Centrifuging MFT at 10,000 rpm[**] and $4\,^{\circ}C$ released a clear supernatant that was used to return the solids to their original water chemistry.

The separated solids suspensions were centrifuged at 10,000 rpm and $4\,^{\circ}C$ in order to separate the solids from the water used during fractionation. However, once the suspension in C was centrifuged, a two-layered sediment appeared in the centrifuge

---

[§] Particle size distribution
[**] Revolutions per minute

28

bottles[††]. In this study, the bottom layer, with a light shade of gray, is referred to as fraction 2; and the top layer, with a darker color, is referred to as fraction 3. The layers were separated and washed independently with MFT supernatant.

Figure 2.8 shows the particle size distribution of the separated solid fractions. The mean particle sizes of fractions 1 to 3 are 5.96, 0.14 and 0.16 μm, respectively. Photographs of these three ultra-fine fractions are shown in Figure 2.9.

Stock samples of each fraction were prepared after washing and redispersing the solids in MFT supernatant. These stock samples were used in all experiments to prepare suspensions of desired concentrations. Desired solid concentrations were achieved by adding appropriate amount of isolated MFT water to the stock samples.

Total solids concentrations in the suspensions (wt%) were measured by drying the suspensions in a vacuum oven until no further weight loss was observed. In the instances where dry particles were required for the experiments, suspensions were dried in the vacuum oven (-10 kPa) for 30 minutes. The agglomerates formed as a result of heating were crushed manually by mortar and pestle.

2.4. Experimental Procedures

2.4.1. Ultra-fine Solids Mineralogy

Mineralogy of the oil sands ultra-fines was determined by X-ray diffraction (XRD). Ultra-fine solids were separated from tailings and middlings through dilution with deionized water followed by settling. Calcium saturated oriented slides of these ultra-fine solids were prepared following the procedure described in reference [30]:

[††] Appearance of the separate layers in the sediment indicates different settling velocities of the particles. Based on Stokes formula $V_t = \dfrac{[(\rho_s - \rho)gD_P^2]}{18\mu}$ for settling velocity of spherical particles in a medium of viscosity μ and density ρ, the particles appeared to differ either in size (D_p) or density (ρ_s).

29

Suspensions of 2 wt% total solid concentration were prepared from MFT and gelled middlings ultra-fines. Four millilitres of these suspensions were filtered through membrane filters of 0.45 μm pore size. As the suspension passed through the filter, 3 to 5 mL of 0.1 M $CaCl_2$ solution was passed through the solids. Finally, about 5 mL of deionized water was passed through the solid cake to wash the excess of calcium ions from the oriented particles. To prepare glycolated slides, the solids cakes were placed in a desiccator containing ethylene glycol and heated to 60 °C. After 6 hours of heating followed by a stage of thermal equilibration at room temperature, the slides were ready for XRD. Identification of the particle mineralogy was completed by performing XRD on calcium saturated slides at 54 % relative humidity. To reach this level of relative humidity, the slides were placed in a desiccator containing water and $MgNO_3$ salt for 24 hours.

To identify the mineral components of the three ultra-fine fractions separated from MFT, calcium saturated slides of the solids were prepared following the same procedure described above.

2.4.2. Rheology

Flow and oscillatory tests were consecutively performed on suspensions of fractions 1 to 3. Samples were prepared at different total solids concentrations. Table 2.1 summarizes the procedure followed for all rheological experiments. Prior to each test, all suspensions were pre-sheared at 1500 s^{-1} and equilibrated for 10 s to avoid shear history effects and to achieve reproducible results.

Rate-controlled flow tests were performed to measure the viscosities and yield stresses of the suspensions. Oscillatory strain sweep tests were used to determine the linear viscoelastic region of each sample without disturbing the structures of the suspensions. Oscillatory frequency sweep tests performed in the linear viscoelastic region determined the solid-like characteristics and gel strength of all samples.

30

Rheological tests were performed in two different water chemistries. Initial experiments were performed on particles dispersed in MFT supernatant water. However, in other tests, calcium chloride solutions[‡‡] were added to the solids to observe the effect of calcium ion on the rheology of the separated solids. In these instances, 15 wt% suspensions of total solids concentration were prepared by adding the desired calcium chloride solution to a stock sample of 30 wt% solids dispersed in MFT supernatant.

2.4.3. Water Chemistry

Ion concentrations in the suspending medium of MFT, as well as the three solid fractions separated from it, were measured by atomic absorption (AA) spectroscopy. The suspending water was obtained by centrifuging each suspension at 20,000 rpm and 4°C. For suspensions of fractions 1 to 3 in calcium chloride solutions, the water was separated within 30 minutes of suspension preparation.

2.4.4. Zeta Potential Measurements

For zeta potential measurements of the three solid fractions in their original water chemistry (i.e. MFT supernatant), one to two droplets of a 2 wt% suspension were redispersed in 5 mL of the suspending medium.

Zeta potential was also measured for the solids dispersed in calcium chloride solutions. The solids of each fraction were dispersed in 1:1 (by volume) suspension of MFT supernatant and calcium chloride solutions. Each test was composed of three consecutive measurements of five cycles and twenty runs. To evaluate the zeta potential from the measured mobility values, the Smoluchowski model was used. This model is suitable for samples of large κa where, κ is the inverse Debye length and a is particle diameter [11].

2.4.5. FTIR Spectroscopy

A disc of KBr salt was scanned first to obtain the infrared spectrum of the beam source. For ultra-fine clays, the spectrum was obtained by scanning dry particles in a mixed form

---

[‡‡] 20 , 60, 100, 500 and 1000 ppm calcium chloride solutions were prepared by adding the corresponding milligrams of $CaCl_2$ to 1 L of deionized water.

with KBr. Dried ultra-fine powders were intimately mixed with potassium bromide (1:100 solids to salt mass ratio) and formed into a disc for infrared scanning.

2.4.6. Contact Angle Measurements

For contact angle measurements of ultra-fine clays, flat surfaces were prepared by filtering 5 mL of 2 wt% suspensions of the three MFT ultra-fine fractions through membrane filters of 0.45 μm pore size. The particle cakes were dried overnight in a humidity desiccant. Contact angles were measured for the particles surfaces using MFT supernatant in air.

2.4.7. Thermogravimetric Analysis

Dried powders of the MFT ultra-fine fractions were prepared by heating the suspensions in a vacuum oven (30 min, -10 kPa) followed by crushing of agglomerates by mortar and pestle. The dried powders were then placed in sealed alumina crucibles and heated over one hour from room temperature to 600 °C in a nitrogen gas environment.

2.4.8. Scanning Electron Microscopy

One droplet of a 1 wt% suspensions of MFT ultra-fine fractions was placed on carbon tapes. The particle suspending medium was evaporated in a humidity desiccant. Ultra-fine particles on the tape were then coated by gold rendering their surfaces conductive which allowed for SEM imaging.

2.4.9. Surface Force Measurements[§§]

A Nanoscope E AFM (Digital Instruments, Santa Barbara, CA) with a vender-supplied fluid cell was used for atomic force measurements. A procedure similar to that described in [31] was followed for sample preparation and measurements.

A prepared substrate was mounted on the piezoelectric transition stage. A clay probe was mounted in the fluid cell. To position a clay probe just over a clay particle glued onto the substrate surface, an optical viewing and positioning system (Digital Instruments) was

---

[§§] All surface force measurements discussed in this study were performed by Dr. Sili Ren (sren@ualberta.ca).

32

used. In our experiment, a prepared solution was slowly injected into the fluid cell with great care to avoid the trapping of air bubbles. The system was allowed to incubate for 1 h at room temperature before the first approach of the probe to the substrate. In the force measurements, the piezoelectric transition stage brought the substrate with clay particles to approach or retract from the probe particle in the vertical direction.

The forces between the probe and a particle on the substrate surface were determined from the deflection of the cantilever using Hooke's law. Each force plot represents a complete extension/retraction cycle of the piezo. When the substrate approached the probe, the long-range interaction between the two particles was measured, whereas the adhesion (or pull-off) force between them was obtained during the retraction process after contact was made. Because the clay particles were irregular, to obtain representative results, each experiment was performed with three particle–particle probe pairs and repeated twice for each pair. For each test condition, hundreds of force profiles were recorded. For quantitative comparison, the measured long-ranged interaction force (F) and adhesion force were normalized by the probe radius (R_p).

33
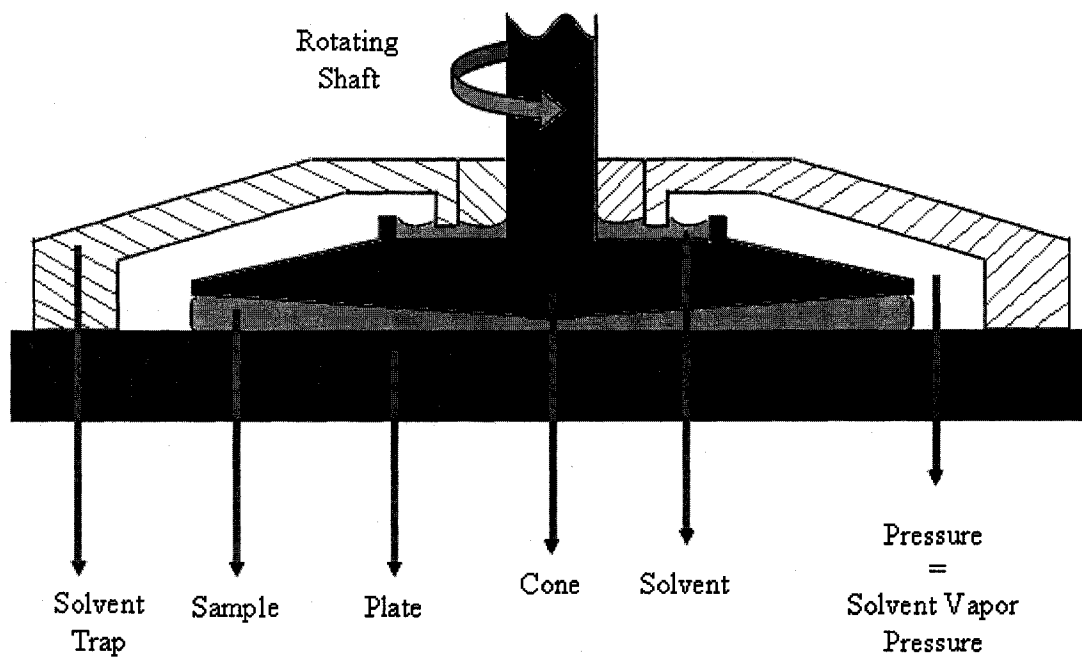
Figure 2.1 – Cone-and-plate geometry with the solvent trap positioned in place.
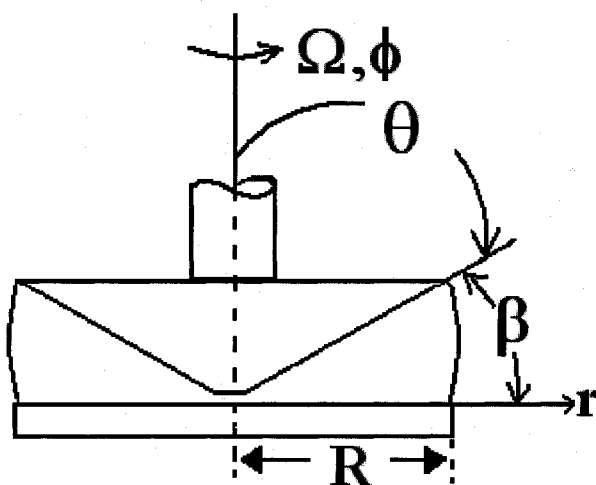
Figure 2.2 – Cone-and-plate geometry in spherical coordinates (ϕ, θ, r).

34
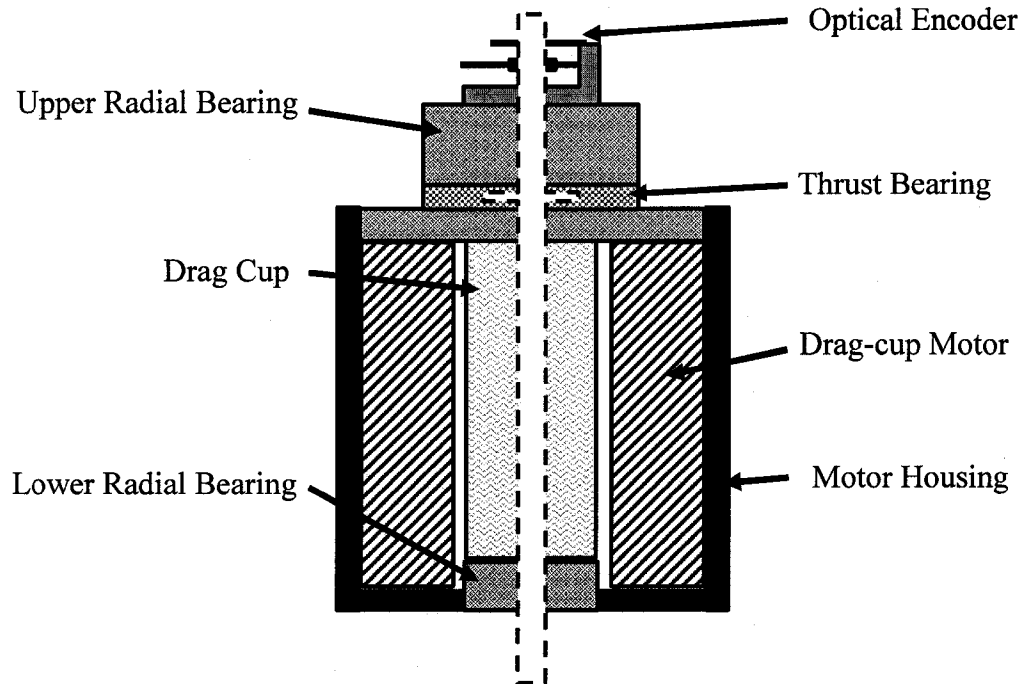
Figure 2.3 – Drive unit of the Rheometer.

35
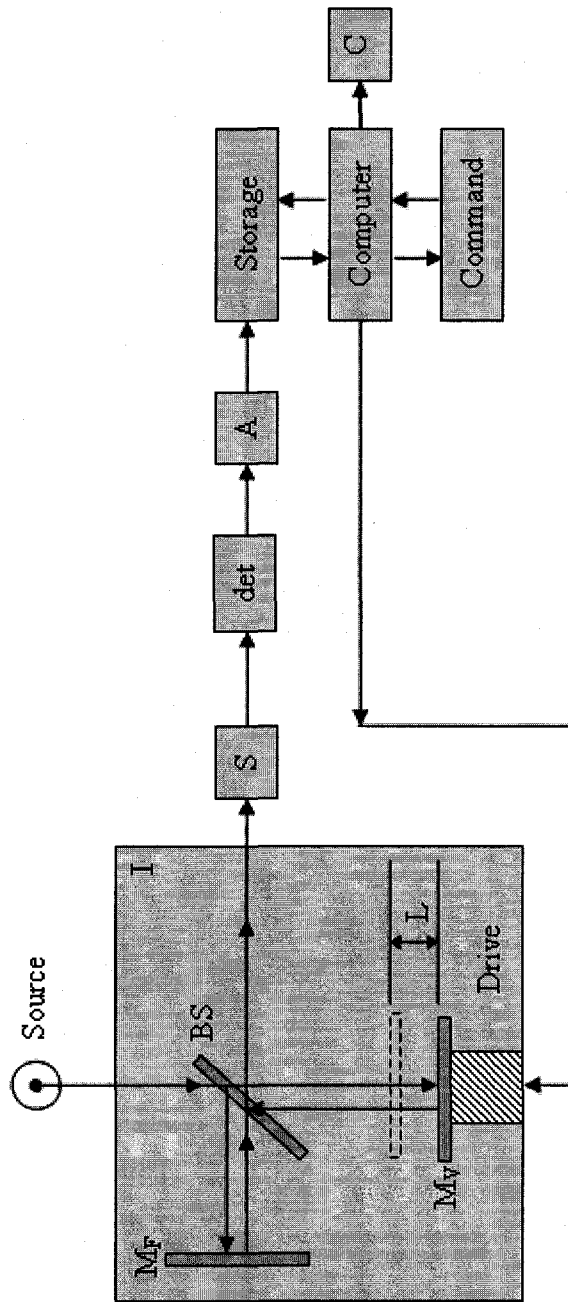
Figure 2.4 - Block Diagram of a Fourier transform system.
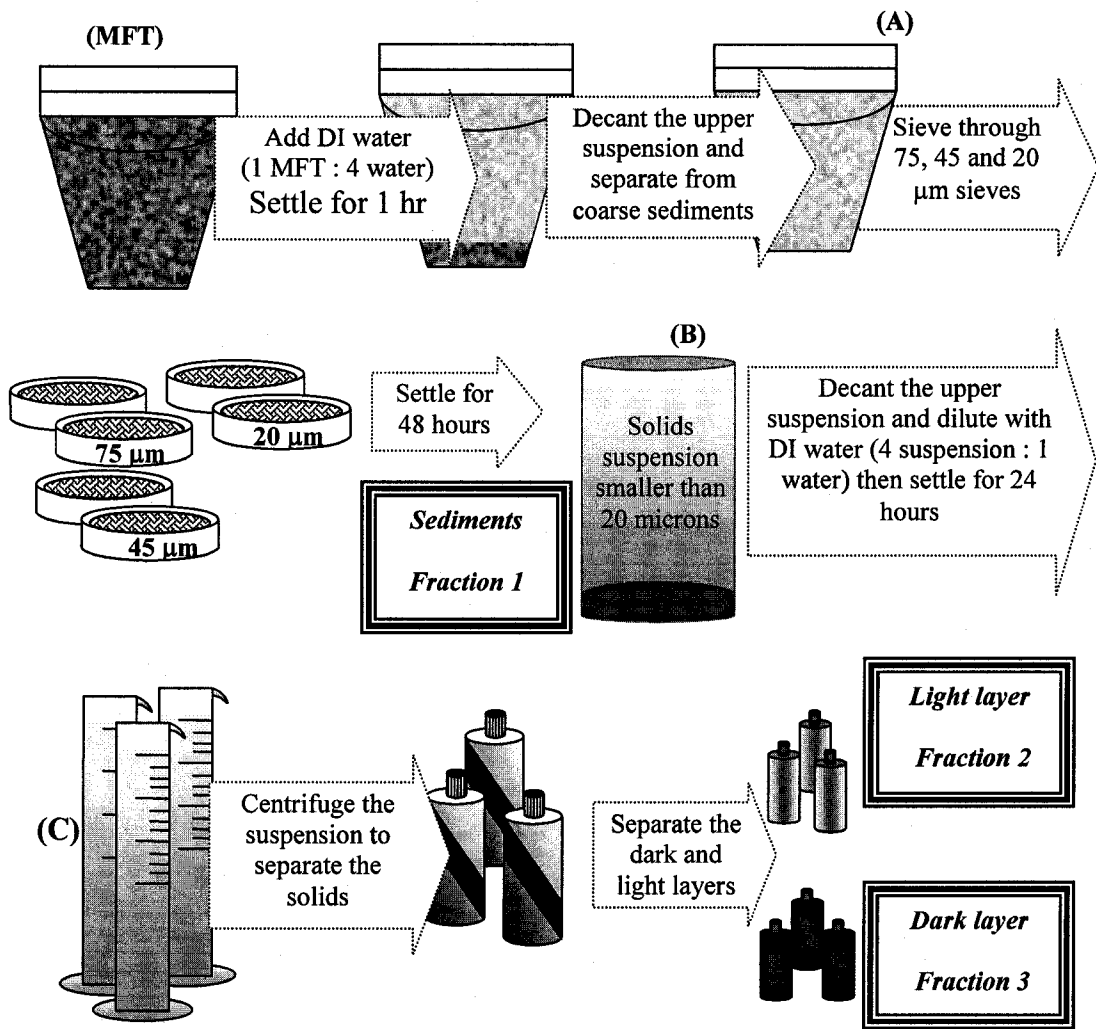
Figure 2.5 – Fractionation of ultra-fine solids from mature fine tails (MFT).

37
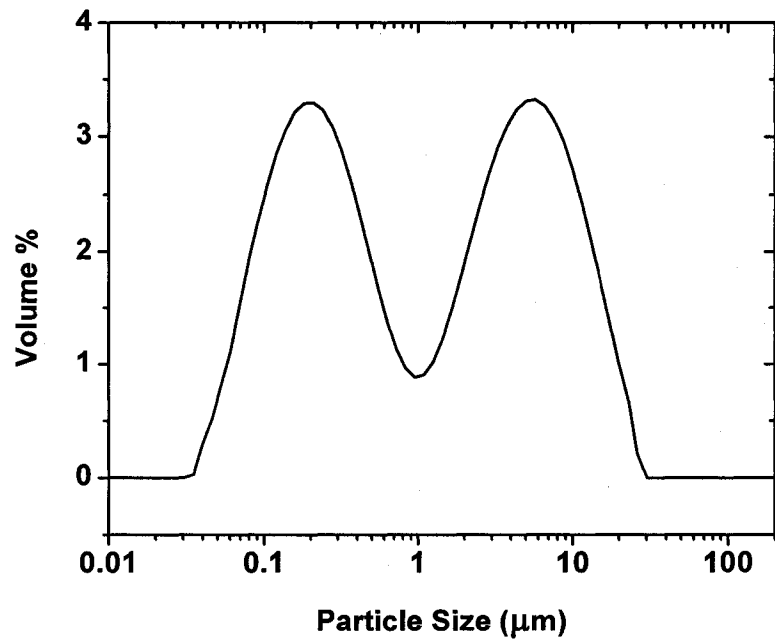
Figure 2.6 – Particle size distribution of the sieved suspension.
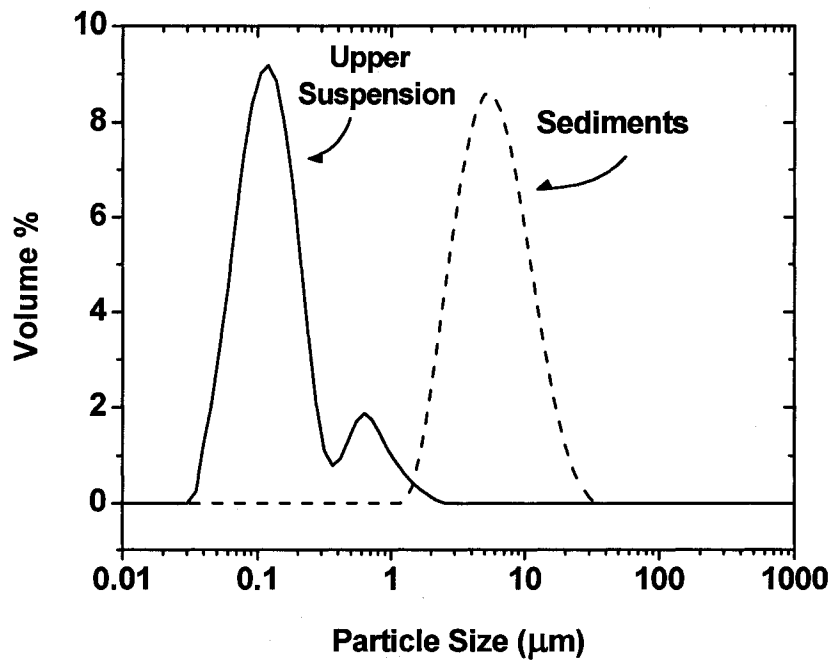
Figure 2.7 – Particle size distribution of the sediments and upper suspension in B.

38
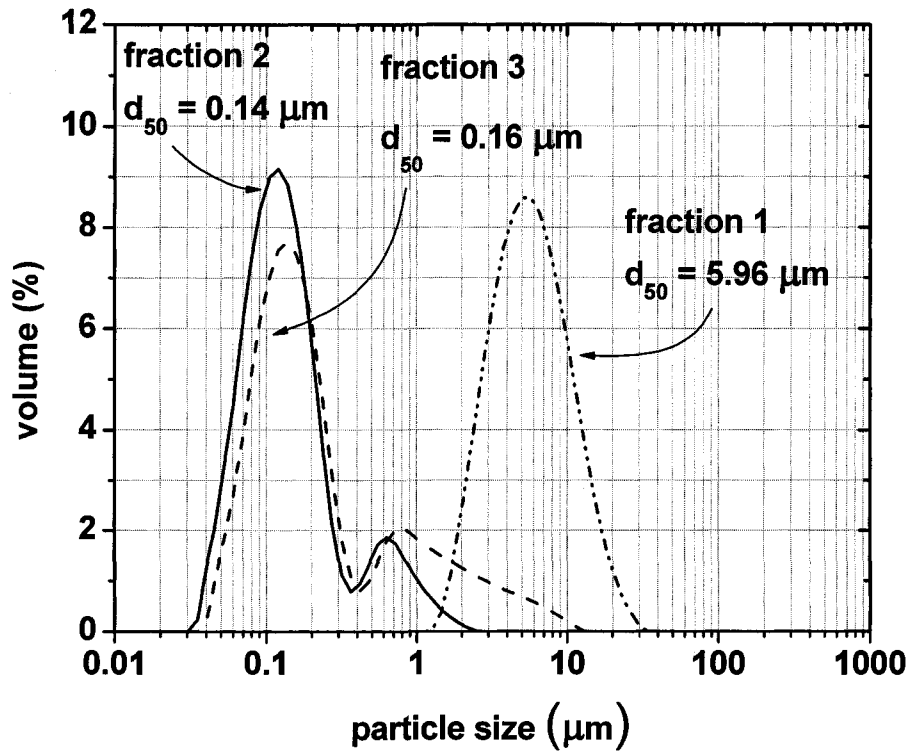
Figure 2.8 – Particle size distribution of fractions 1, 2 and 3.
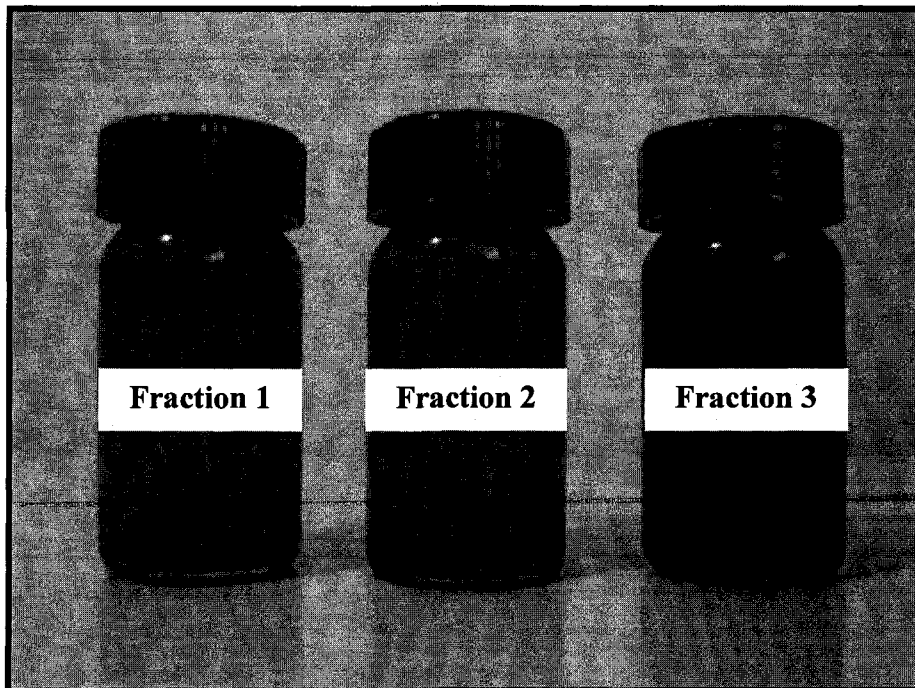
Figure 2.9 – Fractions 1 to 3.

39

Table 2.1 – Sequence of rheological experiments.

Test No.	Test Type	Parameters	Results
1	Conditioning	$\dot{\gamma} = 1500s^{-1}$ $t = 10s$	
2	Equilibration	$t = 180s$	
3	Flow, Steady State	$\dot{\gamma} = 2 \rightarrow 2000s^{-1}$	Stress(τ), yield stress (τ_y), relative viscosity $\mu(\dot{\gamma})$
4	Conditioning	$\dot{\gamma} = 1500s^{-1}$ $t = 10s$	
5	Equilibration	$t = 180s$	
6	Oscillatory, Strain Sweep	$\dot{\gamma} = 1 \times 10^{-3} \rightarrow 0.1s^{-1}$ (angular frequency = 6.283 rad/s)	storage modulus (G'), loss modulus (G''), phase angle (δ), oscillatory stress
7	Conditioning	$\dot{\gamma} = 1500s^{-1}$ $t = 10s$	
8	Equilibration	$t = 180s$	
9	Oscillatory, frequency sweep	Oscillatory stress = constant (measured in test 6) Angular frequency = $1 \rightarrow 100 rad/s$	G', G''

3.   Rheology of Oil Sands Ultra-Fines

For the purpose of this study, rheological measurements were utilized to determine the effect of ultra-fine solids on the flow properties of oil sands slurries. Because gelled middlings are not readily available, mature fine tails (MFT) were chosen as the source of solid particles. Originating from gravity separation vessel middlings, MFT is conveniently accessible. In one occasion where a small amount of gelled middlings was provided, comparisons were made between the mineral composition of MFT and gelled middlings.

Mineralogy of MFT and gelled middlings was determined by X-ray diffraction analysis[***]. X-ray diffraction patterns were collected with a Rigaku D Max B rotating anode (CuK$_\alpha$ and CoK$_\alpha$). Calcium-saturated and glycolated slides of solids were prepared for mixed layer clay identification and quantification as described in reference [32]. The X-ray diffraction patterns of calcium saturated and glycolated slides of solids from MFT and gelled middlings are shown in Figure 3.1a. Figures 3.1b and 3.1c respectively show the diffraction patterns of calcium saturated oriented slides of gelled middlings and MFT at 54% relative humidity in addition to an ethylene glycol environment.

The presence of illite-smectite mixed layers was speculated as a result of the broadening of the peak around 1 nm in the X-ray diffraction pattern, when the clays were Ca-saturated and exposed to 54% relative humidity. At 54% relative humidity, a swelling pure smectite layer having 2 water molecules causes an increase in d-spacing from 1 to 1.5 nm. With ethylene glycol, each molecule is about 0.35 nm, leading to an expansion from 1 to 1.7 nm. When smectite occurs as a mixed layer with illite, as commonly observed in oil sands, there will be a 0.2 nm shift, going from 54% relative humidity to ethylene glycol vapour. However, the actual position of the 1 nm peak depends on the extent of mixed layering. Usually, discrete illite and kaolinite do not respond to ethylene glycol solvation. Upon treatment with organics such as ethylene glycol and glycerol, the

---

[***] Analysis of the XRD patterns were performed by Dr. Oladipo Omotoso (oomotos@NRCan.gc.ca).

41

d-spacings became more precise and the illite peak became more well-defined – an event that is typical of a clay with swelling properties. The presence of randomly interstratified kaolinite-smectite is evident by the asymmetry of low angle peak of the kaolinite at the 0.72 nm peak upon hydration or glycolation.

Quantification (Figure 3.2) was carried out through NEWMOD modeling of the diffraction patterns [33]. The surface area calculation (Table 3.1) was based on the double Voigt method [34] implemented in TOPAS [35]. The quantification procedure as applied to oil sands has been reported previously [32, 36-37]. The diffraction patterns of MFT and gelled middlings show similar peaks. Both samples contain discrete kaolinite and illite in addition to illite-smectite and kaolinite-smectite mixed layers. Figure 3.2 and Table 3.1 show that the type and the amount of minerals in MFT are similar to that found in gelled middlings. Therefore, the results obtained using MFT ultra-fines can be extended to explain the behaviour of oil sands middlings as well.

3.1.   Water Chemistry

Surface properties of clay minerals are strong functions of the chemistry of their suspending medium. As such, rheological behaviour of clay dispersions is strongly affected by the ionic concentration of their suspending medium. Depending on the ionic strength of the solution, clay suspensions can show a diversity of flow behaviours, ranging from Newtonian to a completely non- Newtonian elastic behaviour [38-42].

With focus on oil sands suspensions, initial sets of experiments were carried out on fractions 1 to 3, all of which were dispersed in the original suspending water of mature fine tails (referred to as MFT supernatant in this work). Ionic concentrations of the medium in which these samples were dispersed were compared to that of MFT supernatant (Figure 3.3). Based on the results shown in Figure 3.3, ion concentrations of the suspensions had little deviation from the original chemistry of MFT supernatant. This method therefore preserved the solution chemistry and surface properties of the solids. With little to no deviations from the original conditions of the ultra-fine solids, the results

obtained in this section would directly represent the behaviour of oil sands ultra-fines in the separation process.

3.2. Fraction 1 (d_{50} = 5.96 μm)

Figure 3.4 shows the relative dynamic viscosities[†††] (μ_r) of four suspensions of fraction 1 at 10, 20, 30 and 40 wt% solids concentrations. The results show an increase in suspension viscosity with solid concentration. All suspensions showed a non-Newtonian shear-thinning behaviour where viscosity decreased with shear rate. Higher viscosities at low shear rates indicated the presence of a networked structure in the solid suspensions. As the shear rate increased, the structures were disturbed and broken. Such disturbances in the network structure appeared as decreased viscosity in the results of simple shear flow tests.

As solid concentration was decreased, the flow behaviour of the suspensions also showed a decrease in the non-Newtonian characteristic of the suspensions. This behaviour could be explained based on the effect of particle concentration on the inter-particle forces. At high solid concentrations, the distances between the particles are smaller. Therefore, the particles are in the range where inter-particle forces are active. However, once the concentration is lowered, inter-particle forces are not strong enough to impose a preferred structure in the suspensions. With no structures formed, there will be little change in the viscosity of the suspension; effects of shear and shear-thinning of the suspension will also not be as severe.

For solid-liquid dispersions, yield stress calculation is used as a tool to measure the onset point of elastic properties. When the stress applied to such a suspension is below its yield stress, the material response to shear will be solid-like (constant stress). The magnitude of the yield stress can, to some level, reflect the structures in a suspension. For the

---

[†††] Defined as the ratio of the apparent viscosity of the solids suspension to the viscosity of water at the temperature of the measurements (25°C)

43

suspensions of interest to this work, the Casson model (Equation 3.1) was used to calculate yield stress.

$$\tau^{1/2} = \tau_y^{1/2} + \mu_c^{1/2}\dot{\gamma}^{1/2}$$

(3.1)

In equation 3.1, μ_c is Casson viscosity. Yield stress values can be calculated through the Casson model provided that the square roots of shear stress and shear rate correlate well through a straight line. Figure 3.5 shows that for suspensions of fraction 1 discussed above, a linear correlation could well represent the relationship between square roots of shear stress and shear rate. Thus, the Casson model was an appropriate model to calculate yield stresses of these suspensions.

To calculate yield stress using the above equation, variations of shear stress with shear rate as measured by simple shear flow tests, were substituted in equation 3.1. Figure 3.6 shows the yield stress of fraction 1 with respect to solids concentration. Based on the results, yield stress increased with solids concentration and the highest yield stress was reached at 40 wt%. High yield stress means that a higher stress is required for flow to occur. This initial stress would be required to displace the particles from their preferred positions. High yield stress values would therefore indicate that the particles have a high tendency to maintain their positions. Therefore, an elevated yield stress with increasing solids concentration directly translates to the presence of stronger structures at higher solids concentration. This is in agreement with what was observed in the relative viscosity (Figure 3.4) plots of these suspensions.

Depending on the strength of the suspension structures, they can behave as solid, liquid or viscoelastic gel. To identify the state of gelation in suspensions of fraction 1 solids, oscillatory frequency sweeps were performed. Frequency sweep tests should be carried out in the linear viscoelastic region of the samples where sustained shearing does not disturb the structures in the suspension. For all samples, linear viscoelastic region was determined through oscillatory strain sweep tests. Figure 3.7 shows the results of strain sweep on a 30 wt% suspension of fraction 1 solids. Based on this figure, the linear

44

viscoelastic region falls between 0.0007 and 0.002 Pa oscillatory shear. The linear region for all other suspensions was determined in an identical manner (See Appendix A).

Figure 3.8 shows the results of frequency sweep tests on suspensions of fraction 1. For a 20 wt% suspension of fraction 1, the curves of the two viscoelastic moduli, G' and G'', coincided at about 20 rad/s angular frequency, after which G' became higher than G''. However, for most of the frequencies investigated, G'' was higher than G', indicating more prominent liquid-like behaviour of the suspension. When particle concentration was increased to 30 wt%, G' became higher than G'' over a significant range of the frequencies studied. Yet the two curves cross when angular frequency reached about 90 rad/s. This behaviour showed a slight structure formed in the suspension at 30 wt% solids concentration. At 40 wt% solids, the G' and G" curves did not intersect over the entire range of frequencies studied. The solid-like properties of the suspension were higher than its liquid-like properties, which indicated the formation of a strong solid-like structure or a viscoelastic gel.

Once again, the results confirmed an increase in suspension structure with increasing solid concentration. Higher solid concentration in the suspension corresponded to stronger elastic properties. For similar suspensions, such behaviour was reported in the literature. In references [38] and [39], the authors studied suspensions of sodium-montmorillonite and laponite clays, and reported an increase in elastic properties of the suspension as particle concentration was increased. This behaviour was attributed to the electrostatic interaction of the charged clay particles in the suspension. For ultra-fine solids separated from oil sands, reference [19] also showed increased viscosity and elastic properties with increasing solids concentration.

3.3. Fraction 2 ($d_{50} = 0.14 \ \mu m$)

Figure 3.9 shows the relative viscosity of fraction 2 at different solids concentrations. All suspensions show non-Newtonian shear-thinning behaviour similar to what was observed for suspensions of fraction 1. At low concentrations, structure formation in the

45

suspensions yielded higher viscosities, while shearing the suspensions broke the structures and led to lowered viscosity. Increasing solid concentration increased the viscosity of fraction 2 suspensions as well.

While the trend of the flow curves for suspensions of fraction 2 is similar to those observed for fraction 1, it is interesting to note that the scale of the results in Figures 3.4 and 3.9 differ significantly. At given solids concentration, the viscosity of fraction 2 was higher than its corresponding value for fraction 1 over the range of shear rates studied. Looking at the low shear rate viscosities in Figure 3.10 for fractions 1 and 2 at 30 wt% solids concentration, it shows that the results obtained for the two suspensions differ by two orders of magnitude. This difference in viscosities decreased to one order of magnitude at lower solids concentration. Clearly, particles in fraction 2 formed a more stable structure in their suspensions when compared to fraction 1.

Yield stress for fraction 2 was calculated following the same method applied to fraction 1. First, the linear correlation between square roots of shear stress and shear rate was to be verified. Figure 3.11 shows such linear correlation was present between the two variables (τ_y and $\dot{\gamma}$). Therefore, the Casson model was also suitable for yield stress calculation of fraction 2. Figure 3.12 shows the yield stresses of fraction 2 at different solids concentrations. Once again, the observed trend was similar to that of fraction 1. Increasing solids concentration increased suspension yield stress. This finding pointed to the fact that, with more solids present in the system, the structures formed within the suspensions of fraction 2 were stronger. Comparing the values obtained for yield stresses of fraction 1 and 2, however, indicated the presence of stronger structures in suspensions of fraction 2 as the latter showed to have higher yield stress values.

Figure 3.13 shows the results of frequency sweep tests on fraction 2. Prior to this test, strain sweeps were performed on the samples to determine their linear viscoelastic region (Appendix A). Figure 3.13 shows that for a 10 wt% suspension of fraction 2, at frequencies lower than about 30 rad/s, the value of the elastic modulus G' was higher than the viscous modulus G''. At higher frequencies, however, the elastic modulus of the

46

10 wt% sample became lower than its viscous modulus. This trend indicated a weak structure in the sample. The structure formation in the suspension became more significant when the solids concentration was increased to 20 wt%. Figure 3.13 shows that at 20 wt% total solids, G' is higher than G'' over the entire range of frequencies studied. Increasing solids content in the suspension of fraction 2 did not alter this trend. With G' higher than G'', the suspension of fraction 2 had formed a viscoelastic gel at 30 wt% solid as well.

Once again, in comparison with fraction 1, a similar trend of gel formation was observed for fraction 2. Increasing solids concentration increased the elastic properties of suspensions of fraction 2 and led to gel formation. However, comparing fractions 1 and 2 in terms of the stability of the solid-like structure showed that fraction 2 had a stronger tendency to form a gel at lower particle concentrations. The different scales of the viscoelastic moduli in the frequency sweep diagrams for fractions 1 and 2 verified the stronger solid-like characteristics of fraction 2 at lower solids contents.

Based on the results of flow and oscillatory tests on fractions 1 and 2, fraction 2 with smaller particle sizes formed stronger network structures and had a higher tendency to form a gel. Recall that the mean particle diameter of the solids in fraction 2 was smaller than that of fraction 1. In reference [43], the authors studied the effect of particle size on the flow properties of coagulated colloidal suspensions. They showed that as particle size was decreased, a higher volume fraction of the sample was occupied by flocs rather than single particles. The smaller particles formed more open flocs, leading to high yield stress. In a study on clay suspensions typical of the ceramic industry in reference [40], it was reported more prominent elastic properties for suspensions formed of smaller particles. This behaviour could be attributed to the higher surface-to-volume ratio of the smaller solids. The effect of surface forces is more significant where there is more surface area available for particle interactions.

47

3.3.1. Fractions 1 and 2 – Bimodal System

Figure 3.14 shows the rheological behaviour of a mixture of fractions 1 and 2. While keeping the total solids content constant at 10 wt%, the percentage of fraction 2 was increased. The suspension viscosity was monitored for simple shear tests following the same procedure as for single fraction suspensions. While the suspensions maintained non-Newtonian shear-thinning behaviour, a maximum viscosity was achieved when the suspension only contained solids of fraction 2.

Figure 3.15 shows the relative viscosity of the bimodal suspensions at a given shear rate on a semi-log system of axes. The results in Figure 3.15 show that although the total concentration was kept at 10 wt%, adding particles of fraction 2 to suspensions of fraction 1 increased its viscosity. Yield stress values of these suspensions, as calculated by the Casson model followed the same trend (Figure 3.16). Increasing the content of smaller particles in the suspension, while maintaining total solids content, increased suspension viscosity.

This monotonic increase in viscosity and yield stress with the content of fraction 2 suggests that the system deviated from an ideal hard sphere case since, as reported in reference [44], one would anticipate a minimum in the viscosity for bimodal distribution of hard spheres.

3.4.   Fraction 3 (d_{50} = 0.16 μm)

As was the case for fractions 1 and 2, flow and oscillatory tests were performed on suspensions of fraction 3 at different solids concentrations. Figure 3.17 shows the results of flow tests for fraction 3. This fraction also had a non-Newtonian shear thinning behaviour in its suspensions. The relative viscosity significantly dropped as the rate of shearing on the sample was increased. This behaviour was a sign of network formation within the suspensions similar to that in the previous samples of fractions 1 and 2. Figure 3.18 shows the results of simple shear flow tests on fractions 2 and 3 at a 1:1 mass ratio in a suspension of 20wt% total solids concentration. The combination of fractions 2 and 3

48

showed a higher viscosity than fraction 2 alone. Figure 3.18 thus shows that at a given total concentration, the more fraction 3 solids present in the suspension, the higher the viscosity.

Yield stressed for suspensions of fraction 3 were calculated using the Casson model. Figure 3.19 shows the linear relation between square roots of shear stress and shear rate, proving the suitability of the Casson model for yield stress calculations. Figure 3.20 shows the calculated yield stress values. As expected, the yield stress increased with particle concentration, implying the presence of stronger structures at higher particle contents.

Figure 3.21 shows the storage and loss moduli of suspensions of fraction 3 over two decades of angular frequency. Based on the results, with the storage or elastic modulus higher than the viscous modulus, all three suspensions tested had formed a gel. Even at 5 wt% solids, the difference between G' and G'' is about one order of magnitude. For fraction 3, the gel strength that was achieved at 40 wt% of fraction 1 and 20 wt% of fraction 2 was reached at a much lower concentration of 5 wt%.

Although suspensions of fraction 3 followed a trend similar to that of fractions 1 and 2, the viscosities, yield stresses and the dynamic elastic moduli of this fraction were considerably higher than what was observed in the previous cases. Noting the similar particle size distributions of fractions 2 and 3, according to light scattering measurements (using Mastersizer 2000), this difference was not expected. Therefore, the stronger elastic behaviour of fraction 3 cannot be explained based on particle size measurements. Further characterisation measurements were performed on the solids to study the nature of the interactions between the particles and clarify the rheological behaviour observed above. Chapter 4 gives the details of the characterisation experiments.

3.5. Mapping Gelation Status of MFT Ultra-Fines

Figure 3.22 summarizes the values of yield stress calculated for all three fractions. Incorporating the results of the frequency sweep tests discussed earlier into this figure,

the status of gelation was mapped for all suspensions of fractions 1 to 3. At 20 wt%, fraction 2 started to show a gelled structure. Similar structured behaviour was not achieved for fraction 1 until 40 wt% solids concentration. Based on these observations, a yield stress of about 0.1 Pa in Figure 3.22 was chosen to mark the onset of gelation as it corresponds to gel forming concentrations. Accordingly, all three suspensions of fraction 3 fell above the 0.1 Pa yield stress line. With a similar analysis, the other two regimes were designated as weak and no gel.

50
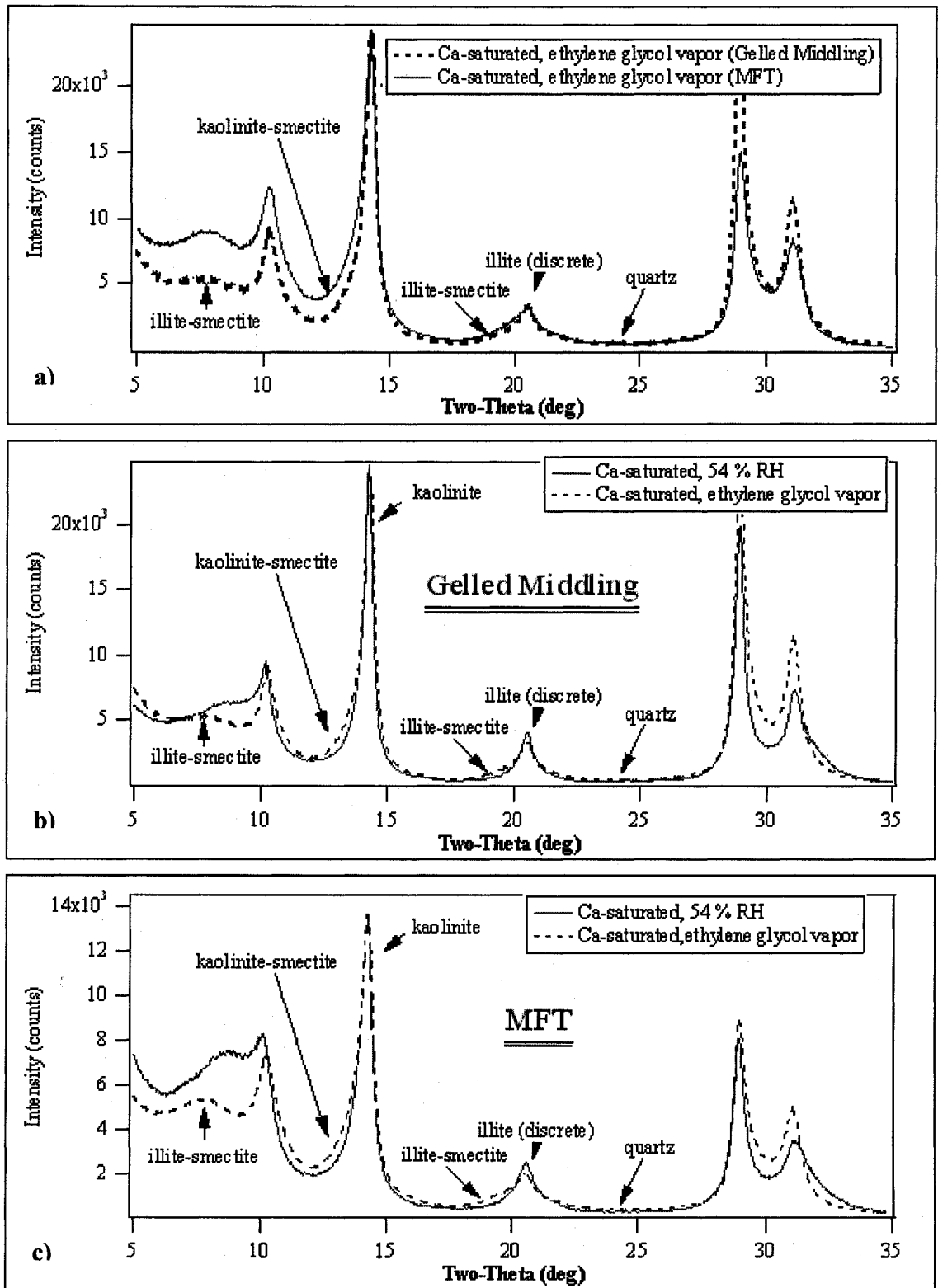
Figure 3.1 - Diffraction patterns of gelled middlings and MFT.
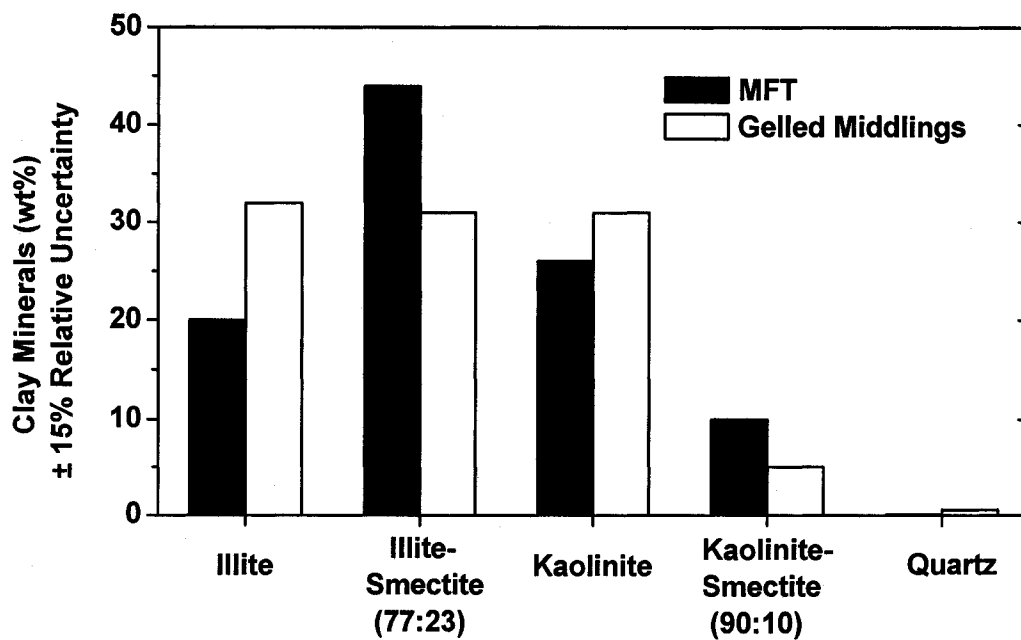
Figure 3.2 - Mineral composition by XRD.
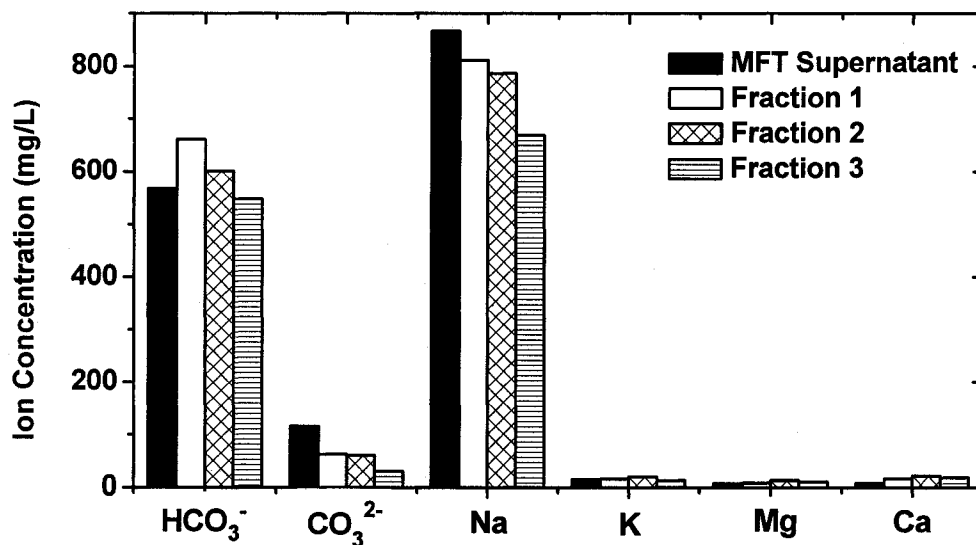
Figure 3.3 - Ion concentration in the suspending medium of MFT and the three ultra-fine fractions separated from it.

52
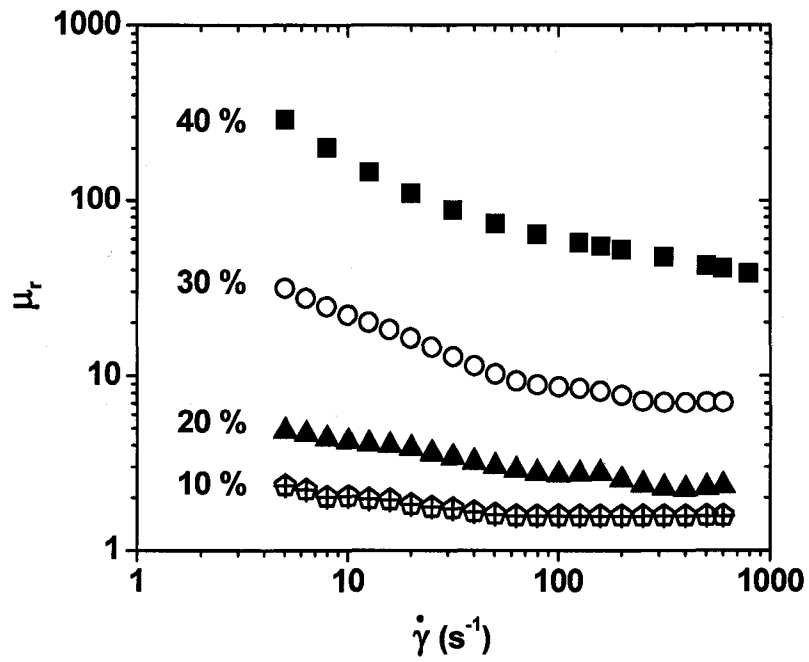
Figure 3.4 – Relative viscosity of fraction 1 at different solids concentrations.
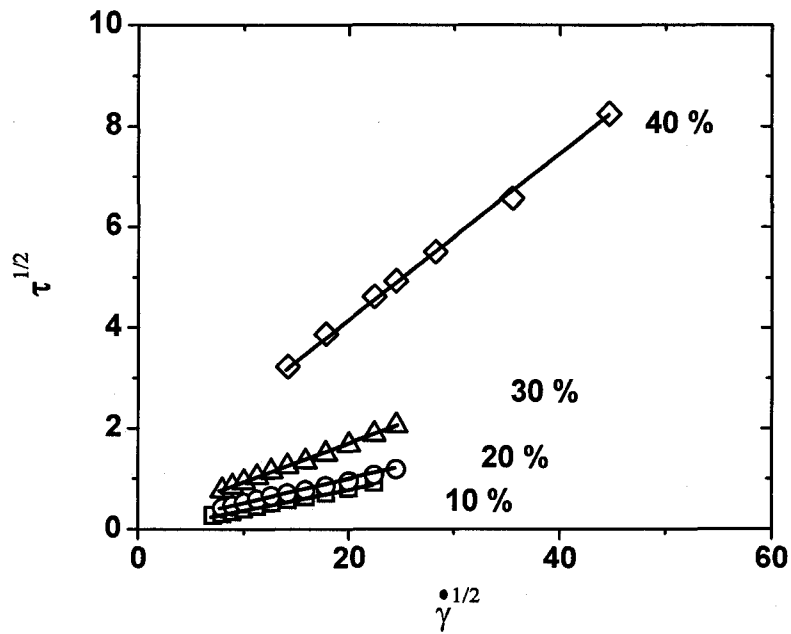
Figure 3.5 – Verifying the application of the Casson model for yield stress calculations of fraction 1.

53
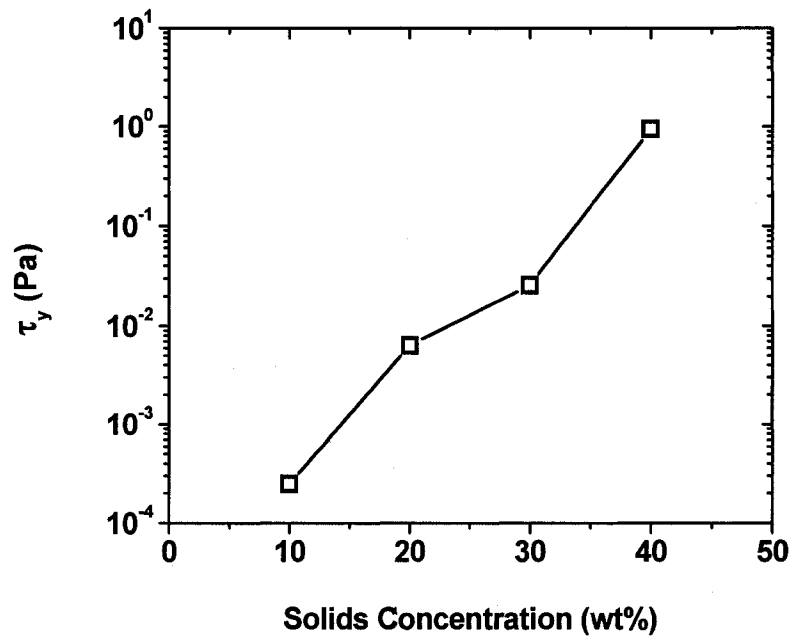
Figure 3.6 - Yield stress of fraction 1 as calculated through the Casson model.
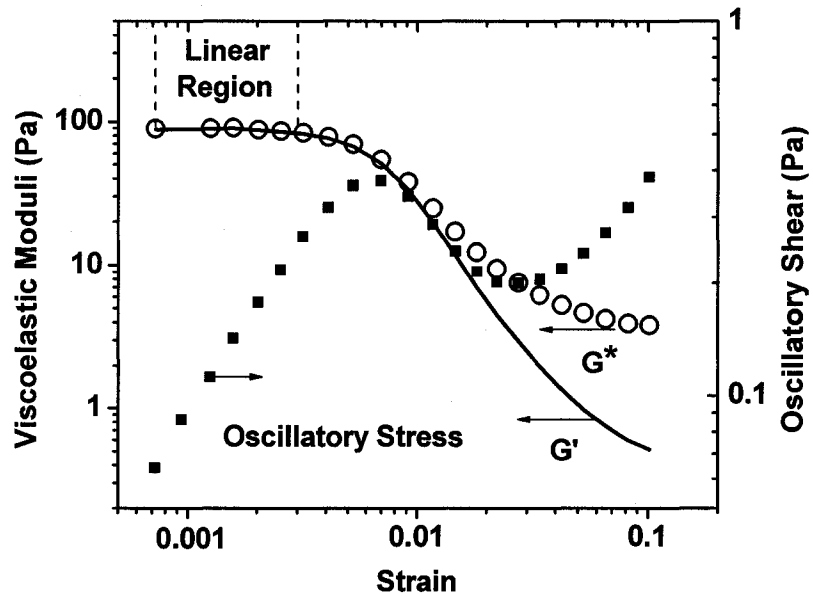
Figure 3.7 – Strain sweep on a 30 wt % suspension of fraction 1 determining the linear viscoelastic region of the suspension.

54
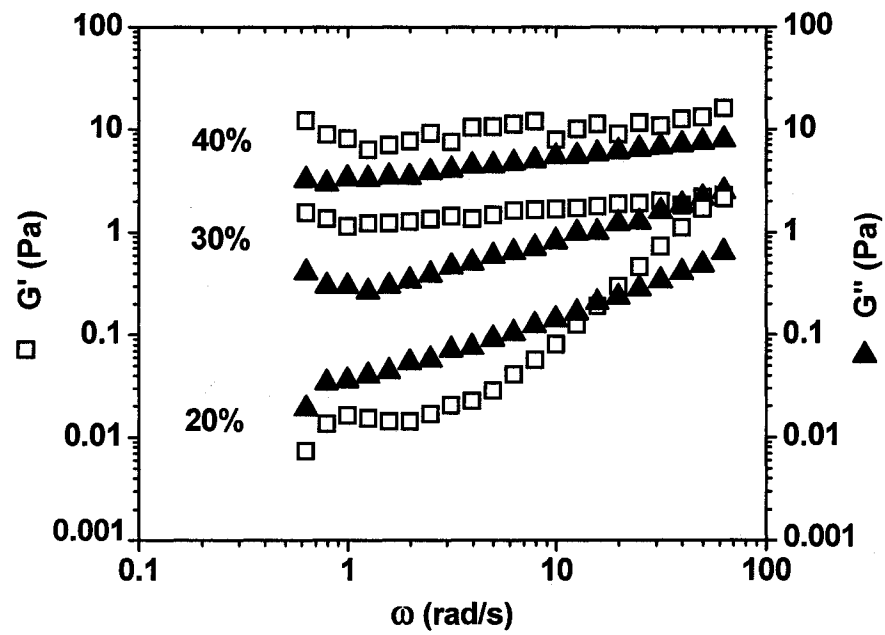
Figure 3.8 – Frequency sweep on suspensions of fraction 1.
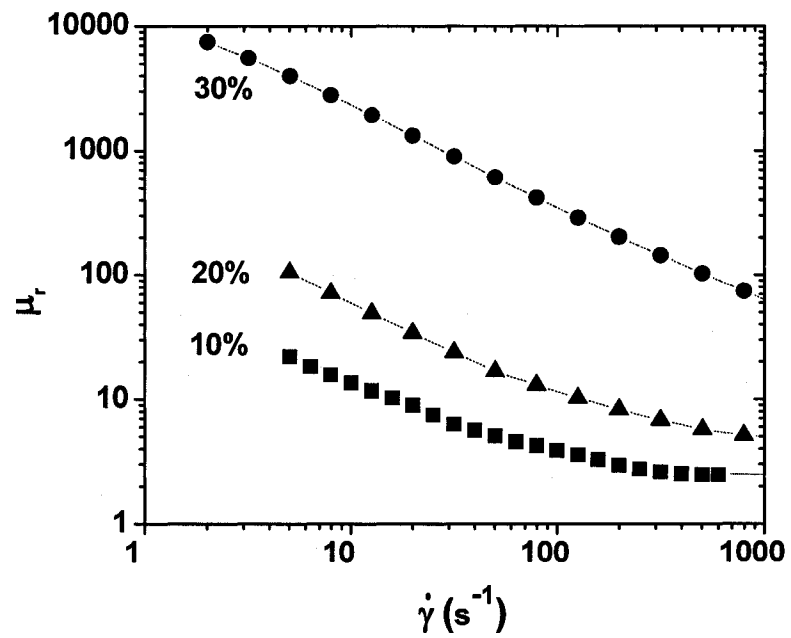
Figure 3.9 – Relative viscosity of fraction 2.

55
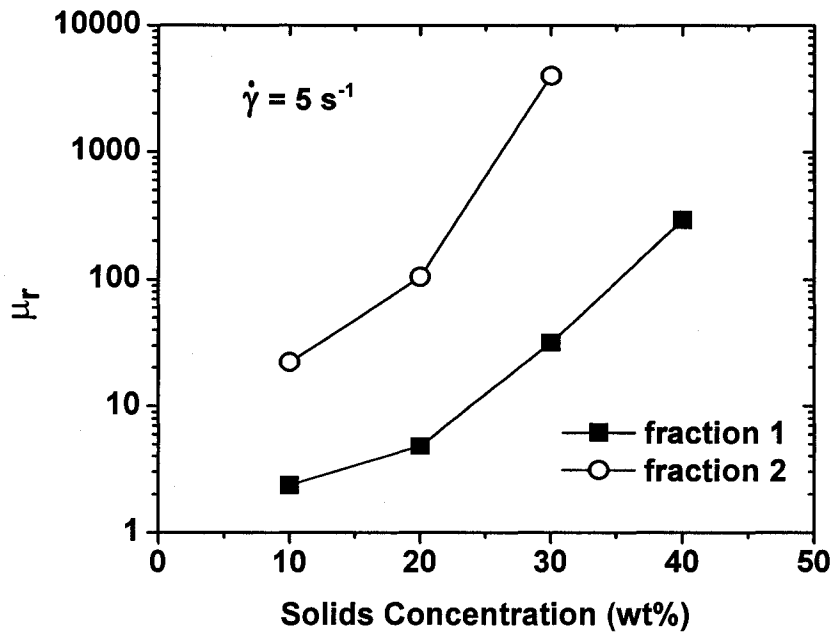
Figure 3.10 – Relative viscosities of fractions 1 and 2 with respect to solids concentration.
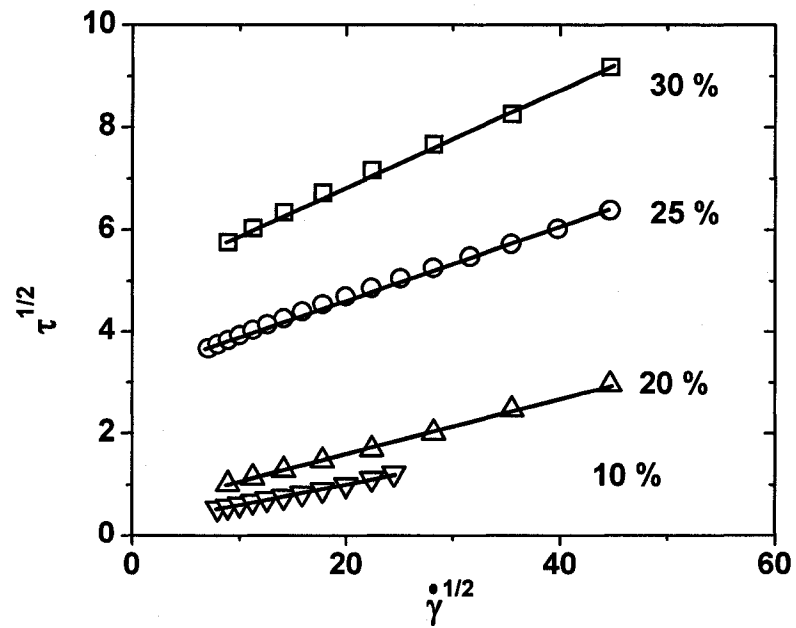
Figure 3.11 - Verifying the application of the Casson model for yield stress calculations of fraction 2.

56
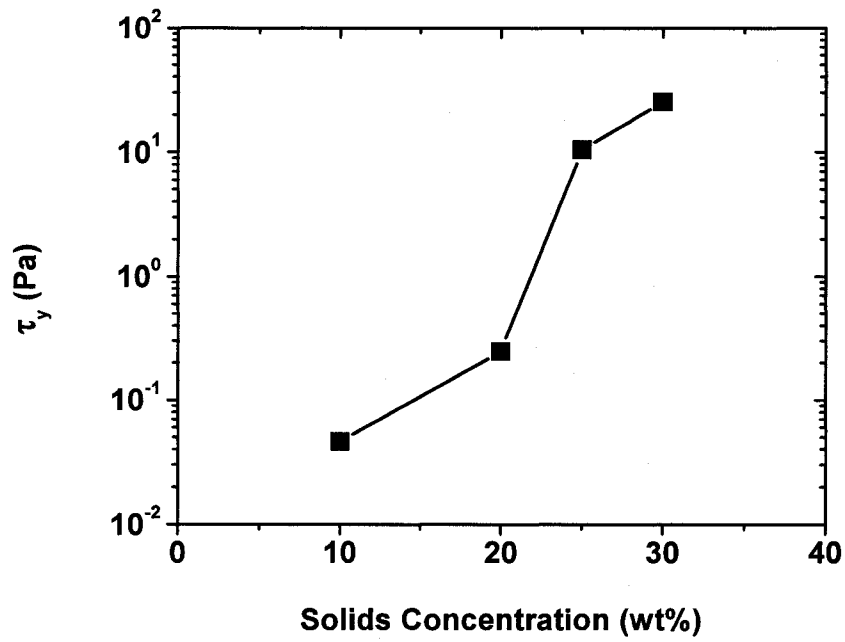
Figure 3.12 - Yield stress of fraction 2 as calculated through the Casson model.
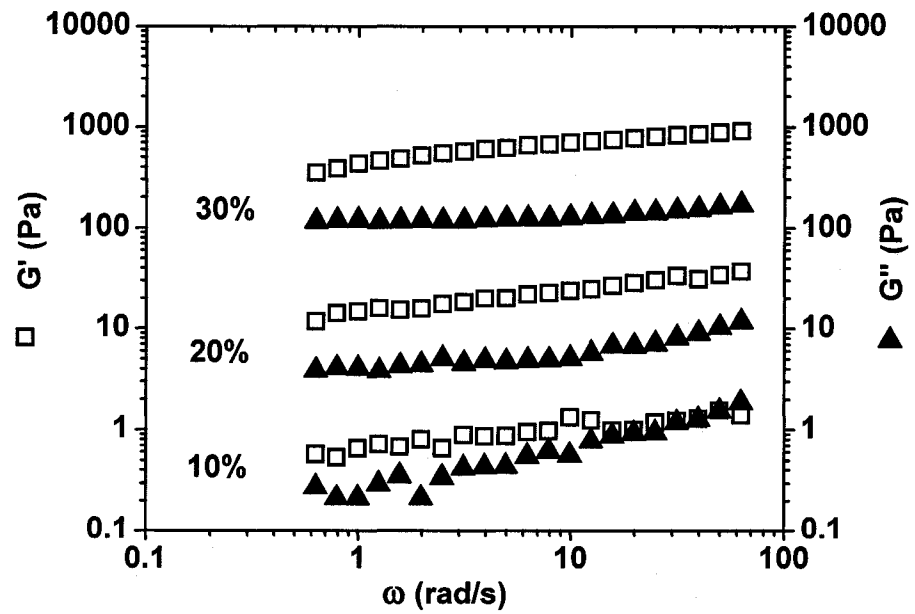
Figure 3.13 – Frequency sweep on suspensions of fraction 2.

57
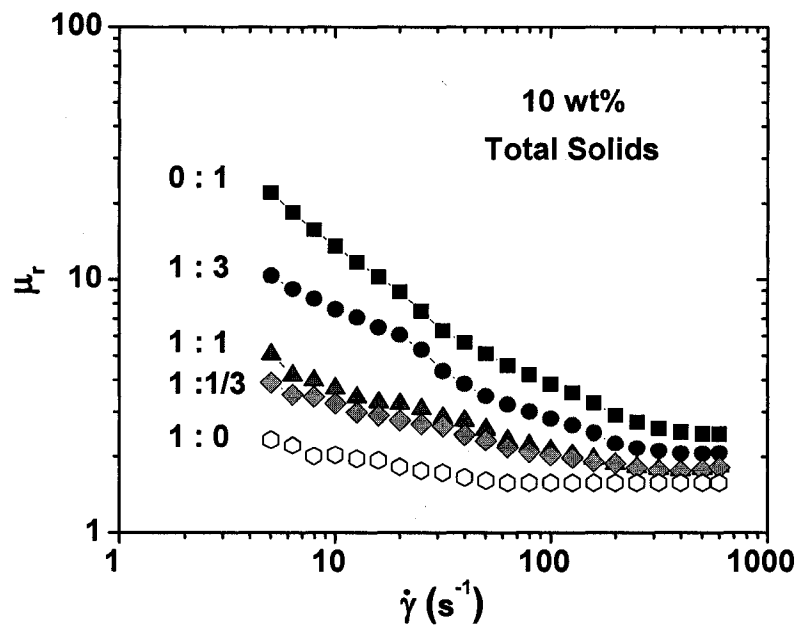
Figure 3.14 - Relative viscosity at different ratios (x : x) of fraction 1 to fraction 2.
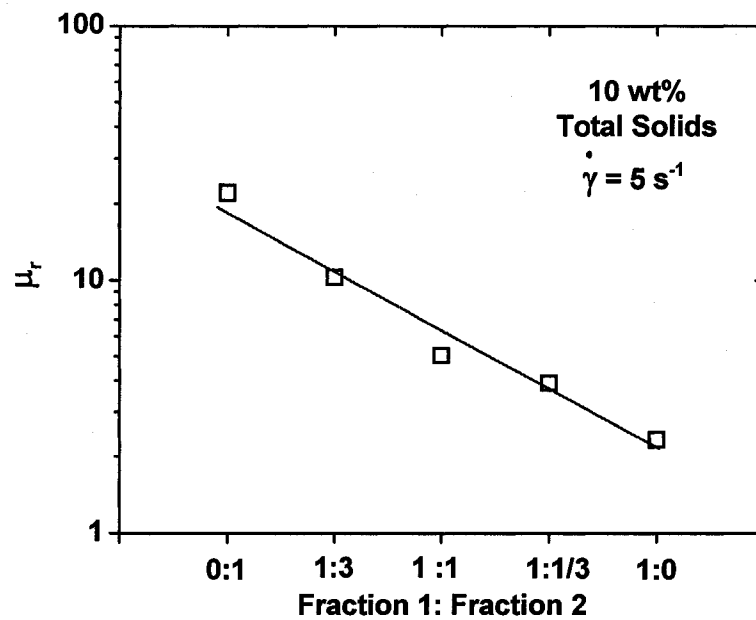
Figure 3.15 – Relative viscosity of a bimodal system of fractions 1 and 2 with respect to fraction 1 to fraction 2 ratio at constant total solids concentration and at $\dot{\gamma} = 5$ s^{-1}.

58
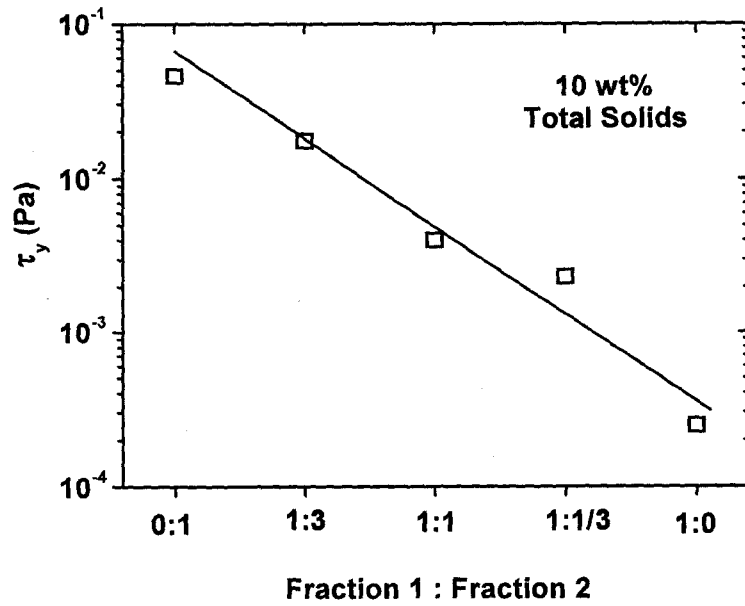
Figure 3.16 – Yield stress of a bimodal system of fractions 1 and 2 with respect to fraction 1 to fraction 2 ratio at a given shear rate.
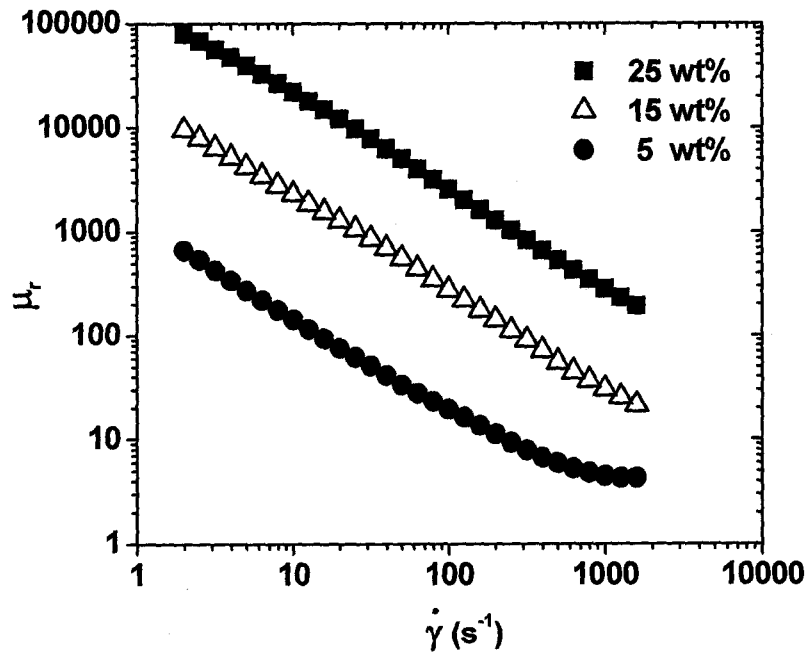
Figure 3.17 - Relative viscosity of fraction 3 at different solids concentrations.
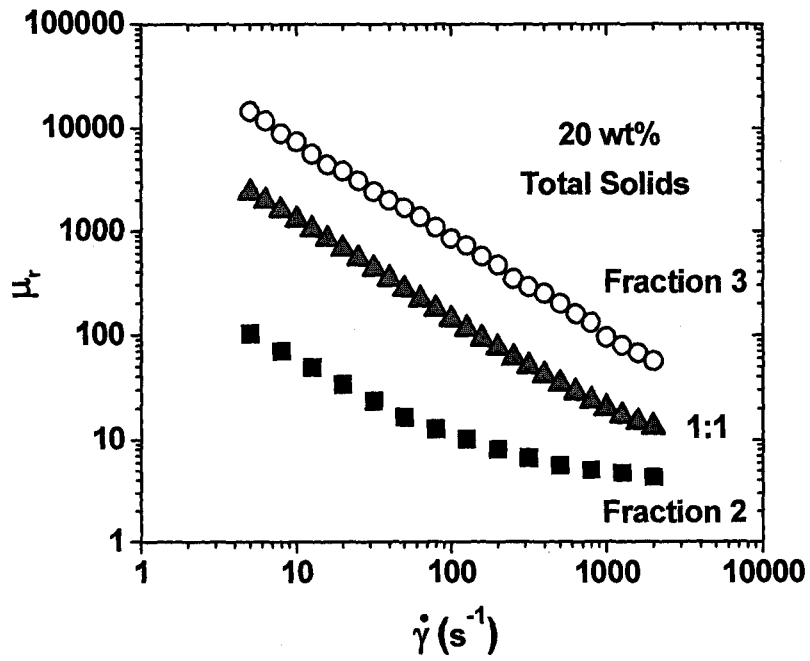
Figure 3.18 - Relative viscosity of a one-to-one combination of fractions 2 and 3.
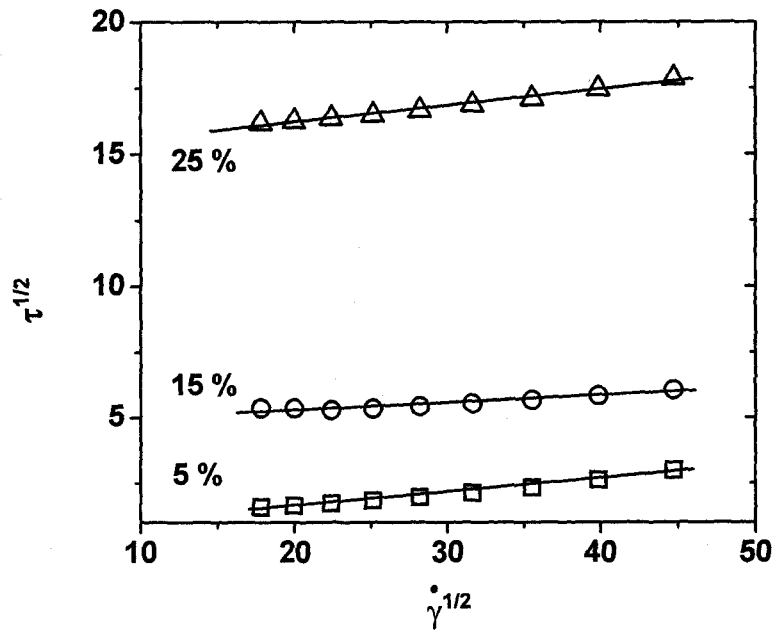
Figure 3.19 – Verifying the application of the Casson model to measure yield stress of suspensions of fraction 3.
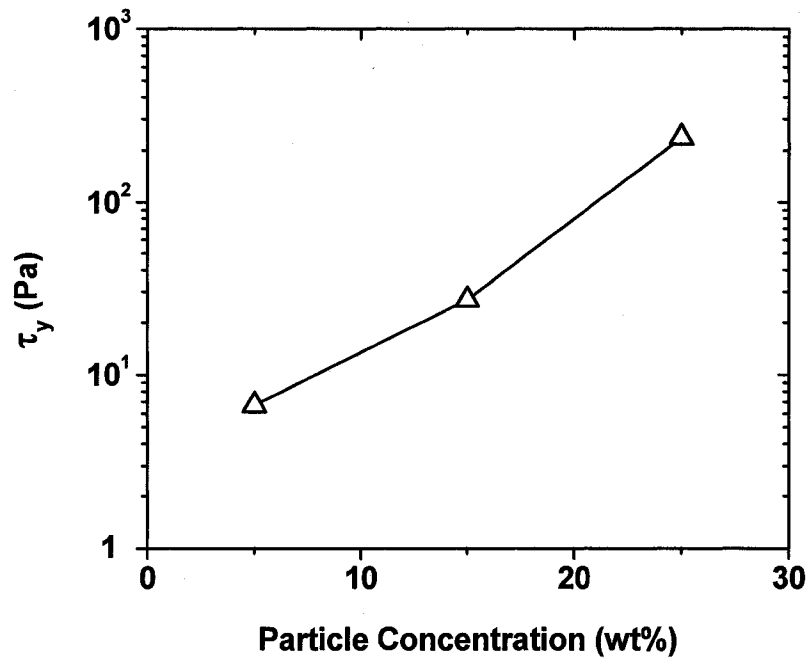
Figure 3.20 – Yield stress of fraction 3 as calculated by the Casson model.
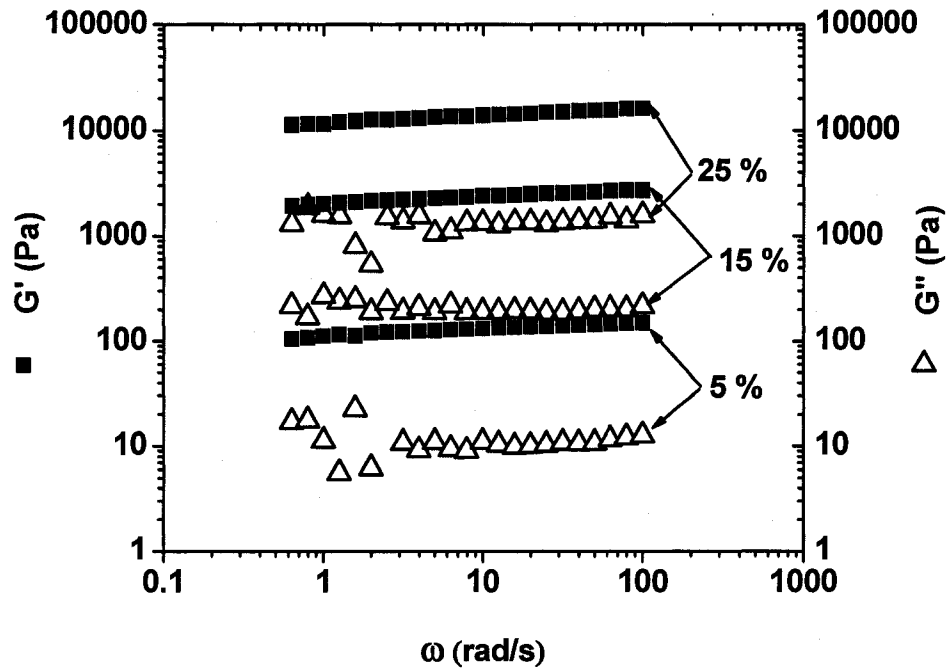
Figure 3.21 – Frequency sweep on suspensions of fraction 3.
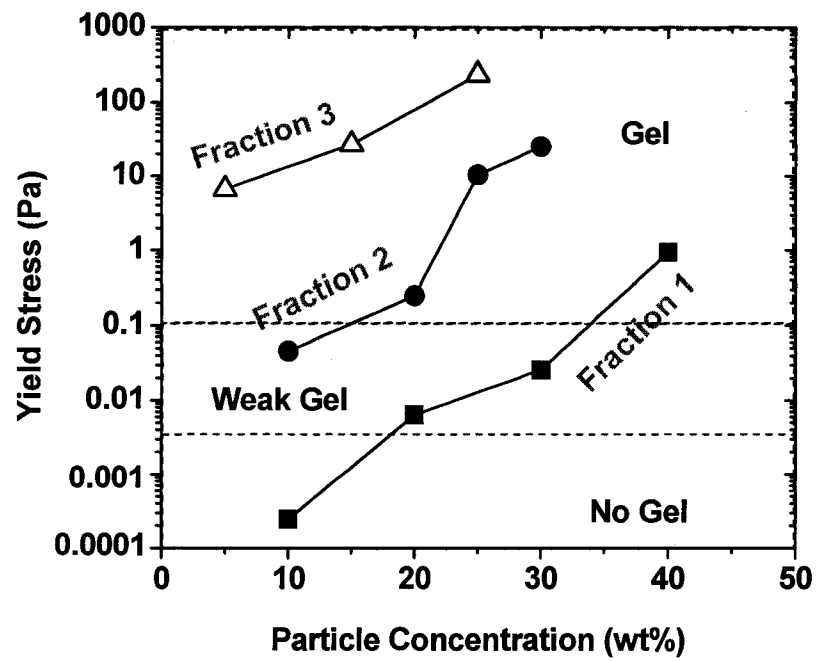
Figure 3.22 – Mapping the state of gelation for MFT ultra-fines.

Table 3.1 - Microstructural parameters derived from XRD domain size in the c^* crystallographic direction.

Sample	Specific surface area (m²/g) [Mean fundamental crystallite thickness - nm]			
	Illite-Smectite (77:23)	Illite	Kaolinite-Smectite (90:10)	Kaolinite
MFT	293 [2.6]	68 [11]	273 [3.3]	61 [15.3]
Gelled Middling	273 [2.8]	68 [11]	255 [3.5]	54 [17.5]

63

4.   Characterization of MFT Ultra-Fines

In Chapter 3 we discussed the rheological properties of suspensions formed from three MFT ultra-fine fractions in the indigenous water chemistry of mature fine tails. All fractions exhibited some degree of elasticity. For all fractions, a gelled structure was observed when the solids concentration in the suspensions exceeded a certain value. This concentration, however, varied significantly among the three fractions. Comparing suspensions of fractions 1 and 2 showed that, fraction 2 can form more viscous suspensions with a higher degree of elasticity. This behaviour was attributed to the number of particles which formed the suspensions. Consisting of particles of smaller sizes, fraction 2 provided a higher surface to volume ratio in its suspensions. This led to higher surface activity of the particles at a given particle concentration and increased suspension elasticity. Smaller particles were also capable of forming larger flocs and as such increased the solid-like (elastic) characteristic of their suspensions.

Among the three fractions, fraction 3 showed the strongest network formation capability. Compared to the other fractions, fraction 3 formed a viscoelastic gel with only a small amount of solids present in its suspension. This behaviour could not be explained based on the particle size distribution of the solids as both fractions 2 and 3 appeared to have nearly the same size distributions.

During the fractionation procedure fractions 2 and 3 were distinguished by their color difference. The particles in fraction 3 had a darker color that could be due to the presence of organic material on the particle surface. This was most likely as these solids were separated from oil sands tailings where the solids are in intimate contact with heavy organic compounds. The presence of the organic material was confirmed in the characterization measurements described in this chapter. In addition, further experiments were performed to explain the high gel formation tendency of fraction 3 as compared to fraction 2.

64

4.1. Content of Organic Matter

4.1.1. Thermogravimetric Analysis

In order to compare the organic content of the MFT ultra-fine fractions, thermogravimetric (TG) analysis was performed on dried forms of each fraction. Figure 4.1 shows the change in mass percent for each fraction as they were heated for an hour from room temperature to 600 °C. All three fractions lost a portion of their mass during the heating process. Fractions 1 and 2 both lost about 10% of their initial mass, while fraction 3 lost almost twice as much – with a 20% decrease in its mass.

At this point, the difference in thermal analysis results of the three fractions can be attributed to two separate factors. Based on XRD results, the MFT ultra-fines were identified as clay particles. Therefore, the mass loss observed in Figure 4.1 could partly be due to the loss of interlayer water of the clays in each fraction [45]. At the same time, organic matter in each fraction could decompose as a result of heating and lead to the observed decreased in the mass.

Considering that the two different phenomena could have caused the TG results, it was necessary to compare the fractions from a different point of view. Based on the similar mass loss curves of fractions 1 and 2, however, it could be concluded that fractions 1 and 2 were not different in terms of their water and/or organic matter content.

4.1.2. FTIR Spectroscopy

In order to compare the organic content of fractions 2 and 3, infrared spectrum of their dried forms were obtained. Figure 4.2 shows the FTIR patterns of fractions 2 and 3. Both fractions showed peaks at wavenumbers in the region 3550 to 3700 cm^{-1}. These peaks are related to the hydroxide groups associated with alumina. Also, both fractions had peaks between 900 and 1200 cm^{-1}. These peaks are related to silicon-oxygen bond. The patterns of Figure 4.2 also showed absorbance between 700 and 900 cm^{-1}. These peaks are due to the presence of aromatic organic compounds.

65

One difference between the patterns of fractions 2 and 3 was the appearance of peaks between 1400 and 1700 cm^{-1} on the spectrum of fraction 3. Absorbances in the region between 2800 and 3000 wavenumbers also appeared only on the spectrum of fraction 3. These peaks are related to certain aromatic and aliphatic carbon bonds. Therefore, it was reasonable to conclude that fraction 3 contained some organic compounds that are not found in fraction 2. In addition to the differences in peaks, absorbances in the spectrum of fraction 3 appear much stronger than that of fraction 2. Although fraction 2 contained some organic matter, the coverage on the particle surfaces is not as significant as in fraction 3. Similar behaviour was observed in the comparison of hydrophilic and biwettable ultra-fines in reference [17]. The organic material was identified to be mostly humic in nature, with some multi-ring compounds from bitumen that were chemically adsorbed to the base humic compounds.

4.2. Surface Wettability

With different amounts of organic matter in fractions 2 and 3, it was speculated that the degree of hydrophobicity of the particles in the two fractions were not similar. Contact angle measurements were performed on flat surfaces formed from ultra-fine solids in fractions 2 and 3. Figure 4.3a shows the images used for contact angle measurements. Figure 4.3b compares contact angles of the two fractions. The results showed that, compared to the particles in fraction 2, the particles in fraction 3 were more hydrophobic.

4.3. Long-Range Interaction and Adhesion Forces

Long-range interaction and adhesion forces were measured between the particles from fractions 2 and 3. The results in Figure 4.4 show that long-range interaction forces between the solids of both fractions was purely repulsive. These long-range interactions, however, followed different trends. Between the solids of fraction 2, repulsion between the particles appeared to be much more significant at larger separation distances. This is while the interaction force between the solids of fraction 3 was nearly zero at most of the

66

separation distances studied. The results in Figure 4.4 suggest a stronger potency of particle aggregation for fraction 3 particles than for fraction 2 particles, due to much weaker repulsion accounting for the lower gel strength in fraction 2 suspensions.

The results in the inset of Figure 4.4 show that the adhesion forces between the particles of both fractions were similar. The similar shear-thinning behaviour of the samples, as demonstrated in Chapter 3, could be related to the similar adhesion forces observed.

4.4. Mineralogy

Mineral compositions of the three ultra-fine fractions were determined using XRD analysis. Diffraction patterns of calcium saturated oriented slides at 54% relative humidity of the three fractions are shown in Figure 4.5. Mineral composition was identified through the same procedure as described for MFT and gelled middlings, described in the previous chapter. The diffraction data were analyzed using the Rietveld analysis software, AUTOQUAN^{TM} from GE Technologies [46].

Tables 4.1 and 4.2 show the mineral components of the three fractions. As was the case for the source of these ultra-fine solids, clay particles such as kaolinite and illite in discrete forms, as well as mixed forms of smectite as illite-smectite and kaolinite-smectite, were the main components of each fraction. Based on the results in Table 4.1, fraction 1 was mainly composed of quartz, kaolinite and some illite. The main components of fraction 2 were kaolinite and illite, both in discrete and mixed forms. Among other minerals, fraction 2 also contained some quartz. In contrast, mineral analysis on fraction 3 did not show any quartz particle in this fraction. The amounts of discrete illite and its mixed form with smectite were higher than in the other two fractions. Smectite, being a three-layered clay with swelling capacity, can lead to the high gelation tendency observed for fraction 3.

It is interesting to note the total surface area of each fraction given in the final row of Table 4.1. These results showed that the surface area of the particles increased from

67

fraction 1 to 3. The results in Table 4.2 show that the main contributors to the surface area of each fraction were the mixed forms of smectite.

Although the high surface area of fraction 3 could explain the high surface activity of these particles, this result contradicts the particle size measurements based on light scattering. Since the PSD of fractions 2 and 3 were similar, similar surface areas were expected as well. The high surface area obtained in XRD measurements would imply that the particles in fraction 3 were of smaller sizes. In order to confirm the particle sizes in fractions 2 and 3, SEM images (Figure 4.6) of the particles were captured. These images show that the unit particles in these fractions were indeed of different sizes and morphologies.

4.5. Particle Size or Organic Matter

Based on the results discussed thus far, the stronger solid-like properties of fraction 3 could be due to two different factors: smaller particle sizes and hydrophobic character of the particle surfaces; the latter could be due to the presence of organic matter on the particle surfaces. It would, however, be enlightening to reveal whether one of these factors in particular, or the combination of both, that would result in the stronger structures formed in fraction 3. In order to confirm how the above factors led to the observed rheological behaviour of fraction 3, the solids were studied in the absence of organic matter.

To remove the organic coating of the particles, the solids of fraction 3 were dispersed in a hydrogen peroxide solution and shaken vigorously. Hydrogen peroxide would oxidize the humic matter on the particle surfaces and separate them from the solids. Figure 4.7 shows the result of thermogravimetric analysis on the solids after removal of organic material from the particles surfaces. This figure showed that the mass loss of the dried particles decreased to 10 wt%, which was similar to the case for the solids of fractions 1 and 2.

68

After removing the organics, the solids were redispersed in MFT supernatant (approximately 2 g of solids in 50 mL of MFT supernatant). Table 4.3 gives a comparison of the solution chemistry of these solids with that of fraction 3 and MFT. The table shows that the ion concentration are similar and of the same order. The wash process did not alter the solution chemistry significantly. To ensure that the particle size was not affected by the hydrogen peroxide wash, SEM images of the particles in fraction 3 were captured after their organic coatings were removed (Figure 4.8). This image showed that removal of the organics did not cause any observable alterations in the particle sizes of fraction 3.

The washed solids were also compared to the original form of fraction 3 in terms of surface wettability of the particle surfaces. Flat particle surfaces here were prepared in the same manner as described for fractions 2 and 3 in section 2.4.6. Figure 4.9 shows the image used to measure the contact angle of the organic free solids of fraction 3. Contact angle of a droplet of MFT supernatant on solid surfaces in air was smaller for the organic free solids than the value measured for fraction 3 before hydrogen peroxide wash. This finding suggests that the higher hydrophobicity of fraction 3 was related to the organic compounds on the particle surfaces.

Comparison of the solids in the absence and presence of organics was completed by measuring the zeta potential of these particles in MFT supernatant water. Figure 4.10 shows the results of these measurements. The difference between the values obtained for the two solids fell within the error margin of the measurements. Washing the solids and removing the organics therefore did not cause a significant alteration in the zeta potential of the particles.

Figure 4.11 shows the results of a simple shear flow test on a 23 wt% suspension of fraction 3 after the organics were removed. The results were compared to the flow curve of a 20 wt% suspension of fraction 3 in its original form where the solids were not washed in hydrogen peroxide. Figure 4.11 shows that the non-Newtonian shear thinning behaviour of the suspension was maintained after removal of the organics. Recalling the

results presented in Chapter 3 and considering the increasing trend of the relative viscosity with particle concentration, the viscosity at 23 wt% was expected to be higher than that of a 20 wt% suspension – provided that the surface interaction of the particles were unaffected. However, Figure 4.11 shows that removing the organic matter from the surfaces of the particles reduced their suspension viscosity. The result of this flow test therefore implied that the high gelation propensity of particles in fraction 3 could mainly be attributed to the organic coating of the particle surfaces.

4.6. Effect of Calcium Ion

In order to investigate the effect of electrostatic forces on the rheological behaviour of fractions 2 and 3, simple shear flow tests were performed on suspensions of these fractions at different calcium chloride concentrations. The preparation method for the suspensions used in this section was described earlier in chapter 2. For both fractions, suspensions were prepared by adding a desired calcium chloride solution[‡‡‡] to a 30 wt% suspension of solids washed and dispersed in MFT supernatant. Particle concentrations of the test samples were maintained at 15 wt% in order to minimize differences that might arise because of the different amounts of added MFT supernatant. Different amounts of either MFT supernatant or calcium chloride solution in the suspensions could alter the ionic strength of the electrolyte solution and affect the rheology of the samples.

Figure 4.12 shows the relative viscosities of fraction 1 suspensions at a given solids concentration and different calcium content. Unlike the samples prepared in MFT supernatant, the solids dispersed in solutions of low calcium chloride concentrations did not show a non-Newtonian behaviour. Increasing calcium concentration in the suspensions, however, caused the non-Newtonian shear thinning behaviour to reappear.

Figure 4.13 shows the zeta potential of fraction 2 solids as different calcium ion concentrations were introduced to the suspensions. Based on the results, it is noted that adding calcium ions to the suspensions lowered the negative value of electric potential at

---

[‡‡‡] 0, 20, 60, 100, 500 and 1000 ppm (milligrams $CaCl_2$ per liter of deionized water)

70

the shear plane of the particles. Decreased zeta potentials (values closer to zero) suggests lower repulsive forces between the solid particles.

Noting the variations of ion content in the suspensions with respect to calcium ion addition (Figure 4.14), the reduced electric potential can be due to two different phenomena. Since the contents of both sodium and potassium ions in the suspending water of the samples were increased, part of the decreased zeta potential could be related to exchanged surface calcium ions. In addition, increasing electrolyte concentration in the system and increasing its ionic strength could lower the zeta potential of the solids. Both scenarios here would decrease the electric repulsion of the system and cause particle agglomeration and structure formation in the suspensions. The increased viscosity of the suspensions at higher calcium concentration in Figure 4.12 is an indication of structure formation of the solids.

Similar tests were performed in order to investigate the behaviour of fraction 3 with changing calcium concentration. Figure 4.15 shows the results of flow tests on suspensions of fraction 3 with different contents of calcium chloride added to the suspensions. For all calcium concentrations, the suspensions showed non-Newtonian shear thinning behaviour, where increasing the concentration of calcium in the suspensions increased viscosity.

Figure 4.16 shows the zeta potential of fraction 3 solids with respect to calcium concentration of the solution. Similar to what was observed for fraction 2, increasing the content of calcium in the samples shifted the zeta potential of fraction 3 to less negative numbers. In comparison to the suspensions of fraction 2, both solids followed the same trend in their zeta potential variations. However, fraction 3 appeared to have slightly lower zeta potential values. The ionic concentration of the suspensions used in flow tests of fraction 3 was also measured by atomic absorption spectroscopy. The results (Figure 4.17) showed that the ion content in these suspensions was similar to that of fraction 2. This behaviour indicated that the same phenomena were responsible for decreasing the zeta potential of solids in suspensions of fraction 3.

71

As the zeta potential of the suspended solids from both fractions 2 and 3 followed the same trends, different rheological behaviours observed for these fractions cannot be related to the electrostatic relations in particular. The consistent behaviour in the non-Newtonian characteristics of fraction 3 with changing calcium concentration further established the presence of different interactions between the solids in fraction 3 as compared to those existing in fraction 2. As stated in Section 4.3, the presence of organic matter on the surfaces of the particles in fraction 3 was recognized as the cause of decreased repulsion between the particles leading to higher number of flocs formed and to non-Newtonian behaviour even at lower ionic concentrations.

72
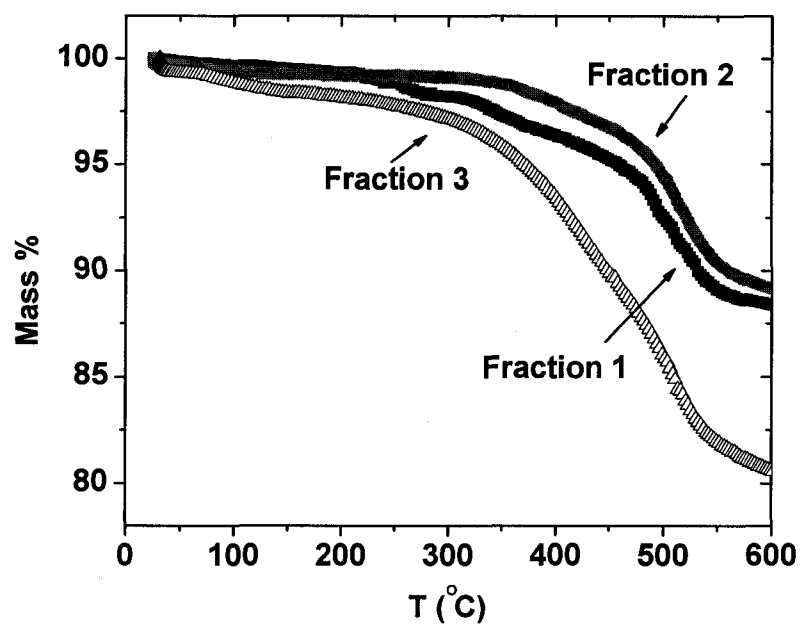
Figure 4.1 – Thermogravimetric analysis of fractions 1 to 3.
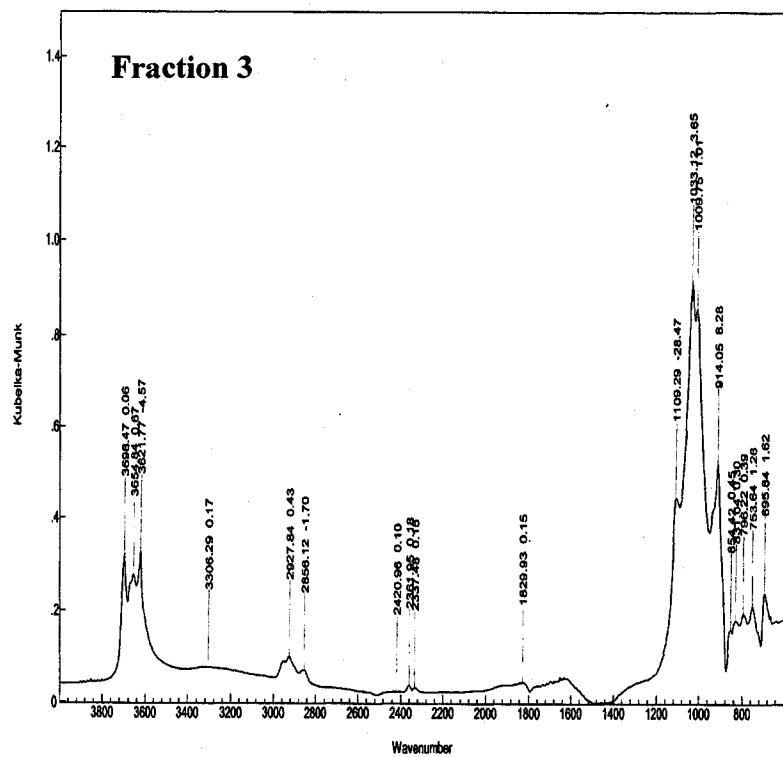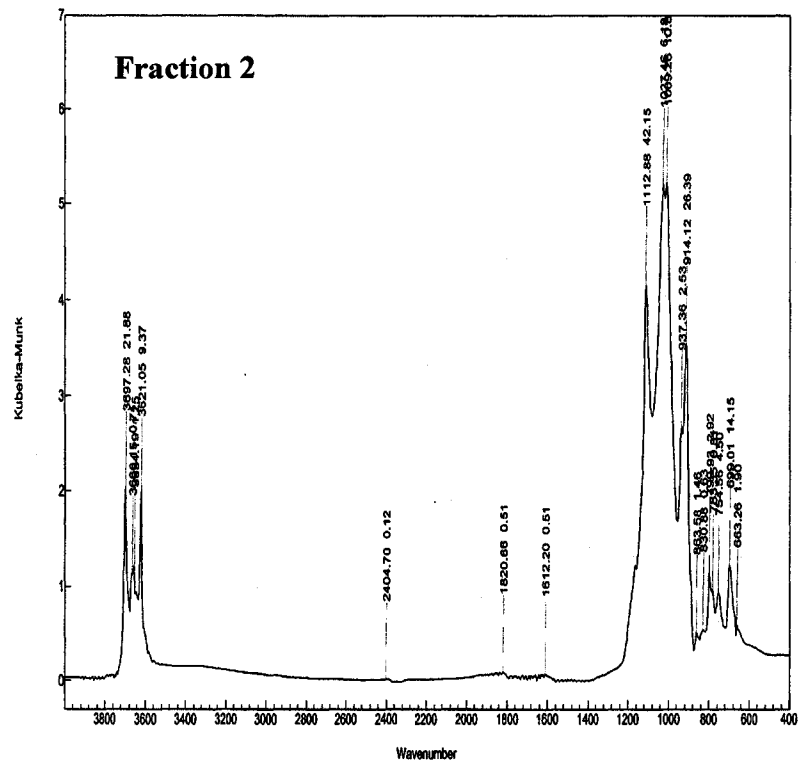
Figure 4.2 – FTIR patterns of fractions 2 and 3.

74
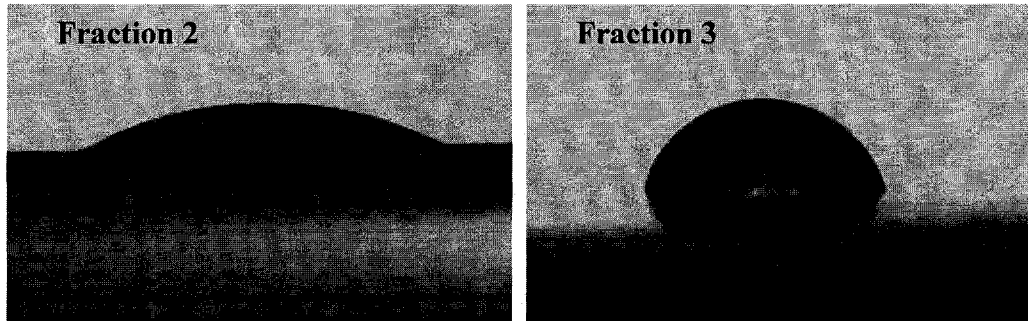
a)
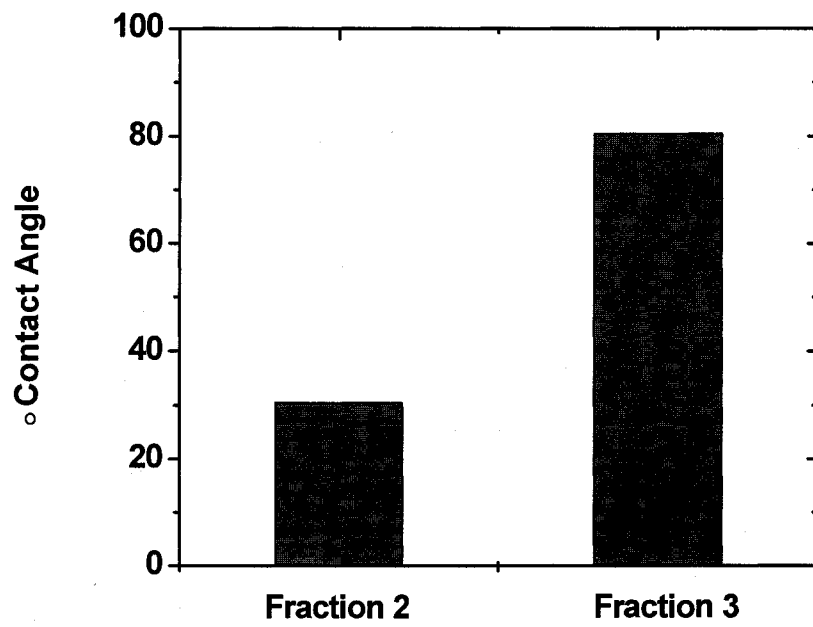
b)

Figure 4.3 – Contact angle measurement on fractions 2 and 3.

75
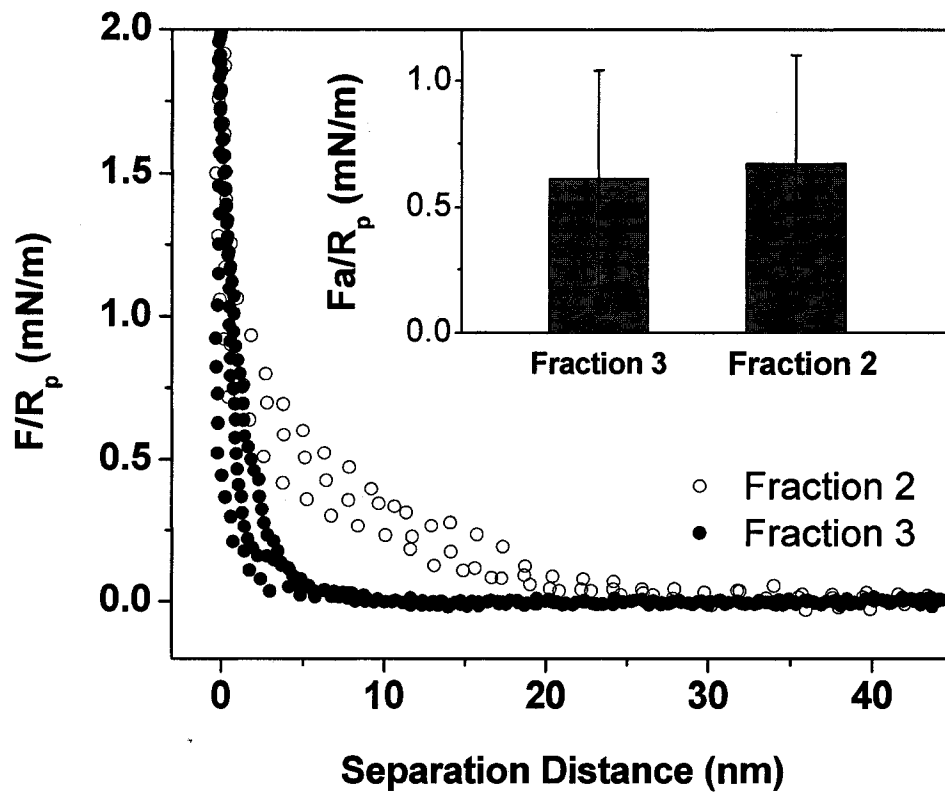
Figure 4.4 – Long-range interaction and adhesion forces between pairs of particles from fraction 2 and fraction 3.
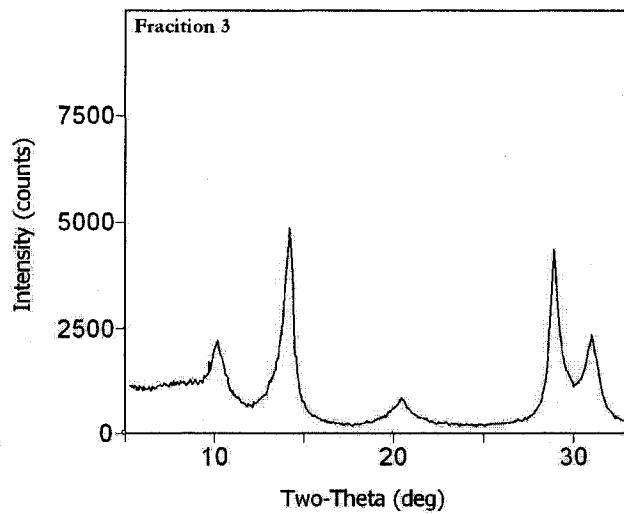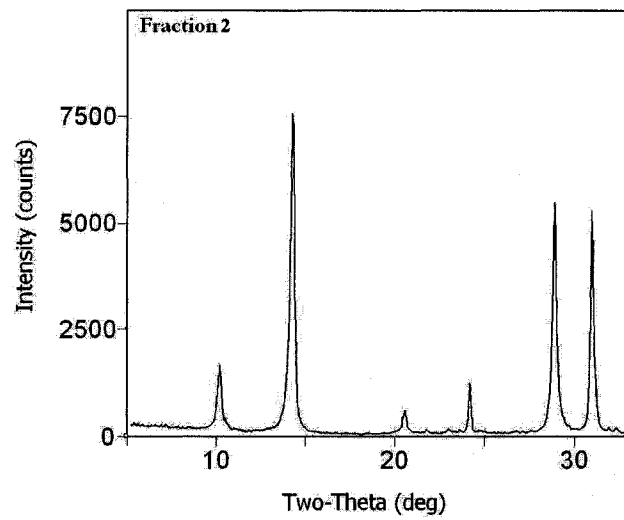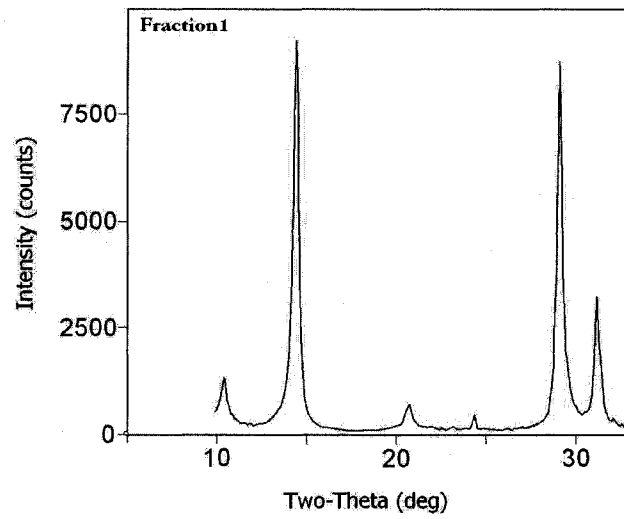
Figure 4.5 - Diffraction patterns of calcium saturated oriented slides of the three ultra-fine fractions in 54% relative humidity.
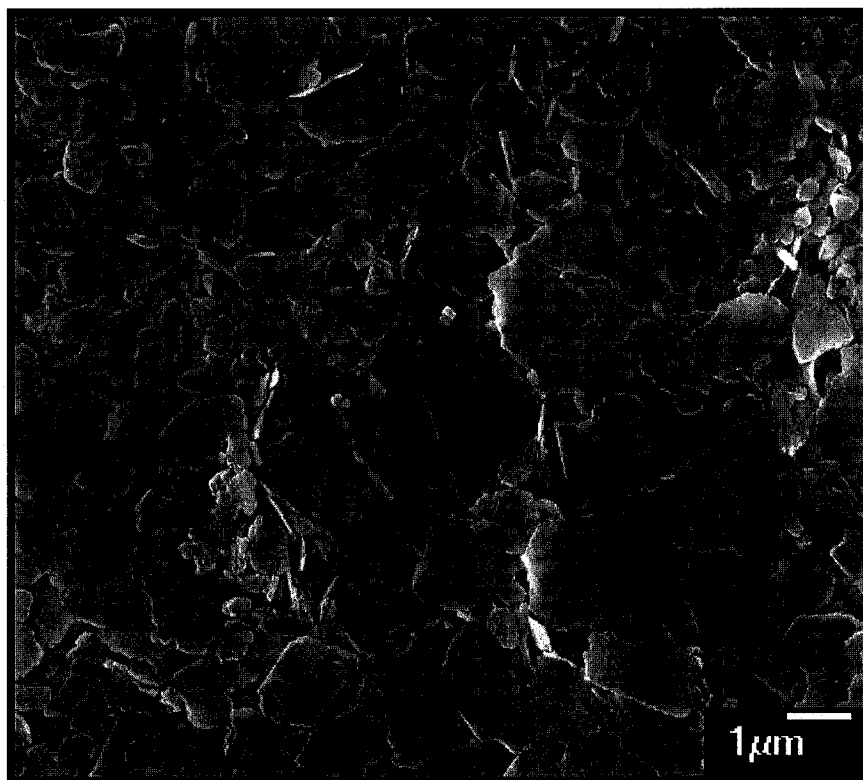
(a)
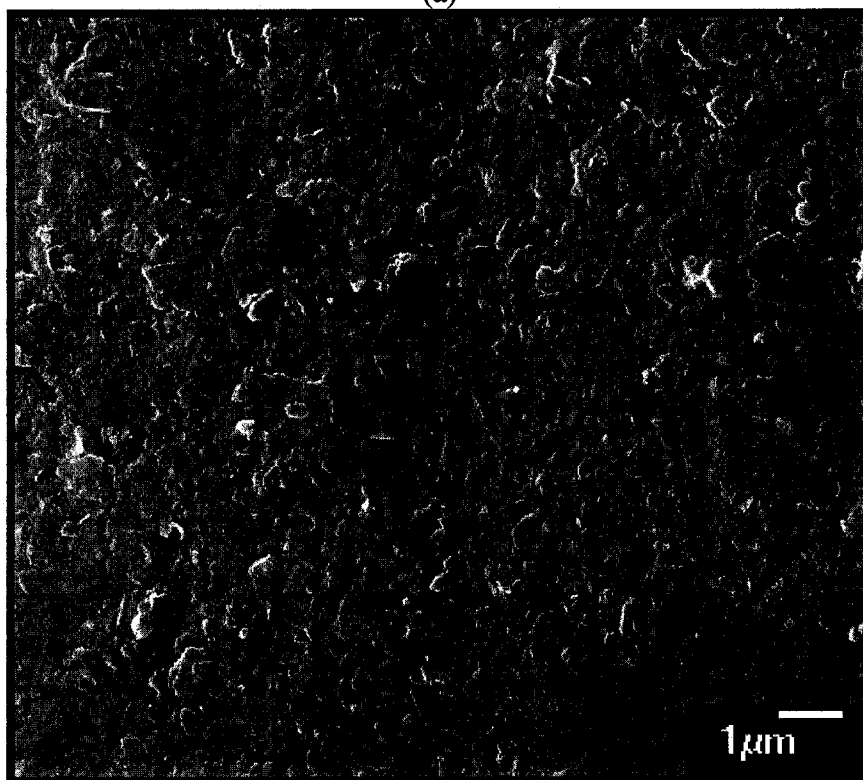
(b)

Figure 4.6 - Scanning electron micrographs of a) fraction 2 and b) fraction 3

78
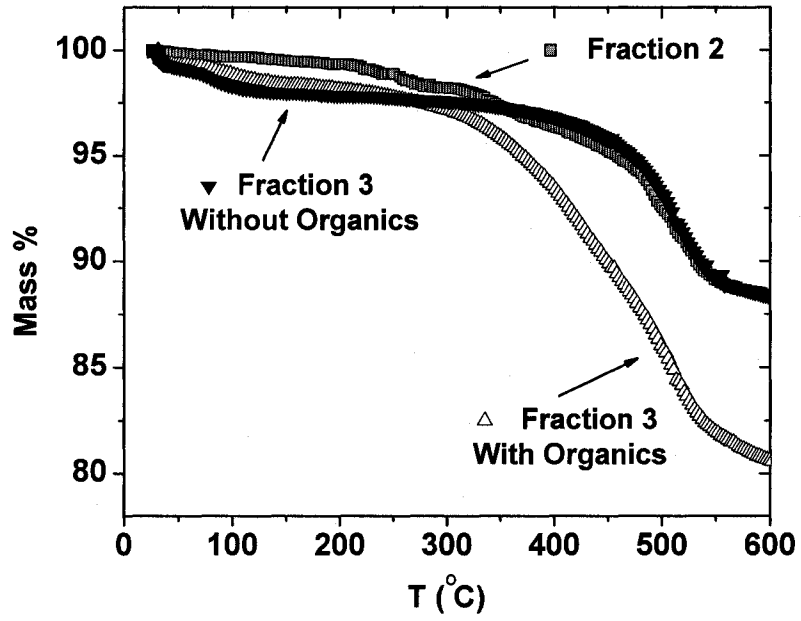
Figure 4.7 – Thermogravimetric analysis of fraction 3 after washing the solids in H_2O_2.
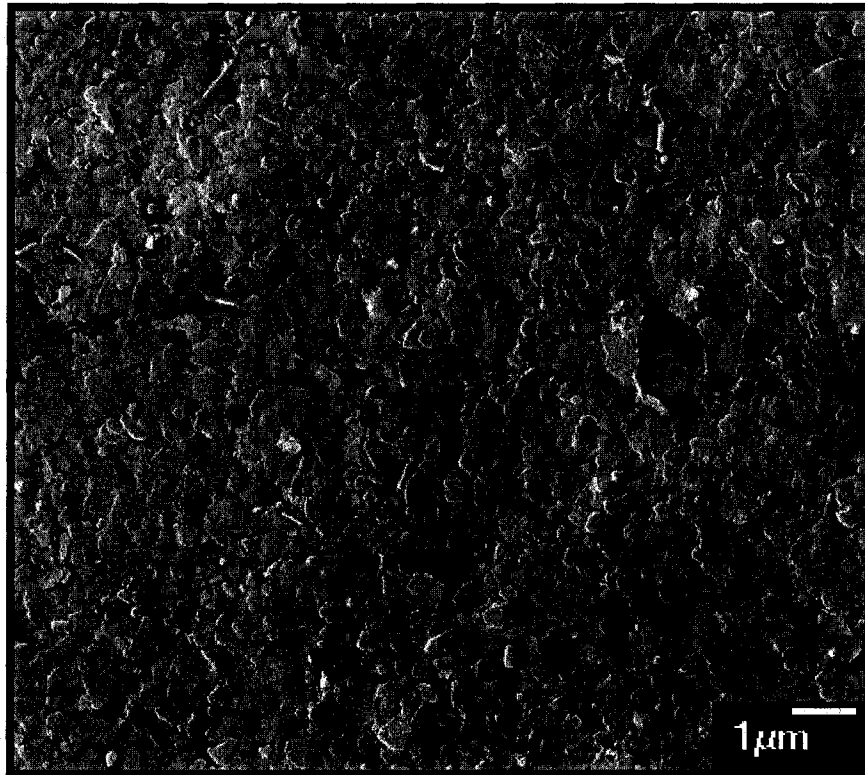
Figure 4.8 – SEM image of fraction 3 after washing the solids in H_2O_2.

79

θ = 23.3 °   θ = 80.5 °
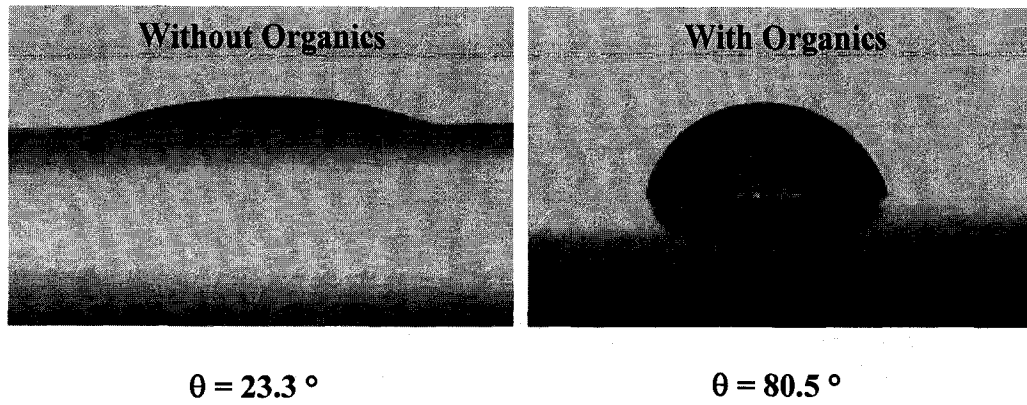
Figure 4.9 – Contact angle measurement of MFT supernatant on the organic free surface of fraction 3 solids in air.
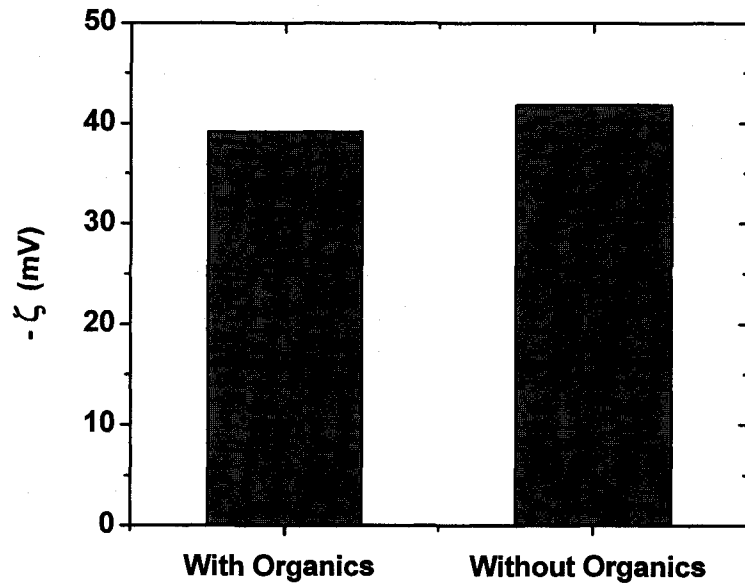
Figure 4.10 – Zeta potentials of solids in fraction 3 in the original form and after treatment with hydrogen peroxide to remove the organic coating of the solids. Both measurements were carried out in MFT supernatant water.
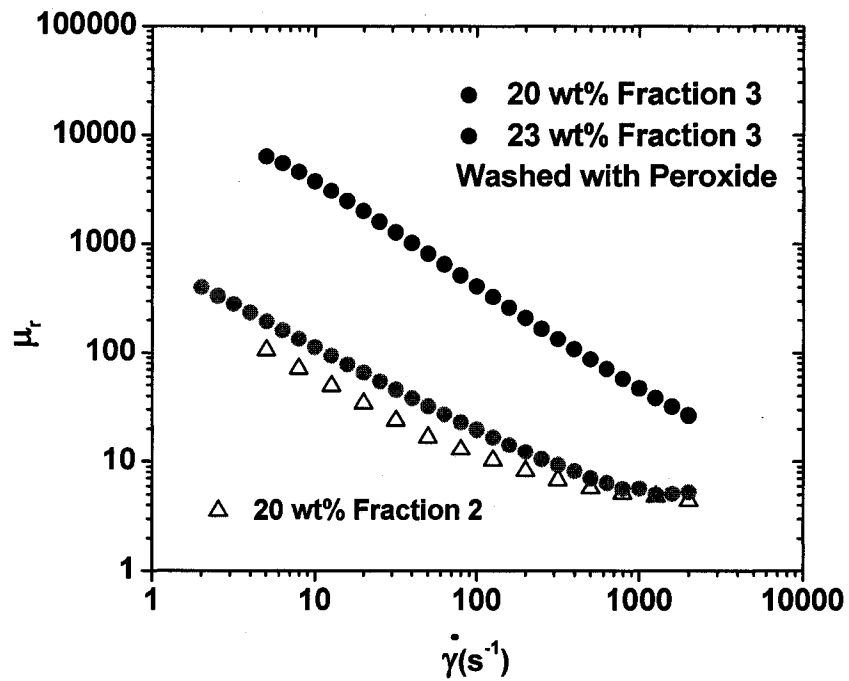
Figure 4.11 – Flow test on fraction 3 with and without the organic coating of the solids.
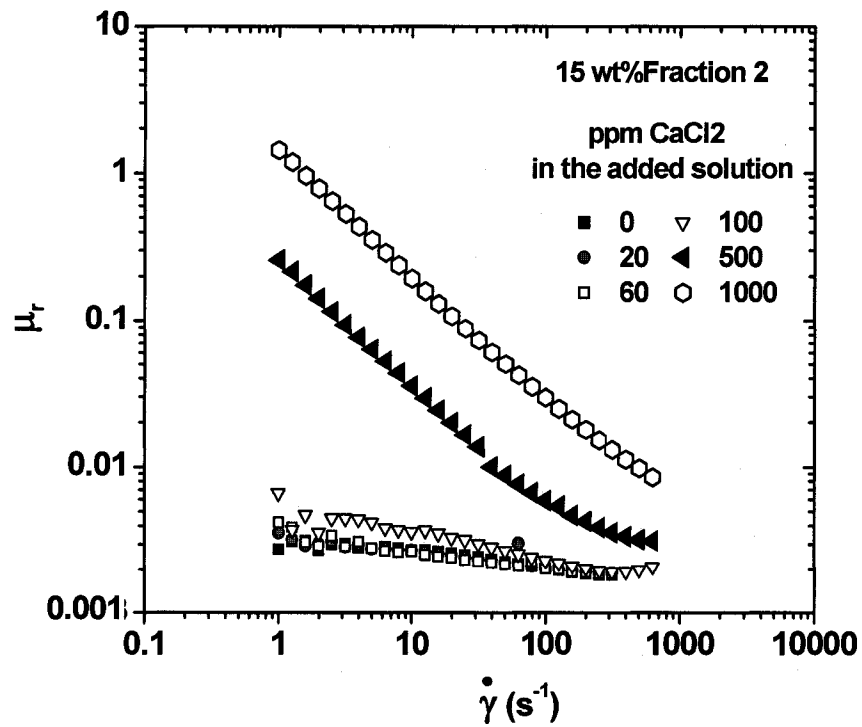
Figure 4.12 – Flow test results of fraction 2 for different amounts of calcium added.
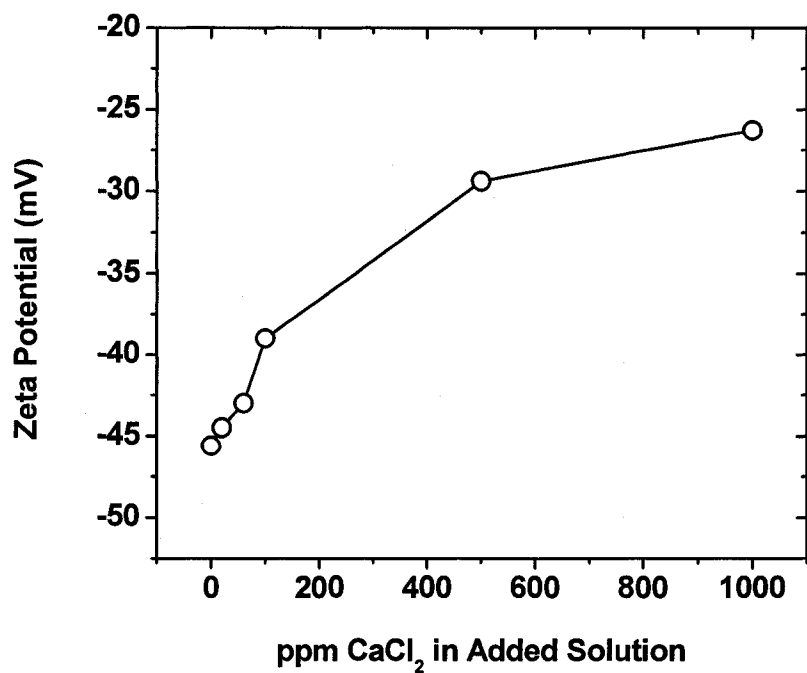
Figure 4.13 – Zeta potential of solids in fraction 2 suspensions prepared with different calcium chloride solutions.
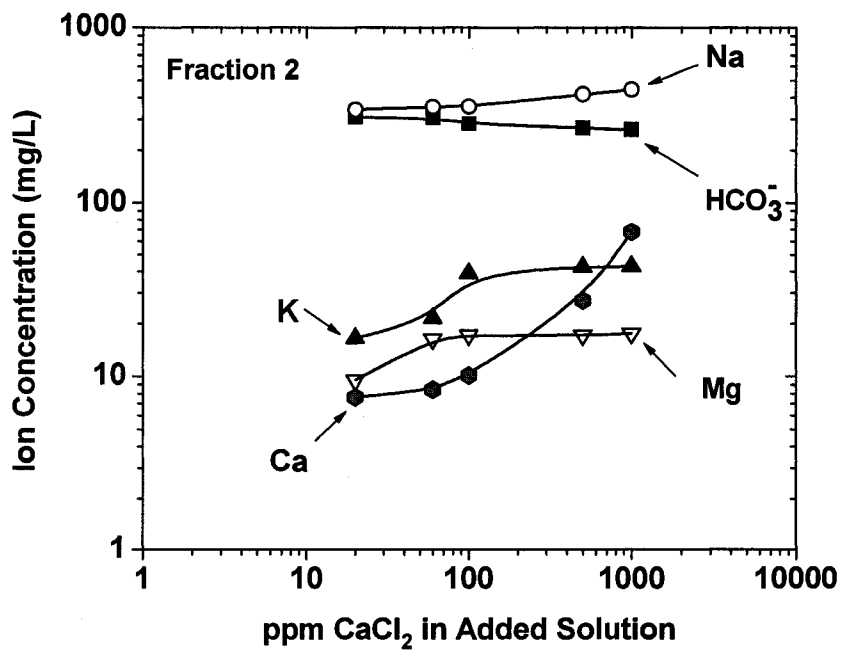
Figure 4.14 – Ion concentration in fraction 2 suspensions prepared with different calcium chloride solutions.

82
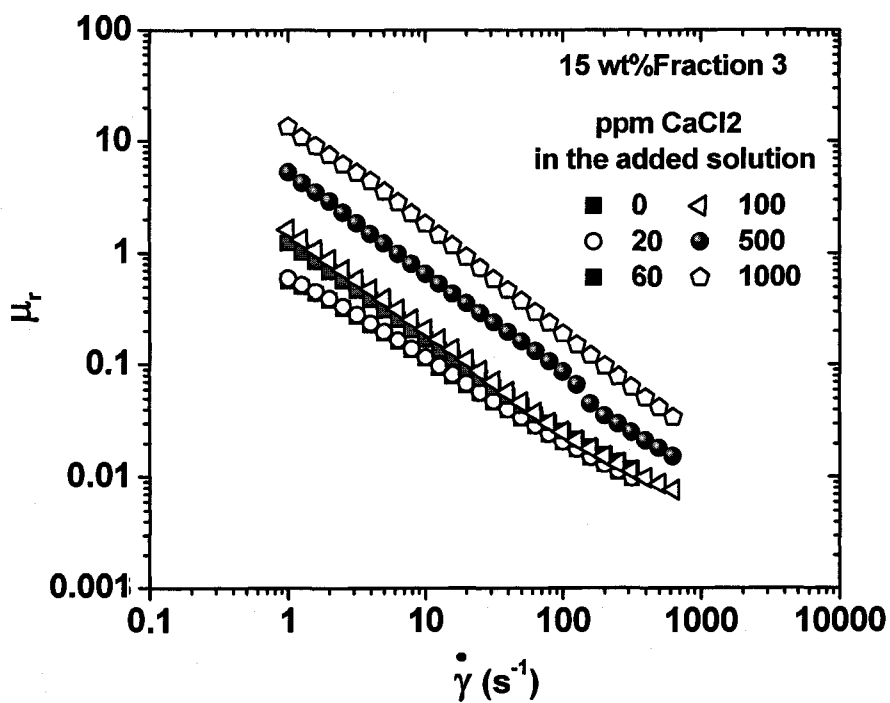
Figure 4.15 - Flow test on fraction 3 at different calcium concentrations.
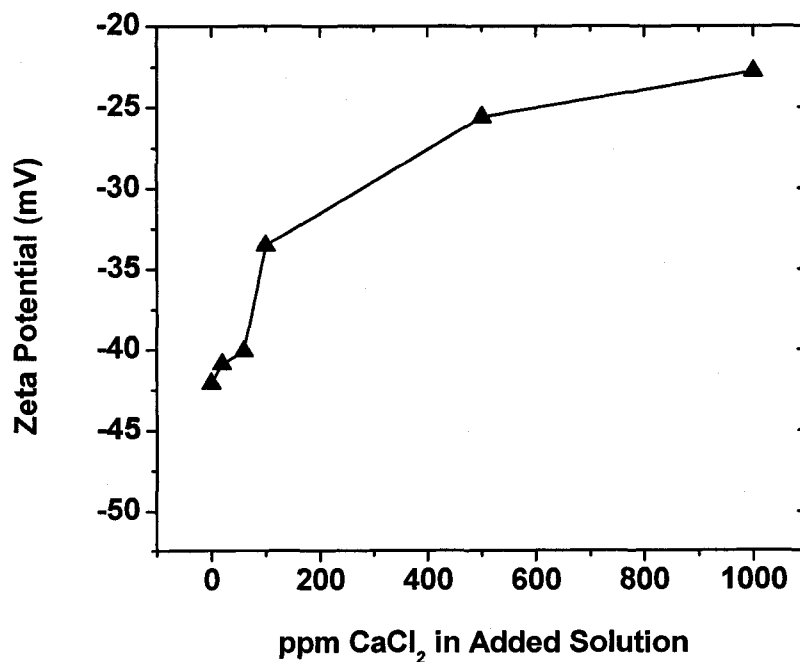
Figure 4.16 - Zeta potential of solids in fraction 3 suspensions prepared with different calcium chloride solutions.

83
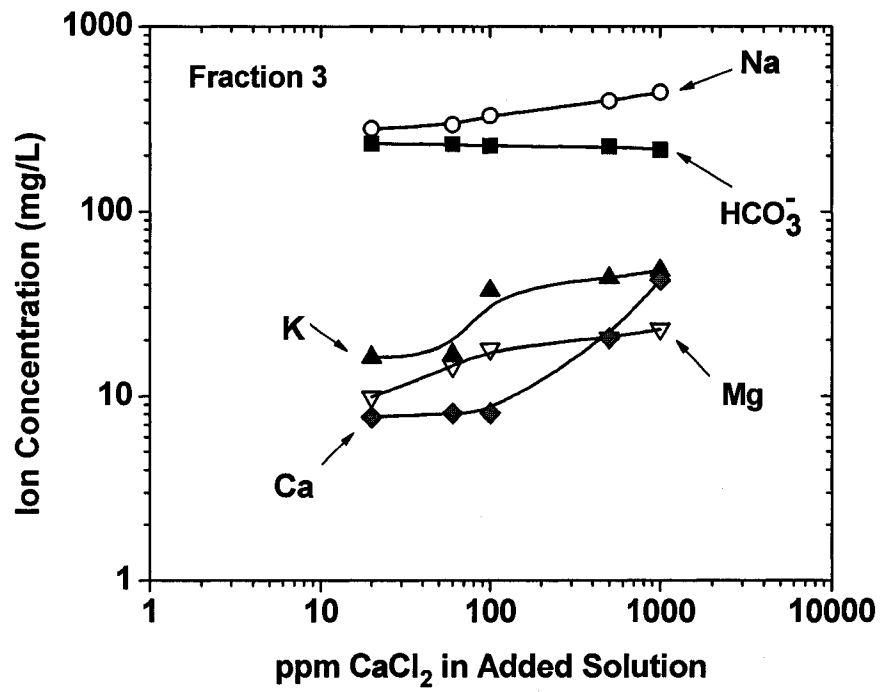
Figure 4.17 - Ion concentration in fraction 3 suspensions prepared with different calcium chloride solutions.

Table 4.1 - Mineral composition of clay fractions (wt%).

Mineral Group	Mineral Type	Fraction 1 10-μm	Fraction 2 0.3-μm light	Fraction 3 0.3-μm dark
	Quartz	27.9 ± 0.5	8.5 ± 0.6	
Carbonates	Ankerite	0.6 ± 0.2	0.3 ± 0.2	
	Calcite	1.8 ± 0.6	2.1 ± 1.1	
	Siderite	5.2 ± 0.3	1.1 ± 0.4	
Feldspars	K-spar	1.3 ± 0.4	1.9 ± 0.5	
	Plagioclase	0.8 ± 0.3	0.7 ± 0.4	
	Pyrite	0.4 ± 0.1	0.2 ± 0.1	
	Anatase	1.0 ± 0.2	1.3 ± 0.2	
	Rutile	0.6 ± 0.2	0.8 ± 0.3	
Clay Minerals	Chlorite	1.8 ± 0.5	2.2 ± 0.6	
	Kaolinite (90) – smectite	bdl[*]	7.5 ± 0.7	14.6 ± 0.8
	Kaolinite	41 ± 0.7	41.6 ± 0.7	19.7 ± 1.0
	Illite(77)-smectite	3.9 ± 0.7	16.7 ± 0.7	33.5 ± 1.7
	Illite	14.0 ± 0.7	15.8 ± 0.7	32.4 ± 1.7
	Estimated total surface area (m^2/g)	22 ± 1	86 ± 4	174 ± 9

[*]bdl – below detection limit

85

Table 4.2 - Surface area derived from XRD domain size in the c* crystallographic direction. Clay minerals are the most significant contributors to the total surface area. Contribution of chlorite is negligible.

Sample	Specific surface area (m^2/g)			
	Kaolinite (90)-Smectite	Kaolinite	Illite (77)-Smectite	Illite
Fraction 1 10-μm		26	228	17
Fraction 2 0.3-μm light	258	35	280	38
Fraction 3 0.3-μm dark	260	52	293	87

Table 4.3 - Solution chemistry of the solids in fraction 3 redispersed in MFT supernatant after washing in hydrogen peroxide.

	Ionic concentration (mg/L)					
	HCO_3^-	CO_3^{2-}	Na	K	Mg	Ca
MFT supernatant	568.0	116.1	866.3	14.6	7.4	7.7
Fraction 3	548.5	30.3	669.2	12.7	10.1	17.6
Fraction 3 without organics	624.2	68.7	855.2	15.8	8.16	11.8

86

5.   Conclusions

5.1. Problem Review

Dependence of the modern world on petroleum energy is likely to continue in the foreseeable future. With the ever increasing demand for energy and escalating oil prices, much attention has been drawn to Alberta's oil sands resources. The Athabasca oil sands deposits are among the largest in the world. As the conventional oil supplies begin to deplete in the coming decades, the Canadian oil sands industry will become an increasingly important force in the global energy market. For the industry to be competitive, it is crucial to maximize the efficiency of oil sands extraction methods and minimize hydrocarbon loss to the tailings. This can be accomplished through understanding of basic mechanisms which underlie the various extraction processes.

In regard to the conventional, water based extraction process that is widely used for bitumen recovery, colloidal clay particles contribute greatly to some of the most challenging problems in the oil sands industry. While gravity separation is capable of recovering most of the bitumen from the ore, clay particles are not easily removed from the suspension. These suspended clays lead eventually to large volumes of non-consolidating tailings. The storage of oil sands tailings in large ponds has led to many environmental and economical concerns. The amount of river water that cannot be recovered from the tailings has been a matter of controversy in the past years. Entrapment of emulsified bitumen droplets in the tailings structures, as well as disposal of the reject tailings, have been the subject of many studies.

In addition to the problems with the reject solids, colloidal particles can also hinder the gravity separation process and reduce the recovery rate significantly. Ultra-fine solids are known to affect the structure of the slurry in flotation vessels. Forming gelled structures, these solids block the flow path of bitumen and solids. Avoiding gelation in the separation process depends on detailed understanding of the flow properties of oil sands slurries.

87

In this study, three ultra-fine fractions (fractions 1 to 3) were separated from oil sands tailings (MFT). The objective of this work was to investigate the behaviour of oil sands solids and the rheology of their suspensions with little change in surface properties of the solids. Particles that contributed most to structure formation within the dispersions were identified through rheological measurements. Critical conditions that could lead to gelation and severe structure formation in the suspensions were identified in terms of particle concentration and solids type. Characterization measurements were then utilized to identify the properties of these solids which led to the rheological properties observed. The following section summarizes the major findings derived from this work.

5.2. Experimental Results

Three ultra-fine fractions of solids were isolated from MFT. All three fractions, when dispersed in the water of mature fine tails, formed non-Newtonian shear thinning suspensions above a given solids content. The non-Newtonian behaviour observed became more discernible as particle concentration in the suspensions was increased. Increase of particle concentration also increased the relative viscosities of all samples. Oscillatory tests on these samples confirmed that in a given fraction, increasing the solids content of the suspensions can change a dispersed ungelled system to a gelled system.

The rheological behaviour of the three fractions also showed that fraction 2 ($d_{50} = 0.14$ μm), which contained particles smaller than those in fraction 1 ($d_{50} = 5.96$ μm), could form more viscous suspensions of higher gel strength at a given solids concentration. Among the three fractions, however, fraction 3 had the highest gel strength and viscosities.

Characterization measurements on fraction 3 showed that the particle surfaces in this fraction were coated with organic compounds, some of which were not present in fraction 2. Based on the characterization measurements, fraction 3 contained the highest amount of organics relative to the other fractions. Comparing the surface wettability of the

88

particles in fractions 2 and 3 showed a higher hydrophobicity of solids in fraction 3. This property was related to the presence of organic matter on the particle surfaces. Scanning electron micrographs of fractions 2 and 3 showed that fraction 3 contained the smallest particles sizes among the three fractions. Due to formation of tactoids, these particle sizes could not be evaluated correctly by light scattering techniques. Mineral analysis of the three fractions showed the presence of different types of clays in these fractions. Among the three fractions of solids, fraction 3 contained a higher content of smectite which is a swelling clay and can greatly contribute to strong gelation characteristics.

In order to determine which property of fraction 3 led to its high viscosities and gel strength, relative viscosity of this fraction was studied in the absence of organic matter coating the particle surfaces. While removing the organics did not affect particle size, zeta potential or ionic strength of its dispersing medium, the hydrophobicity of the particle surfaces were reduced significantly. Comparing the relative viscosities of fraction 3 with and without the organics showed a significant decrease in the viscosity of this fraction. This experiment proved that the high tendency of fraction 3 to gel was related to its high organic content.

The role of electrostatic forces in the structure formation of ultra-fine solids was determined through further rheological measurements performed in the presence of calcium ions. While suspensions of fractions 2 and 3 showed non-Newtonian shear thinning behaviour at high concentrations of calcium chloride, decreasing ion concentration in suspensions of fraction 2 eliminated the shear thinning effect. Fraction 3, however, maintained its non-Newtonian behaviour at all calcium chloride concentrations. Since both fractions 2 and 3 followed a similar trend in their zeta potential variations with calcium concentration, this was additional proof that phenomena other than electrostatic interactions were responsible for the strong structures formed in fraction 3 suspensions.

In conclusion, the experimental work here showed that the organic rich ultra-fine solids in oil sands tailings contribute greatly to structure formation within the aqueous

89

suspensions. The organic matter renders the particle surfaces hydrophobic. With less repulsion between the particles, the organic rich solids showed the capability of forming networked structures of high gel strength.

5.3. Recommendations for Future Work

This study revealed the effect of organic coated ultra-fine solids on increasing the viscosity and solid-like characteristic of oil sands suspensions. However, in order to successfully counterbalance the gelling character of the organic rich solids, the following questions need to be answered:

- What is the nature of the organic matter on the particle surfaces? Are the organics naturally adsorbed on the clays or the extraction process is a major contributor to the formation of organic rich solids?
- What is the chemical composition of the organic compounds?
- How does the presence of organic matter alter the repulsion between the particles?
- Why the organic compounds are mostly associated with the fine solid fraction?

Although the results presented here clearly showed the networking property of solids in the presence of organic matter, the exact mechanism of particle interactions in this case was not evident. Further studies are therefore required to clarify the nature of particle associations. In addition, chemical composition of the organics as well as the original source of these compounds could initiate alternative solutions to avoid structure formation in oil sands suspensions.

References

[1]   Energy Statistics Handbook, Statistics Canada, Oct-Dec (2006)

[2]   Oil Sands, Alberta Energy, Government of Alberta, http://www.energy.gov.ab.ca

[3]   Canada's Oil Sands and Heavy Oil: Developing the World's Largest Petroleum Resource, Petroleum Communication Foundation, Apr (2000)

[4]   Liu, J., Xu, Z., Masliyah, J., Role of fine clays in bitumen extraction from oil sands, AIChE Journal, v 50, n 8, p 1917-1927 Aug (2004)

[5]   Zhou, Z. A., Xu, Z., Masliyah, J.H., Czarnecki, J., Coagulation of bitumen with fine silica in model systems, Colloids and Surfaces A: Physicochemical and Engineering Aspects, 148 199-211 (1999)

[6]   Canada's Oil Sands, Opportunities and Challenges to 2015: An Update, National Energy Board, Jun (2006)

[7]   Masliyah, J., Xu, Z., Fundamentals of Oil Sands Extraction, Custom Courseware for a Course at the University of Alberta Chemical and Materials Engineering Department, Winter (2006)

[8]   Eckert, W. F., J. H. Masliyah, M. R. Gray, P. M. Fedorak, Prediction of sedimentation and consolidation of fine tails, AIChE 42 960-972 (1996)

[9]   van Olphen, H., An Introduction to Clay Colloid Chemistry, Interscience Publishers, John Wiley and Sons, New York, (1963)

[10]   Masliyah, J., Bhattacharjee, S., Electrokinetic and Colloid Transport Phenomena. John Wiley & Sons, Inc. (2006)

[11]   Shaw, D. J., Introduction to Colloid and Surface Water Chemistry, Butterworth Publishers, (1970)

[12]   Solid Liquid Dispersions, Edited by T. F. Tadros, Academic Press Inc. (1987)

[13]   H. A. Barnes, J. F. Hutton and K. Walters. An Introduction to Rheology. Elsevier, Amsterdam (1989)

[14]   C. W. Macosko. Rheology: Principles, Measurements and Applications. Wiley-VCH (1994)

[15]   Schramm, L. L., "The influence of suspension viscosity on bitumen rise velocity and potential recovery in the hot water flotation process for oil sands," Journal of Canadian Petroleum Technology 28 73-80 (1989)

[16]   Chong, J., S. Ng, K. H. Chung, B. D. Sparks, L. S. Kotlyar, "Impact of fines content on a warm slurry extraction process using model oil sands," Fuel 82 425-438 (2003)

[17]   Sparks, B. D., L. S. Kotlyar, J. B. O'Carroll, K. H. Chung, "Athabasca oil sands: effect of organic coated solids on bitumen recovery and quality," Journal of Petroleum Science and Engineering 39 417– 430 (2003)

[18]   Tu, Y., J. B. O'Carroll L. S. Kotlyar, "Recovery of bitumen from oil sands: Gelation of ultra-fine clay in the primary separation vessel," Fuel 84 653-660 (2005)

[19]   Chow, R., "Rheology of Oil Sands Slurries," Oil sands Conference, University of Alberta, (2006)

[20]   Angle, C.W., R. Zrobok, H.A. Hamza, "Surface properties and elasticity of oil-sands-derived clays found in a sludge pond," Applied Clay Science, 7 455-470 (1993)

[21]   Ripmeester, J. A., Sirianni, A. F. , Recovery of Water and Bitumen From the Athabasca Oil Sand Tailing Ponds, JCPT, 20 (1): 131-133 (1981)

[22]   Kessick, M. A., Structure and Properties of Oil Sands Clay Tailings, JCPT 18 (1): 49-52 (1979)

[23]   Ripmeester, J. A., Kotlyar, L. S., Sparks, B. D. ^{2}H NMR and the Sol-Gel Transition in Suspensions of Colloidal Clays, Colloids and Surfaces A: Physicochemical and Engineering Aspects 78: 57-63 OCT (1993)

[24]   Kotlyar, L. S., Sparks, B.D., Schutte, R., Woods, J. R., Understanding of Fundamentals – Key to Process modification for Tailings Reduction. Journal of Environmental Science and Health Part A – Environmental Science and Engineering and Toxic and Hazardous Substance Control 28 (10): 2215-2224 (1993)

[25]   Majid, A., Sparks, B. D., Role of hydrophobic solids in the stability of oil sands fine tailings, Fuel, v 75, n 7, p 879-884 (1996)

[26]   Majid, A., Sparks, B.D., Ripmeester, J. A., Characterization of insoluble organic matter associated with non-settling clay minerals from Syncrude sludge pond tailings, Fuel, v 69, n 2, p 145-150 (1990)

[27]   Gimsa, J. , Eppmann, P., Pruger, B., Introducing phase analysis light scattering for dielectric characterization: Measurement of traveling-wave pumping, Biophysical Journal 73 (6): 3309-3316 (1997)

[28]   Spectroscopy source book, Sybil P. Parker, editor in chief. New York : McGraw-Hill, (1988)

[29]   Eshel, G., Levy, G. J., Mingelgrin, U., Singer, M. J., Critical evaluation of the use of laser diffraction for particle-size distribution analysis, Soil Science Society of America Journal 68 (3): 736-743 (2004)

[30]   Moore, D. M., Robert, C. R. Jr., X-ray diffraction and the identification and analysis of clay minerals, Oxford University Press (1997)

[31]   Li, H., Long, J., Xu, Z., Masliyah, J.H., Flocculation of clay suspensions using a temperature-sensitive polymer, AIChE 53 479-488 (2007)

[32]   Omotoso, O., Mikula, R., Stephens, P.W., Surface area of interstratified phyllosilicates in Athabasca oil sands from synchrotron XRD, Advances in X-ray Microanalysis, 45 391-396 (2002)

[33]   Reynolds, R. J., NEWMODTM Clay modeling software (1995)

[34]   Balzar, D., Voigt-function model in diffraction line-broadening analysis, in Microstructure Analysis from Diffraction, Snyder, R. L. et al. editors IUCR monograph (2001)

[35]   TOPASTM Rietveld refinement software, Bruker-AXS (2003)

[36]   Omotoso, O., Mikula, R., High surface area caused by smectitic interstratification of kaolinite and illite in Athabasca oil sands, Applied Clay Science 25 37-47 (2004)

94

[37]   Omotoso, O., Mikula, R. J., Urquhart, S., Sulimma, H., Stephens, P. W., Characterization of clays from poorly processing oil sands using synchrotron techniques, Clay Science 12 88-93 (2005)

[38]   Abend, S., Lagaly, G., Sol-gel transitions of sodium montmorillonite dispersions, Applied Clay Science 16 201-227 (2000)

[39]   Mourchid, A., Delville, A., Lambard, J., Lecolier, E., Levitz, P. Phase diagram of colloidal dispersions of anisotropic charged particles – equilibrium properties, structure, and rheology of laponite suspensions, Langmuir 11, 1942-1950, (1995).

[40]   Rasteiro, M. G., Salgueiros, I., Rheology of Particulate Suspensions in Ceramic Industry, Particulate Science and Technology, 23 145-157 (2005)

[41]   Wallace, D., Tipman, R., Komishke, B., Wallwork, V., Perkins, E., Fines/Water Interactions and Consequences of the Presence of Degraded Illite on Oil Sands Extractability, The Canadian Journal of Chemical Engineering, 82 (2004)

[42]   Brandenburg, U., Lagaly, G., Rheological properties of sodium montmorillonite dispersions, Applied Clay Science, 3 263-279 (1988)

[43]   Firth, B. A., Flow properties of coagulated colloidal suspensions: II. Experimental properties of the flow curve parameters, Journal of Colloid and Interface Science, 57, 257-265 (1976)

[44]   Chong, J. S., Christiansen, E. B., Baer, A. D., Rheology of concentrated suspensions, Journal of Applied Polymer Science 15 2007-2021 (1971)

[45]   Keattch, C. J., Dollimore, D., An Introduction to Thermogravimetry, Second Edition, Heyden and Son Ltd., (1975).

[46]   AUTOQUANTM Rietveld refinement software, GE Technologies (2005)

96

Appendix A
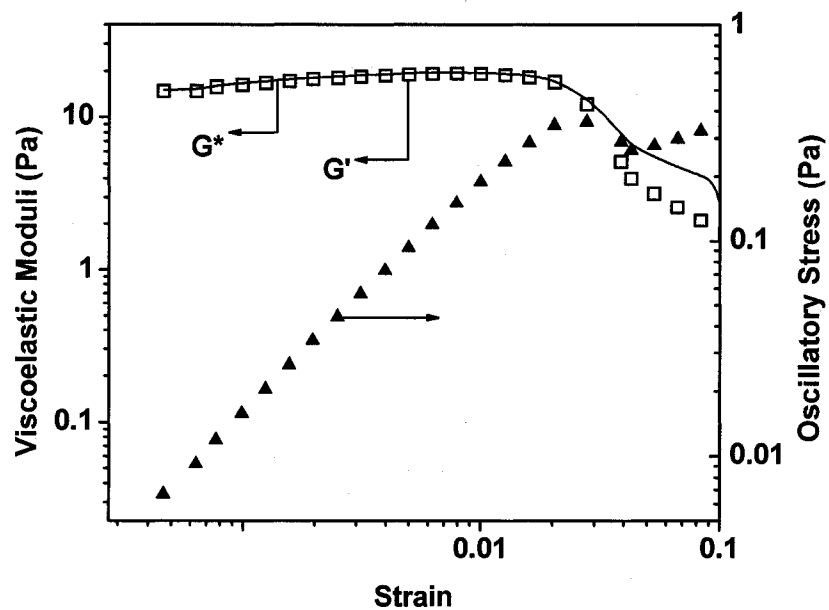
Figure A.1 – Strain sweep on a 20 wt% suspensions of fraction 1.
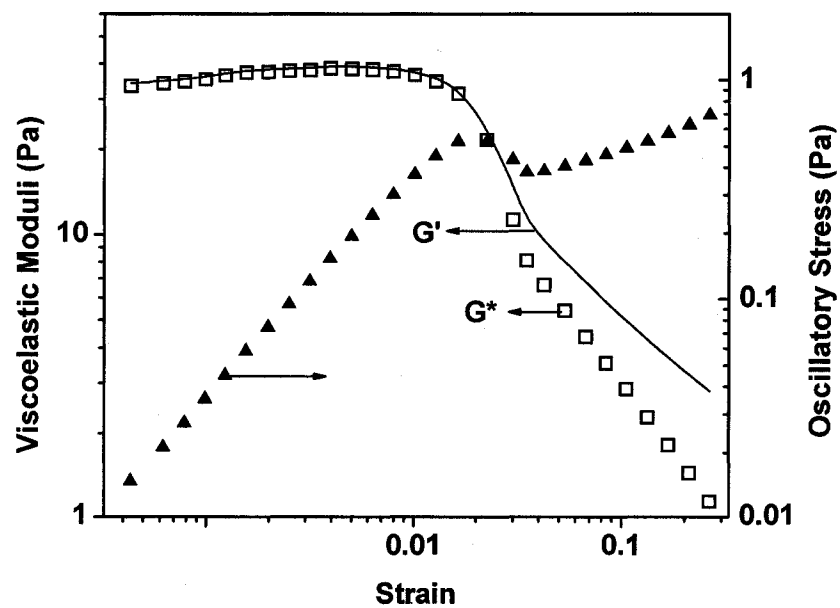
Figure A.2 – Strain sweep on a 40 wt% suspensions of fraction 1.
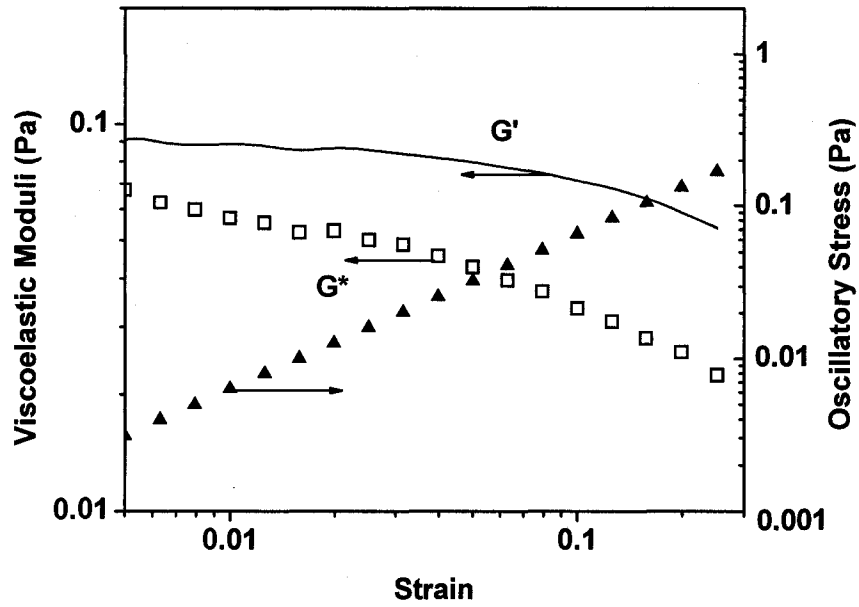
Figure A.3 – Strain sweep on a 10 wt% suspensions of fraction 2.
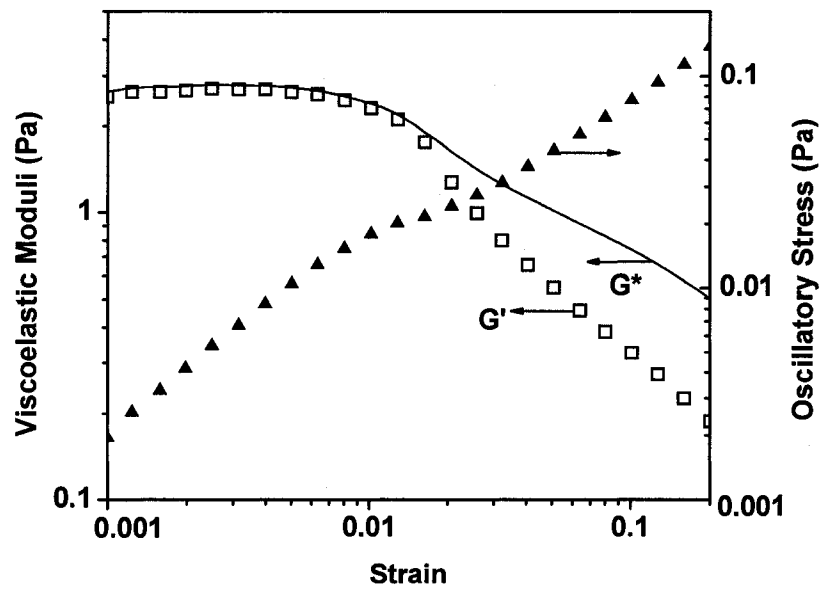
Figure A.4 – Strain sweep on a 20 wt% suspensions of fraction 2.

98
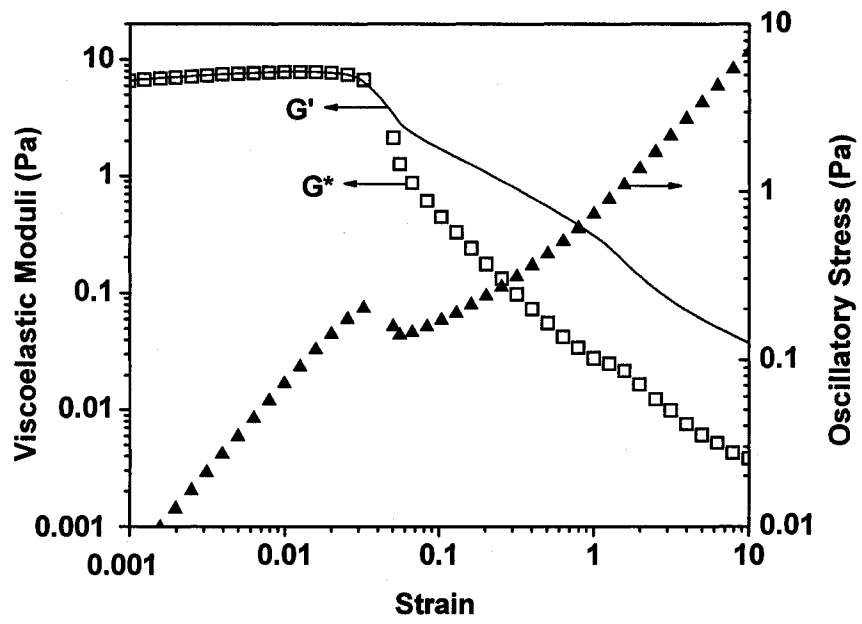
Figure A.5 – Strain sweep on a 30 wt% suspensions of fraction 2.
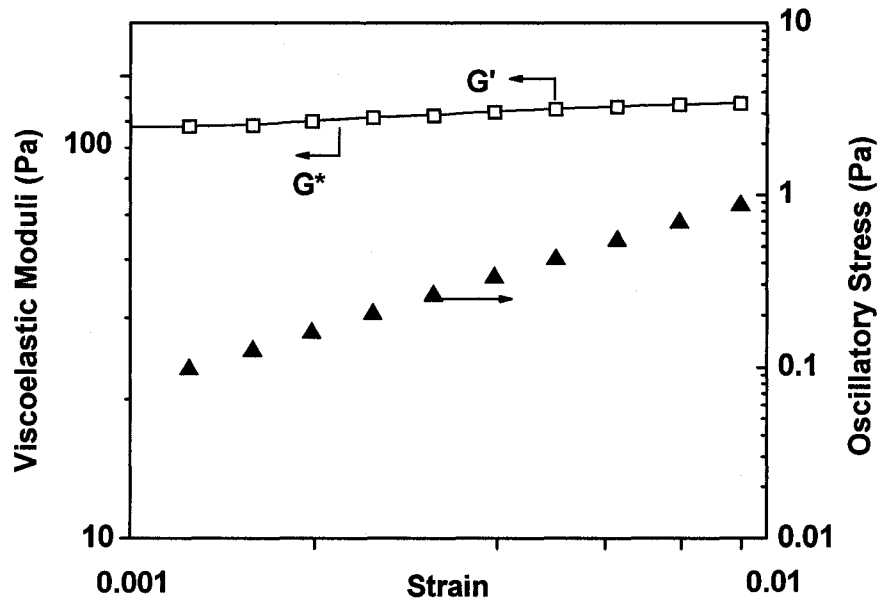
Figure A.6 – Strain sweep on a 5 wt% suspensions of fraction 3.

99
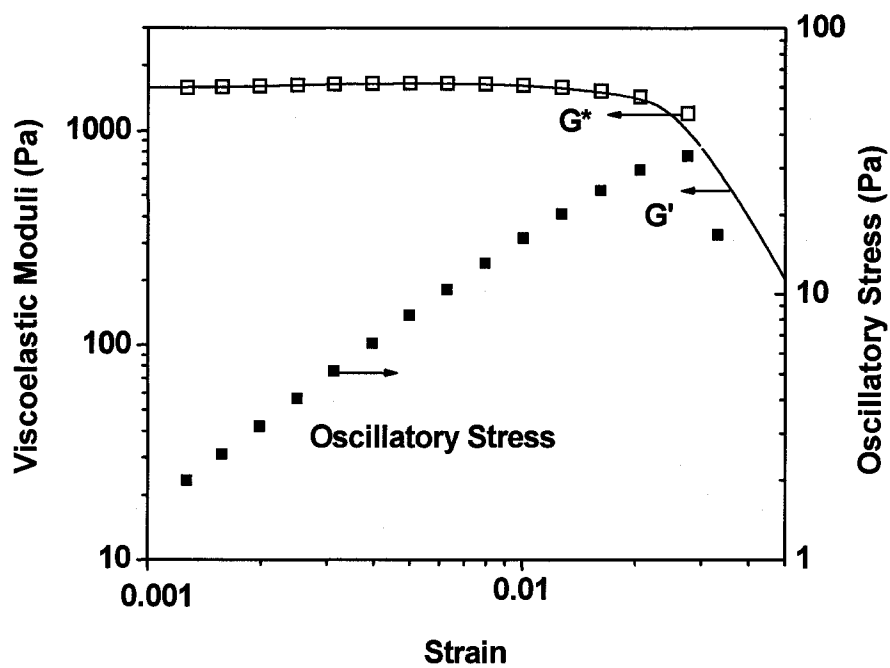
Figure A.7 – Strain sweep on a 15 wt% suspensions of fraction 3.
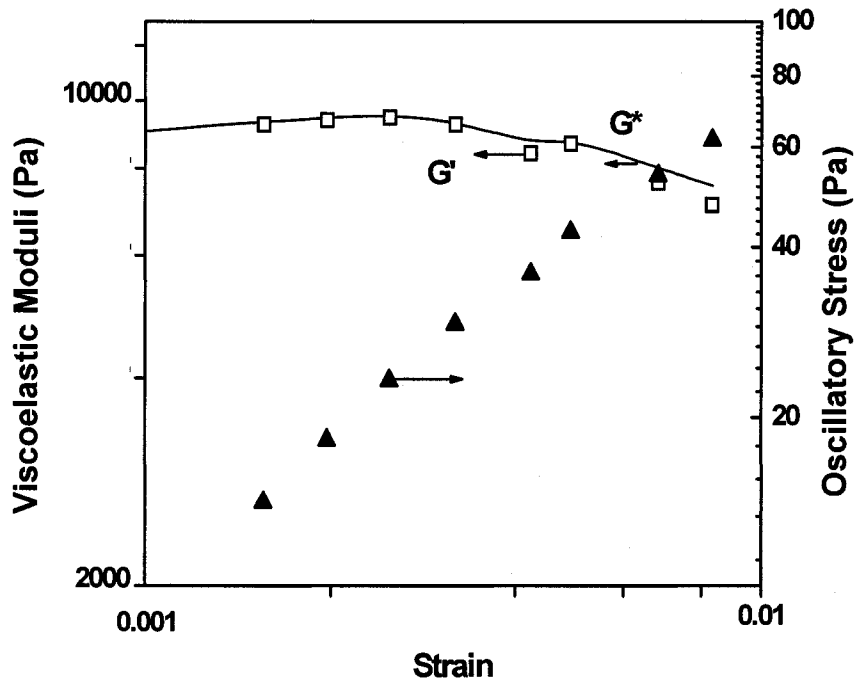
Figure A.8 – Strain sweep on a 25 wt% suspensions of fraction 3.